令和 5 年度　博士論文

Water Window X-ray Emission from Gold Foil Targets under Nd:YAG Laser Pulse Irradiation

（Nd:YAG レーザーパルスによる金箔ターゲットからの水の窓 X 線放射に関する研究）

指導教員　難波　愼一　教授

提出者　広島大学　先進理工系科学研究科

プラズマ基礎科学研究室

D213009 王　笳豪

Abstract

Water Window X-ray Emission from Gold Foil Targets under Nd:YAG Laser Pulse Irradiation

プラズマ基礎科学研究室
D213009　王笳豪

Soft x-ray sources developed by laser produced plasma (LPP) hold great promise for applications in diagnostic and manufacturing nano-devices. Particularly, soft x-rays in the water-window (WW) region (2.3-4.4 nm) offer significant advantages for biological diagnostics. The K-absorption edges for C (4.4 nm), N (3 nm) and O (2.3 nm) fall within this wavelength range, providing high transmission contrasts in living biological cells rich in these elements. Consequently, it is employed in soft x-ray microscopy (SXM) for biological diagnostic in various scenarios. This not only allows imaging of relatively thick living organ samples without sample pretreatments (such as dehydration and sectioning), but also enables the observation of organelles in the cytoplasm with high contrast.

The imaging resolution and quality for SXM are significantly limited by the photon fluence reaching the sample surface. Currently, only large facilities using synchrotron radiation sources can achieve a brightness exceeding 10^{14} photons/ (sr · s · μm^2 · 0.1% bandwidth) for high-quality imaging. However, the brightness of LPP hinders the widespread deployment of SXM, not to mention the associated costs and availability of the required devices. Hence, it is crucial to enhance the photon fluence produced by tabletop devices.

One of the methods is to use laser-produced Au plasma. Due to the n=4-4 and 4-5 transitions in the highly ionized Au ions, x-ray emissions emitted from countless energy levels forms unresolved transition arrays (UTA) with a peak wavelength within the WW region. On the other hand, WW x-ray emission enhances when generating laser-produced Au ions in a low pressure N_2 gas, benefiting from the KLL-Auger electrons emitted from the N atom interact with the highly charged Au ions. These make Au a suitable material for LPP scheme to develop a WW x-ray source.

The contact type SXM is favorable for the laser-produced Au plasma scheme. The generated x-rays with short pulse duration effectively reduce blur, while the focused laser spot can confine the emission in a small region with high brightness. However, a high-repetition tape target system is needed to develop a practical contact SXM. An optimal target thickness not only reduces the target cost drastically but also decreases plasma debris, extending the durability of the optical components.

In this work, a comprehensive measurement on the optimal Au target thickness for WW emission was conducted. Foil targets and thermal deposition Au targets ranging from 300μm to 0.1 μm were manufactured and tested. A subsequent optimization of the laser focus condition at a fixed laser energy was also applied to find the most effective condition for WW radiations. The experimental results were compared with the numerical simulations using the Flexible Atomic Code and the Star-2D code. Thermodynamics of the particles in the plasma were studied, providing a comprehensive explanation for the emission behavior observed by the emission spectroscopy.

Outline

1. INTRODUCTION

A wide range of applications using different kinds of light have been brought into our daily lives, such as the lighting, optical imaging, and laser technology. The variety of the light properties, whether it is treated as wave or particles in the quantum physics, gives much versatile on their behaviors. In particular, lights with different wavelengths can be divided into different ranges as shown in Fig. 1.

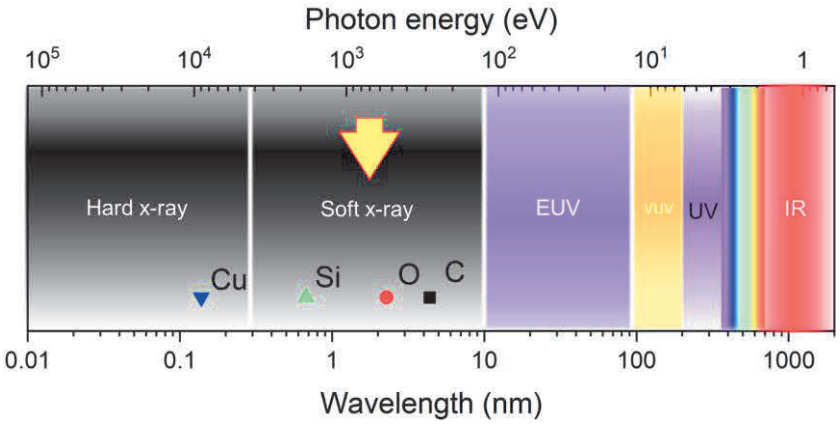

Fig. 1: Spectral ranging from infrared (IR) to hard x-ray. The 4 points indicated are the K-edges of the labeled elements. The photon energy is shown in the top-axis. Visible light is shown in rainbow band.

In this work, a special wavelength band known as the “water window” (WW) within the soft x-ray region was investigated to explore the potential development of a short-wavelength light source for scientific research. This chapter provides a comprehensive introduction to WW x-ray, organized in the sequence of source, application, and ultimately our research motivation.

1.1 Water window x-ray

Soft X-rays in the so-called water-window (WW) region are important for biological research, as this wavelength range lies between the K absorption edges for carbon (4.4 nm) and oxygen (2.3 nm), exhibiting a high transmission contrast between atomic carbon and oxygen (water), which are the two main constituents of living organisms (see Fig. 2).

The K-edge refers to the photon energy level just beyond the binding energy of the K-shell electrons in an atom, where the absorption coefficient increases drastically then decrease gradually as the energy becomes higher. After the absorption, the electron is ionized due the photoelectric effect, leaving a vacancy in the inner shell. This vacancy can be filled by an outer-shell electron, resulting in the emission of an Auger electron or characteristic x-ray, which depends on the atomic number. Same behavior also occurs for L-shell, known as the L-edge.

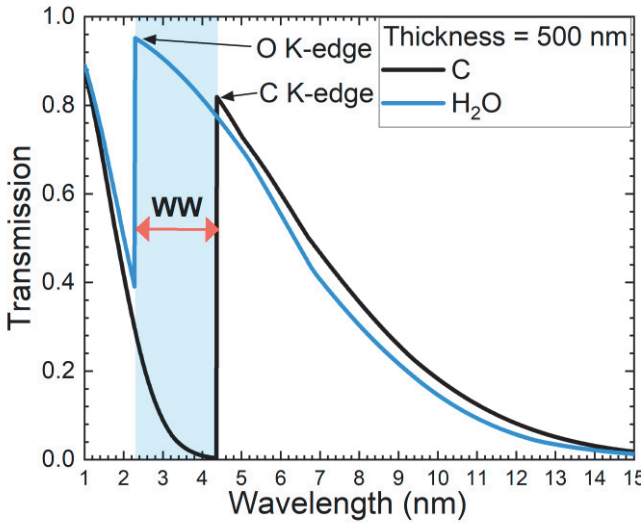

Fig. 2: Transmittance for carbon and water around the WW region (2.3-4.4 nm). The K-edges for both elements are marked. The thicknesses for both substances are set the same as 500 nm.

One of the most important applications for WW x-ray is used as the light source for x-ray microscopy. Because the resolution of the optical microscopy using visible light source is limited by the wavelength of light according to the Rayleigh criterion as,

$$\theta = \frac{1.22\lambda}{NA} \tag{1-1}$$

where *NA* is the numerical aperture for the system, and θ is the angular resolution, λ is the wavelength of light. The equation describes two images which are just resolvable when the center of the diffraction pattern of one coincides with the first minimum (dark fringe) of the other. Resolution for optical microscopy is consequently limited to several hundred nanometers. On the contrary, WW x-rays have a short wavelength with characteristic transmission bands, making them favorable for being used as imaging light source.

Since water and carbon-based organelles are the main substances in the biological cells, WW x-rays offer remarkable properties in terms of contrast and penetrating power. A comparison of the attenuation length for water and protein is shown in Fig. 3 [1].

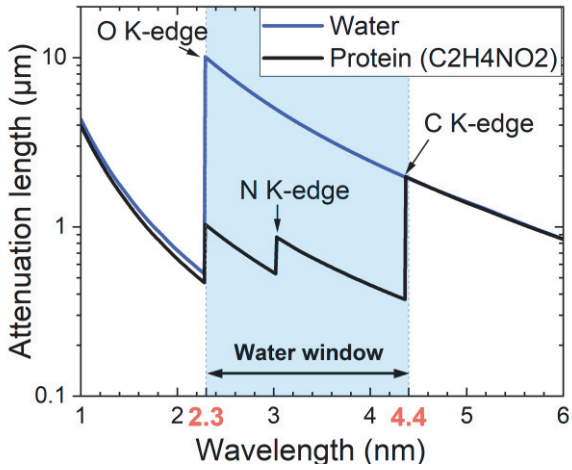

Fig. 3: The depth into the material measured along the surface normal where the intensity of x-rays falls to 1/e of its value at the surface [1].

1.2 Soft x-ray microscopy (SXM)

1.2.1 Characteristics

Short wavelength was not the sole factor that rendered SXM irreplaceable. Biologists have employed various microscopy tools, such as optical and confocal microscopy, electron microscopy, and atomic force microscopy. However, none of them could fulfill an alternative role.

The optical microscopy has limited resolution as explained above. This resolution was then improved by the confocal microscopy, which utilized the focused laser and pinholes to obtained optical sectioning of the object. An example is shown in Fig. 4 [2], the out-of-focus light was eliminated by the aperture before the detector, which increased the resolution of the system. Resolution for this technology could reach several hundred nanometers [3]. However, the high phototoxicity from the laser irradiation could not be ignored when compared to the other microscopies.

The electron microscopy (EM), including transmission type and scanning type, can produce almost unlimited resolution for imaging cellular structures. Because the size of the electron is negligible compared to the object. But the sample needs to be placed in the vacuum as shown in Fig. 5 to receive the electron interaction, which brings damage at the same time. Also, the penetration depth for the electron beam is typically below 1 μm [4]. These limitations make sample for EM need to be section and dehydration, which is not suitable for observing living cells.

Atomic force microscopy is utilized as a surface evaluation technology, where the atomic force between the cantilever and the sample atoms is detected and converted into a signal. This method can be applied in both air and liquid environments, making it versatile for numerous applications. However, it is important to note that the inner structure of the sample is not accessible through this method [5].

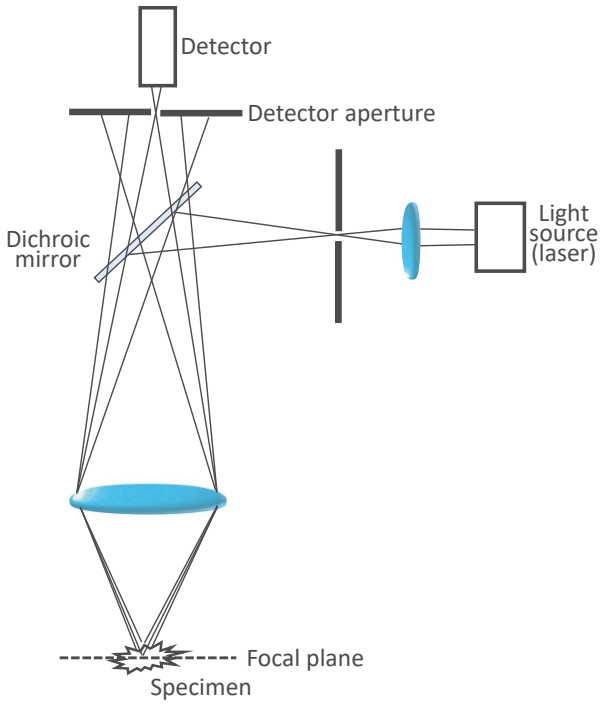

Fig. 4: Schematic of a confocal microscopy [2].

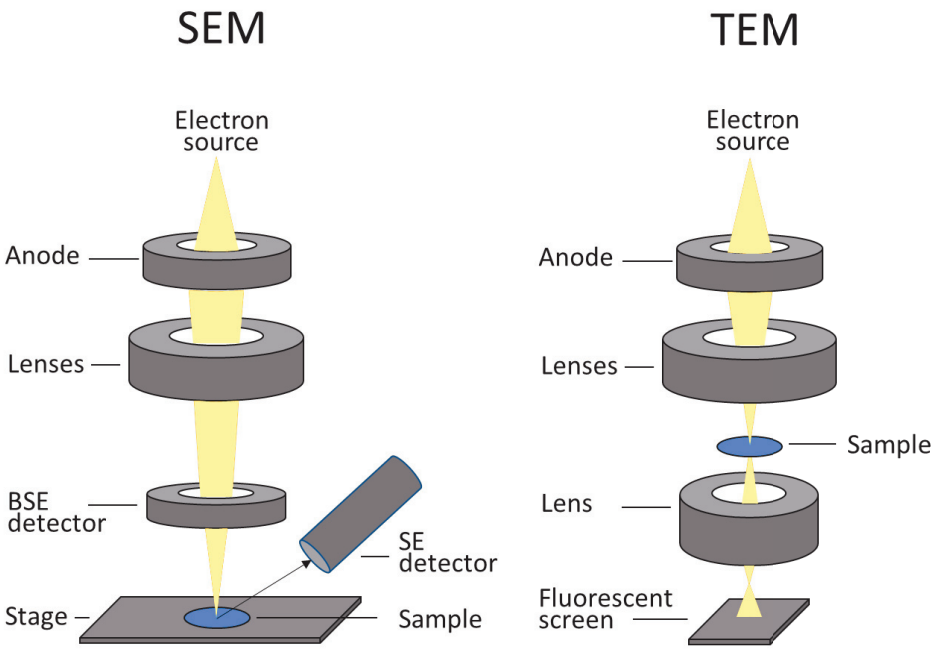

Fig. 5: Schematic of the typical scanning electron microscopy (SEM) and transmission electron microscopy (TEM).

Compared to the aforementioned techniques, SXM utilizing WW x-rays boasts unique contrast with excellent penetration power, thereby enhancing the signal-to-noise ratio. In SXM, the scattering process is negligible in comparison to absorption, with the photoelectric effect dominating in this photon energy range (as depicted in Fig. 6) [6]. This aspect is crucial for maintaining image quality, as the scattering process can introduce blur to the image. Additionally, the depth of field for SXM has been improved to a relatively large range [7,8], enabling the possibility of 3D imaging.

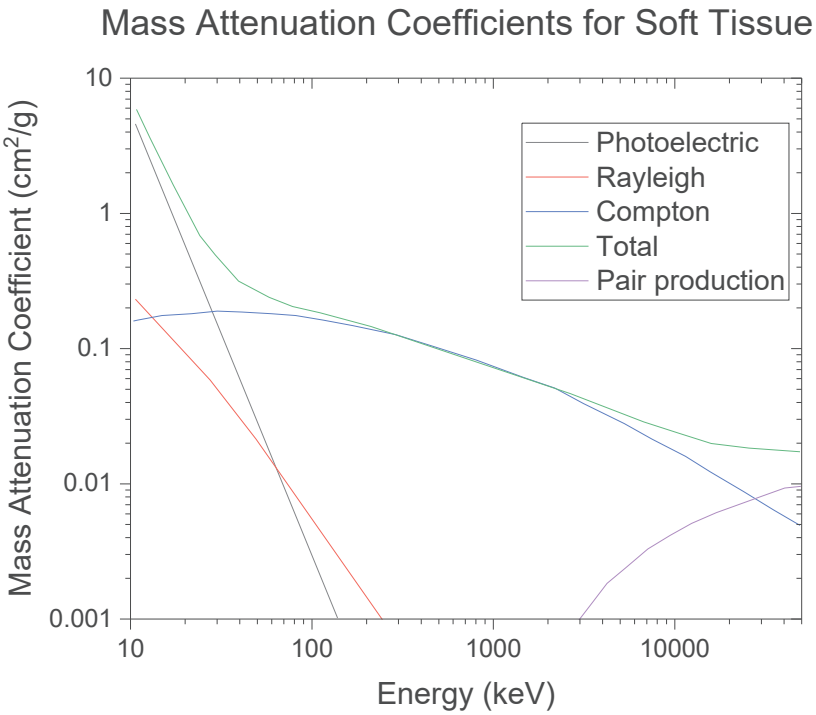

Fig. 6: Graph of the Rayleigh, photoelectric, Compton, pair production, and total mass attenuation coefficient for tissues (Z=7) as a function of photon energy. [6]

1.2.2 Different types of the SXM

The structure of SXM undergoes significant changes over time. Since x-rays were first discovered by Röntgen [9], it was soon applied to a point-projection microscopy by Malsch [10] as shown in Fig. 7. The electrons were emitted from the filament cathode to the aperture. A collection coil was applied to the tube, focusing the electrons onto a metal foil with a spot diameter of 0.1 mm. The interaction between the electrons and the metal foil radiates x-rays from the foil surface due to the bremsstrahlung (braking radiation). Finally, the object placed near the radiation point could be imaged onto a luminous screen as a magnified shadow. The image was obtained with a resolution of a few microns, indicating a high potential for developing high-resolution microscopy.

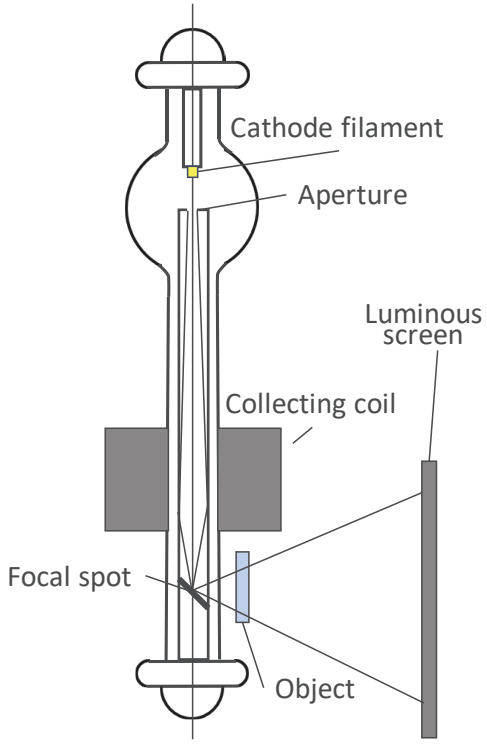

Fig. 7: Schematic of a point-projection microscope [10].

After decades of the development, three types of SXM have come into view.

- **Contact x-ray microscopy**

The contact SXR utilizes x-ray sensitive resist underneath the sample to convert x-ray images into the detectable form (e.g., AFM or visible light). The technique was developed by Spiller, E., *et al*. [11], who used carbon Kα line (4.48 nm) and synchrotron radiation source to obtain SXM images with a resolution of near 10 nm. A laboratory contact x-ray microscopy, which used picosecond single pulse soft x-ray from the laser-produced plasma, observed nanometer-scale inner structure of the living biological specimen in a hydrated condition [12].

An example structure of the contact SXM is shown in Fig. 8. Soft x-rays were emitted from the laser produced plasma and collected by using the grazing-incidence toroidal mirror.

The focused soft x-ray spot penetrated through the sample and absorbed by the scintillator. Since the transmission rate for the sample's inner structures were different, the image was then converted to the visible light and finally detected by the camera. Since the soft x-rays were generated for the single pulse shot, the short exposure time could avoid the radiation damage of the sample. Moreover, the brown motion of the cells and diffusion of proteins were found to be at a microsecond or sub-microsecond time scale, while the duration of the X-ray pulse is almost consistent with the pumping nanosecond/picosecond laser pulse [13]. A 3D imaging was even possible by using stereo-pairs with different observing angle. However, it is obvious that many aspects may affect the final image quality, such as the diffraction, the penumbral blur due to the sample thickness, and nonlinear effects in the resist development [14,15].

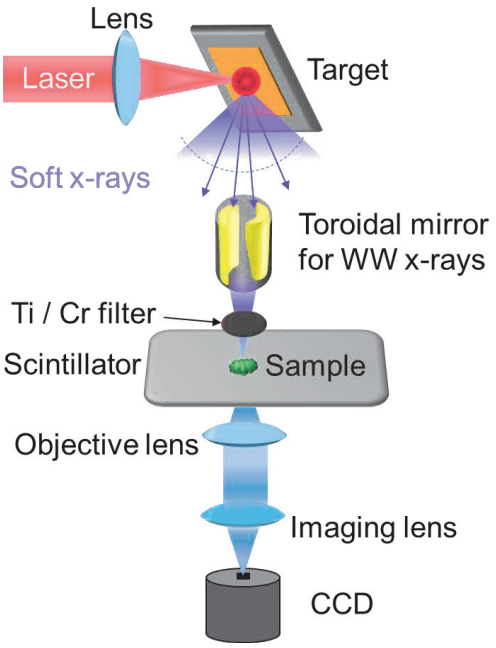

Fig. 8: Schematic of a typical contact SXM.

- **Scanning transmission SXM**

The scanning transmission SXM was first demonstrated by [16] as illustrated in Fig. 9. A zone plate served as a condenser to focus the x-rays from the synchrotron source into a point on the sample. To obtain the image, the x-ray energy was held constant, and the sample was raster-scanned in the focus of the x-ray microprobe forming a 2D map of the x-ray absorbance. The scanning transmission SXM benefits from the high brightness and consistent output of the synchrotron source, a characteristic that is challenging to replicate on a laboratory scale where limited brightness of x-ray sources is common.

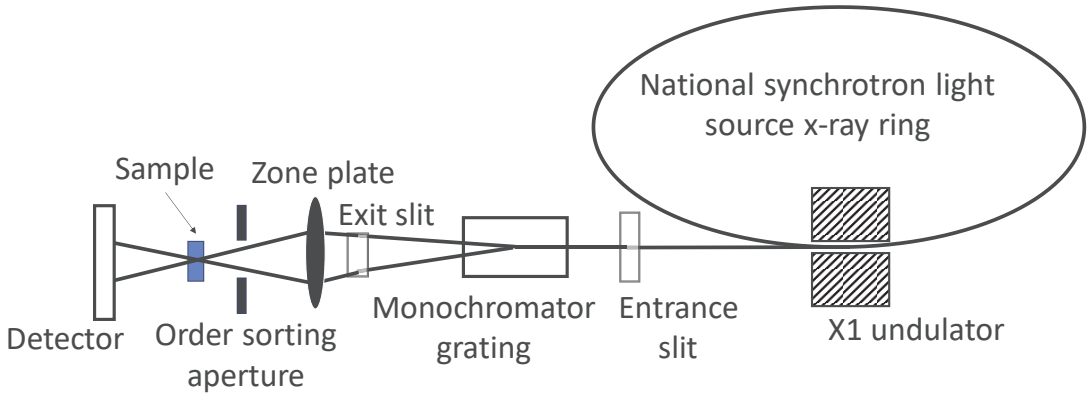

Fig. 9: Schematic of the Stony Brook scanning transmission SXM [16].

- **Full-field transmission SXM**

The primary difference between the full-field transmission SXM and the scanning transmission SXM is that the x-ray is focused onto the full-field of the sample, without a requirement of moving the sample stage for scanning. The first development was achieved by [17] (Fig. 10). In this setup, a polychromatic radiation source was dispersed by a holographic laminar grating through a holographically zone plate, generated a reduced monochromatic image of the synchrotron source in the object plane. The image optics was a micro zone plate which generated the magnified image on the image plane. This full-field imaging scheme was suitable for a tomographic 3D imaging due to the relatively short exposure time. Similar as the stereo-pairs described in the contact SXM, imaging from several angular projections was possible when used a rotation sample stage [18].

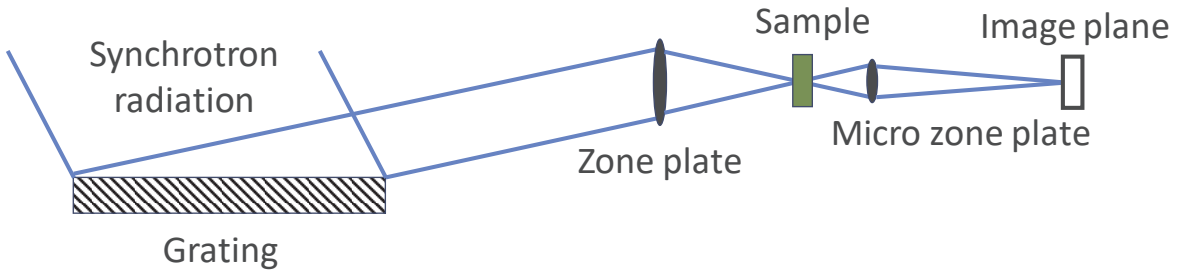

Fig. 10: Schematic of the first full-field transmission SXM [17].

- **Laboratory scale SXM**

A wide deployment for the SXM is undoubtedly craved as the excellent imaging quality obtained using synchrotron x-ray sources. However, achieving the same order of brightness as a synchrotron source for x-rays is currently impossible on a laboratory scale. Lots of attempts have been made to develop a compact SXM so far.

In [19], a compact cryogenic soft x-ray computed tomography was developed using a z-pinch plasma as the x-ray source. Resolution better than 50 nm was achieved. While in [20], a full-field transmission SXM was developed using the laser-produced plasma as the pumping scheme to generate WW x-rays (Fig. 11). The resolution of this setup reached 40 nm when irradiating the nitrogen gas target with a laser power of 60 W.

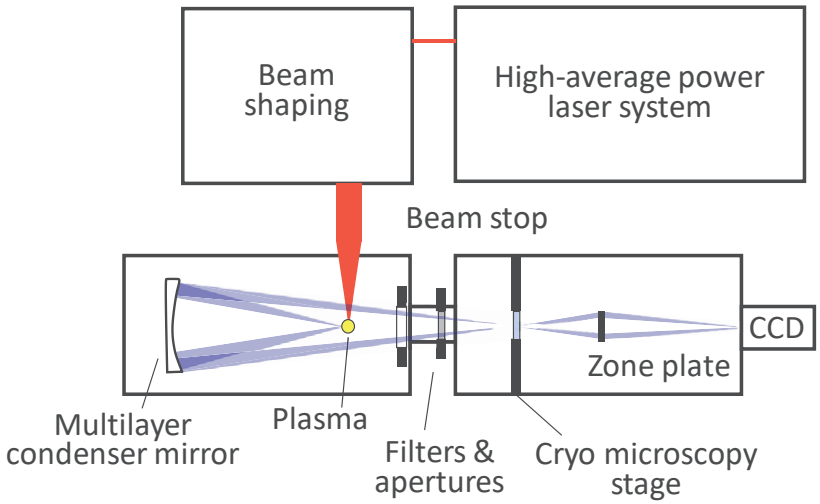

Fig. 11: Schematic of the compact full-field SXM using laser-produced plasma [20].

Although good imaging quality was achieved in these works, the huge gap in the brightness between synchrotron x-ray source and other schemes made the resolution of the biological images incomparable.

1.2.3 Optics

Most focusing optics used in the wavelength range of visible light are not available for x-rays, due to the complex refraction index is almost 1 and the absorption of the medium is high. The complex refraction index n^* is given by,

$$n^* = 1 - \delta - i\beta \tag{1-2}$$

where $(1-\delta)$ describes the ratio of the free-space speed of the light to the speed in the medium, β describes the absorption aspect of the electromagnetic wave [21]. For the common optics made by SiO_2, the factors of refraction index are shown in Fig. 12. While the absorption coefficient α of the material can be calculated by,

$$\alpha = \frac{4\pi\beta}{\lambda} \ (cm^{-1}) \tag{1-3}$$

It is evident that alternative methods are necessary to efficiently focus WW x-rays from the source onto the sample. Below, the most common optics for collecting x-rays are discussed.

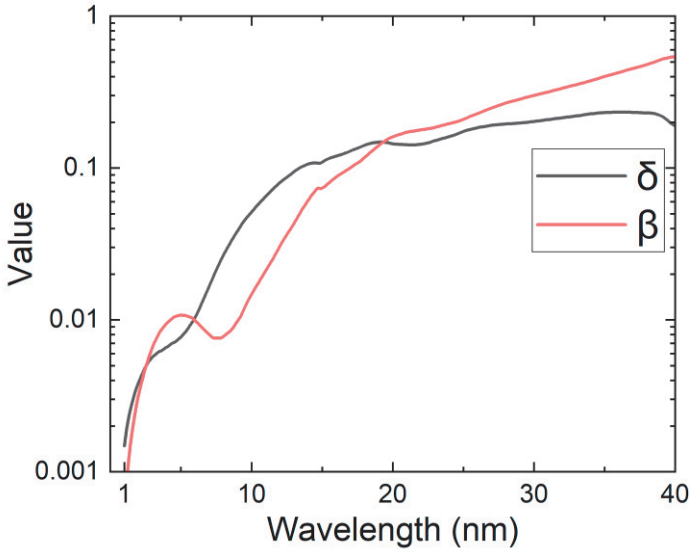

Fig. 12: The factors of the complex refraction index for SiO_2, δ and β, as a function of wavelength [1].

- **Zone plate**

The zone plate is a kind of optics using diffraction and phase shifting for the passing light wave to generate a focus point. was first developed by Baez, A. [22]. For a classical type, it consisted of a series of transparent and opaque concentric rings or zones, with a designed

width so that monochromatic x-rays was focused onto one point by the diffraction. The principle is illustrated in Fig. 13, as the rings of the zone plates follow:

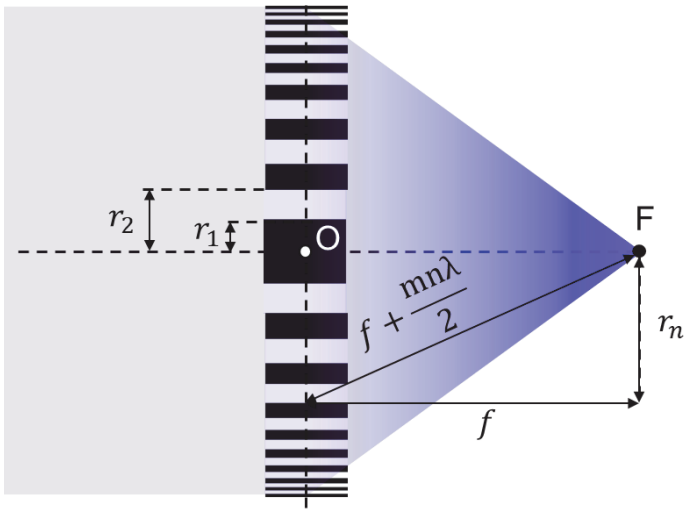

Fig. 13: Schematic of the Fresnel zone plate. F is the first order of the zone plate focal point. r_n refers to the n-th zone, m refers to the order of the diffraction wavelength.

$$f^2 + {r_n}^2 = (f + \frac{nm\lambda}{2})^2 \tag{1-4}$$

where r_n refers to the n-th zone, m refers to the order of the diffraction wavelength. The value m is due to the several orders generated from the diffraction, which can affect the efficiency η_m of the zone plate by,

$$\eta_m = \frac{1}{(\pi m)^2} \tag{1-5}$$

When a higher order of the focus is used, the efficiency reduces correspondingly. The equation (1-4) illustrates when the path between two x-rays emerging from two neighboring zones is $n\lambda/2$, interference can be generated at the focus point F. In this way, constructive and destructive interferences are combined at F. By blocking the destructive interferences (n = 1, 3, 5, …), a constructive focal point can be generated. However, since r_n is a function of λ, chromatic aberration can reduce the focusing efficiency.

Errors during the manufacturing of the zone plates can also cause aberrations, since zone plates generally consist of several tens of thousands of rings with a size in nanometer scale [23].

- **Grazing incidence mirror**

The grazing incidence mirror refers to the optics that used in a small incident angle (nearly 90 degrees) for x-ray reflection. It can also be used for Schwarzschild focusing mirror,

multilayer mirror, and so on. Principle of the grazing incidence mirror can be obtained from the diffraction formula as,

$$\frac{sin\,\theta}{sin\,\gamma} = \frac{n_2}{n_1} \tag{1-6}$$

where θ and γ are the incident angle and diffraction angle, respectively. n_1 and n_2 are the refraction indexes of the incidence medium and diffraction medium, respectively. Noting the refraction index is connected the former equation (1-2) as,

$$n = 1 - \delta \tag{1-7}$$

When the diffraction angel γ becomes 90 degrees, θ reaches the critical angle, where any θ larger than the critical angle can generate a total reflection. For x-ray coming from the vacuum, $n_1 = 1$, while the refraction medium (e.g. Au coating for 2.55 nm WW x-ray) has a $n_2 = 0.995$. Consequently, the critical angle is 84 degrees which is a grazing incidence condition.

- **Multilayer mirror**

The multilayer mirror consists of many reflection layers, each layer reflects part of the x-ray, and the rest is reflected by the underneath layer. The primary principle is given by the Bragg's law as,

$$2D\,sin\,\theta = n\lambda \tag{1-8}$$

where θ is the incidence angle, d is the spacing between each layer, n is the integer. This schematic is also illustrated in Fig. 14. As the reflected waves have a constructive interference similar to the principle described in the zone plate section, the reflection can be enhanced. In the practical case, the spacing d continuously changed, governing the direction of the reflection light into the desire shape [24]. The layers usually consist of two kinds of materials to create an index contrast. The multilayer mirror can be manufactured into a spherical shape, which owns a wide incident angle for x-ray focusing when compared with Fresnel zone plate.

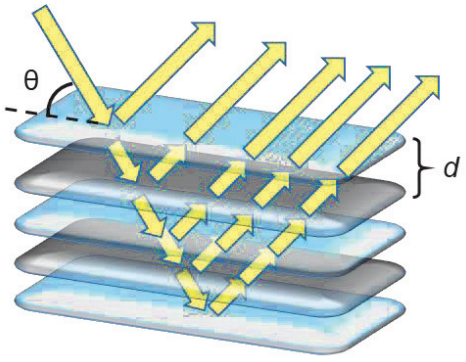

Fig. 14: Schematic of the Bragg's law.

The materials which have absorption edges in the WW x-ray region are usually used to manufacture the multilayer mirror due to the high diffraction index (as shown in Fig. 15). For examples: In [25], W/B_4C and Co/C were developed for multilayer mirrors with reflectivity of >40% and >10% at 2.48 nm and 4.47 nm, respectively. In [26], V/Sc mirror was used to produce a reflectivity of 18.4% at 3.129 nm and 5.2% at 2.425 nm. A list of refraction index of the complex oxide was given by [27], emphasized the importance of complex oxide for high reflectivity multilayer mirror. Besides, large grazing incidence angle and normal incidence mirror were also developed as described in [28–31].

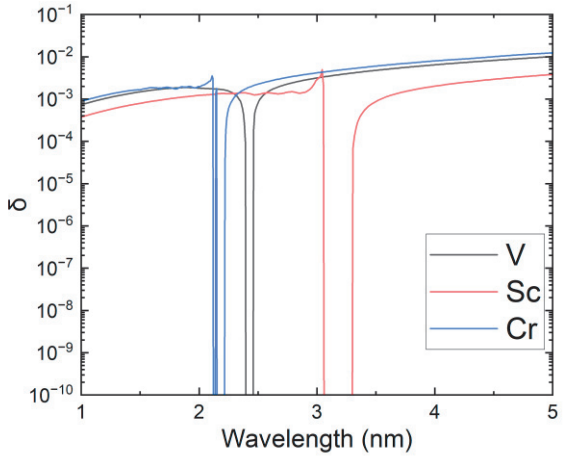

Fig. 15: Delta value for the common elements used for x-ray multilayer mirror at the WW region [1].

1.2.4 WW x-ray source

The WW x-ray source is one of the most important parts in the SXM. While the practical use of the SXM is highly dependent on the brightness of the light source, the size of the device can also impose limitations on widespread deployment. Several main schemes have been developed for producing WW x rays.

- **Synchrotron radiation**

The synchrotron radiations use strong magnetic field to bend high-speed electron, emitting strong x-rays due to the bremsstrahlung process. The speed of electron is near to the speed of light, giving an ultra-relativistic condition where the total energy E of the electron is almost completely equal to its kinetic energy. As giving by

$$E = \frac{mc^2}{\sqrt{1 - \frac{v^2}{c^2}}} = \gamma mc^2 \tag{1-9}$$

where c is the speed of light, γ is the Einstein relativistic factor. v is the particle velocity and m is the particle mass [32]. For the particles that $v \to c$, the emitted photons from the electron have a highly forward direction, which is crucial to predict the final spectra and spatial radiation distribution for the source. Since in this case,

$$E = \gamma mc^2 \approx pc \tag{1-10}$$

where p is the Lorentz invariant momentum. Both electrons and emitted photons are moving along p, because most of the electron momentum is associated with the forward motion [33].

Different from the bonded electrons in the atoms, the accelerated electrons do not have energy levels so that selected continuum spectra band can be emitted, providing high brightness for a wide range of applications from hard x-ray to infrared. Depending on their principles, synchrotron sources can be divided into four types: bending magnet, wiggler, undulator, and free electron laser. Each one has different radiation characteristics as illustrated in Fig. 16. The bending magnet employs a magnetic field perpendicular to the direction of electron motion, generating Lorentz force to bend the electrons. Since the bending is a gradual process, continuum spectra are generated in this case, which also have a relatively large radiation diversity. Wiggler and undulator, on the other hand, use alternating electromagnetic field to continuously bend electrons, emitting radiations along the forward direction. The undulator utilizes a periodic magnetic field to ensure emissions from the same electron exhibit good coherence, while there is no coherence among different electrons. Harmonic radiation can also be generated as shown in the third line in Fig. 16. Coherent radiation can be achieved by the free electron laser, as the radiations are controlled to be in the same phase. Consequently, strong radiation with sharp spectral peak is obtained [34,35].

Synchrotron radiation sources have been applied to SXMs in many works. In [36], the x-ray photon energy of 516 eV was used to observe freshwater organism with a resolution less than 100 nm for structure in hydrated condition. In [37], free electron laser operating at a

wavelength of 13.7 nm obtained an output at 2.75 nm as the 5-th order harmonic. A summary of the brightness of WW x-ray source utilizing state-of-the-art synchrotron sources is provided in reference [38].

Synchrotron radiations can produce intense WW x-rays, suitable for achieving resolutions in the range of a few tens of nanometers [39]. However, these facilities require significant space and incur high operating costs, rendering them impractical for widespread deployment.

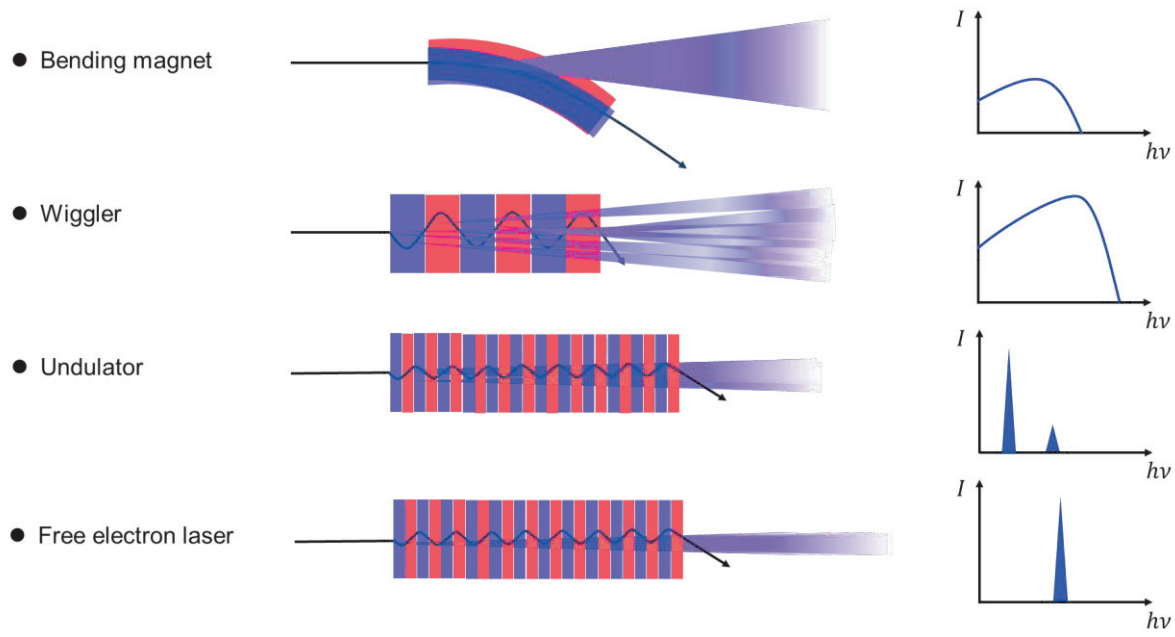

Fig. 16: Schematic of the different types of synchrotron radiation source. The middle row shows radiation part for each type. The row on the right side shows the output characteristics for each type.

- **Discharge pinch plasma**

Generally, discharge produced plasma (DPP) is generated by applying high voltage to a gas, liquid and solid. When the material is initially ionized by the electric field, electrons are generated and collide with the remaining particles, leading to the formation of a nearly fully ionized plasma. Subsequently, a self-focusing of the plasma occurs due to the strong magnetic field induced by the abundant electric charges [40], pulling the plasma through the central axis [41]. The compressing causes an increase in the temperature and density, and the emission gets stronger. The compressed plasma is known as the z-pinch plasma. The letter "z" is used to denote that the electric current direction is longitudinal. The schematic is shown in Fig. 17.

The discharge plasma can produce stable, sustainable WW x-rays as illustrated in [42], where a strong line spectrum at 2.88 nm was generated from the He-like nitrogen ions in a pinch plasma. SXM using a z-pinch capillary discharge plasma source illustrated in [43] achieved a resolution of 75 nm using the same gas. Since the plasma source is relatively large when compared with other schemes, the broad emission area may not be efficiently used and

result in a low brightness.

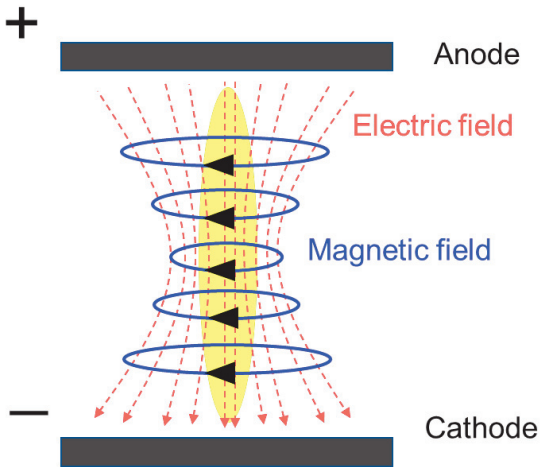

Fig. 17: Schematic of the z pinch plasma. The electric field is pulled by the magnetic field, compressing the plasma to high temperature and density.

- **Laser-produced plasma**

Laser produced plasma (LPP) has also been considered suitable for WW x-ray sources. Generally, a high-energy laser pulse, either single or multiple, is focused onto a target, ablating the target into vapor. As the temperature continues to rise, hot dense plasma is generated. The electron density of the plasma increases during the heating process, reaching the critical density where the laser can no longer penetrate further. Consequently, the laser energy is effectively absorbed in this region, while the remaining energy is reflected to some extent. The concentrated high-energy laser pulses enable intense x-ray emission to be confined to a small area within the plasma, resulting in high brightness. The detailed principles of the laser-produced plasma are discussed in the next section.

Various parameters in this process can be manipulated to select the desired emission wavelength. For example, targets in different types have been used for WW generation: In [44], Argon-Helium gas target was used for LPP, giving a photon fluence of 10^3 photons/ (μm^2 × pulse) in the WW region. A resolution of 80 nm was achieved when observed biological specimen in a helium atmosphere. The x-ray laser scheme, utilizing the three-body recombination process in the He-like carbon plasma, was also employed to produce lasing emission at 4.03 nm [45]. It is clear that the brightness of LPP source is several orders of magnitude smaller than the synchrotron radiation sources. However, the LPP scheme is favorable for developing a compact, low cost SXM, which is essential for this application.

- **Brightness**

Brilliance (brightness), which is defined as photons/ (s × sr × μm^2 × 0.1% Band width (BW)), is often used to evaluate a WW x-ray source [38]. It describes the number of photons emitted per second, per unit solid angle, per area, with a specific wavelength in a narrow band.

The brightness is useful as the effective WW intensity applied on the sample is limited, and the spatial and angular flux can be calculated by integrating over the solid angle and the area, respectively [19].

A convenient method to calculate the minimum photon fluence is given by D. Sayre [46] by calculating the transmitted photons behind the protein sample for an image signal-to-noise ratio over 5 (schematic shown in Fig. 18).

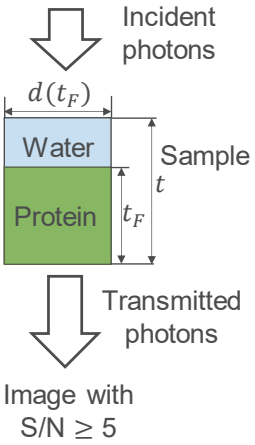

Fig. 18: Schematic of the calculation described by D. Sayre in [46]. The incident photons pass through the sample, which consists of water and protein (feature region) (thickness t_F). The imaging object is an idea cube in the size of d (length) $\times$ d (width) $\times$ t (thickness). Only absorption and transmission are considered in this case. An detector is placed below the sample, imaging the area with no photon loss.

The result is shown in Fig. 19. Four areas are shown with different characteristics, green: the electron microscopy performance better than the x-ray microscopy in this region due to less required radiation dose. Gray: the radiation dose above 10^9 Rads is no longer capable for the structure survival of organic molecules. Light blue: optical microscopy is possible to reach the resolutions in this region, where no need to use the x-ray microscopy. Red: WW SXM takes advantages where the sample structure can survive after the radiation, and the resolution is beyond the optical microscopy.

It has been calculated that a photon fluence of ~10^6 photons/μm^2 is required to obtain an x-ray microscopy image of protein with a spatial resolution under 100 nm with a sample thickness below 10 μm. The value of the signal-to-noise ratio is known as the Rose criterion, which illustrated a signal-to-noise ratio of at least 5 is required to be able to distinguish image features with certainty [47].

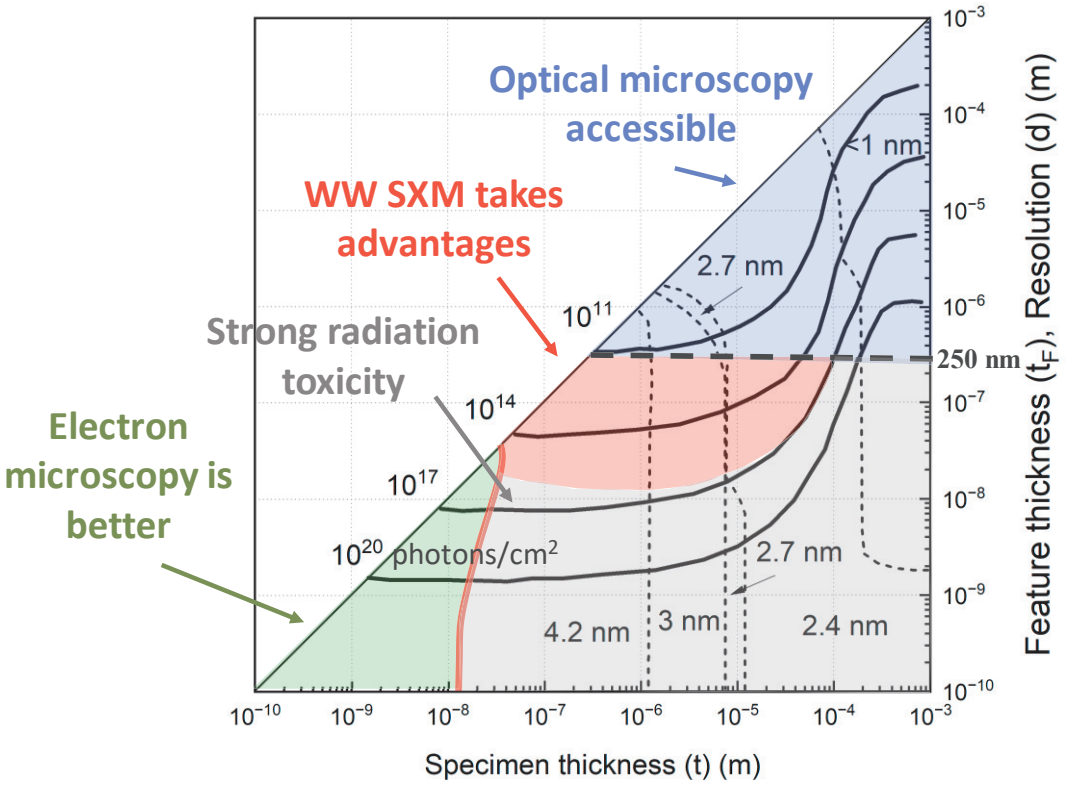

Fig. 19: Minimum photon fluence for a bright-field mode x-ray microscopy as a function of specimen thickness t, and feature thickness t_F. The unit size of the specimen $d \times d$ was set as $d = t_F$ for the convenience of calculation. Only 4 lines are shown the plot. The read line shows the edge where electron microscopy and x-ray microscopy perform the same with the same radiation dose. The thick dash line shows the limit resolution for the optical microscopy. The short dash lines which separate the area show the optimal wavelength for the minimum photon fluence in that region. Four color regions show different characteristics.

However, the exposure time for a sample is also limited when considering practicability and the image blur caused by the Brownian motion of the particles [47]. An x-ray microscope using synchrotron radiation sources can achieve a brilliance of over 10^{18} photons/(s × mrad^2 × mm^2 × 0.1%BW) [48]. In contrast, a permanent laser-plasma setup can only reach a brilliance of 10^{12} photons/(s × sr × μm^2 × 0.1%BW) [49].

Indeed, it is crucial to highlight that the practical resolution of a SXM is influenced by all components, ranging from the light source to the imaging detector. Furthermore, the contrast of the image can vary based on the ratio of wavelengths in the spectra. Improving the conversion efficiency (CE) remains one of the primary points for LPP in the development of a compact WW x-ray source.

1.3 Fundamental of LPP and research motivation

The LLP scheme has been developed for contact type [50,51], scanning type [52], and transmission type [53] SXM, due to its feasibility for all kinds of laboratories. This potential serves as a catalyst for our commitment to advancing the development of a compact WW x-ray source, characterized by high intensity and cost-effectiveness. Moreover, the characteristics of the short WW emission pulse from LPP make contact-type SXM a preferred choice. Additionally, the x-ray-sensitive resist beneath the sample is easy to utilize, thereby saving costs and minimizing photon flux loss from the objective optics. Results from prior research series have demonstrated that laser-produced Au plasma is one of the promising candidates for an intense WW emission source.

In this chapter, the fundamental aspects of LPP are introduced, providing the motivations for the research presented in this work.

1.3.1 Initial ablation

The generation of the LPP for a solid target can be divided into several steps. Initially, particles at the irradiated region are heated into the vapor and ionized due to the energy absorption. The formation of ions contributes to the creation of an initial plasma. The temperature keeps increasing due to the following laser irradiation. This brings frequent collisions between ions and electrons, leading to an enhancement of electron density. When the electron density reaches the critical density, the incident laser cannot penetrate the critical surface, causing an energy deposition on the critical surface and a hot dense region generated within the plasma.

- **Thermal transfer**

The initial ablation of materials by the laser pulse can be described using a one-dimension two-temperature physical mode for electron and ion [54–56]. The spatial and temporal evolution of the electron and lattice (or ion if ionized) can be described as,

$$C_e \frac{\partial T_e}{\partial t} = -\frac{\partial Q(z)}{\partial z} - \gamma(T_e - T_i) + S \tag{1-11}$$

$$C_i \frac{\partial T_i}{\partial t} = \gamma(T_e - T_i) \tag{1-12}$$

$$Q(z) = -k_e \partial T_e / \partial z \tag{1-13}$$

$$S = I(t) A \alpha \, exp\,(-\alpha z) \tag{1-14}$$

where C_e and C_i are the heat capacities (per unit volume) of the electron and lattice. T_e and T_i are the temperature of electron and lattice. $Q(z)$ is the heat flux propagated in the z direction perpendicular to the target surface. S is the laser-induced heating rate expressed by laser intensity $I(t)$, surface absorptivity A (0 for no absorption, 1 for completely absorbed),

and the material absorption coefficient α (cm^{-1}). γ is the parameter characterizing the electron-ion coupling. k_e is the thermal conductivity. The equation (1-11) describes the variation of the electron temperature is connected to the thermal diffusion, lattice (ion)-electron interaction, and the laser heating. The thermal diffusion for lattice is negligible in the period, since the time scale is much longer.

When the thermal diffusivity $D = k_e/C_e$ can be considered as a constant, the electron cooling time $\tau_e = C_e/\gamma$ and lattice heating time $\tau_i = C_i/\gamma$ can be insert into Eqs. (1-11) and (3-10). To find the solutions, a series of initial and boundary conditions are used together with assumed laser intensity $I(t)$, T_e, and T_i at $t < 0$ have

$$I(t) = I_0 exp\,(\frac{t}{\tau_L})\Theta(z) \tag{1-15}$$

$$\Theta(z) = a\,exp(-\alpha z) + b\,exp(-\beta z) \tag{1-16}$$

$$T_i = \kappa T_e \tag{1-17}$$

Where τ_L is the laser pulse duration, a, b, κ are the constants of proportion. α^{-1} and β^{-1} are the optical penetration depth and heat penetration depth. Using the method described in [56], the heat penetration is then calculated as,

$$\beta^{-1} \approx (D\tau_{eff})^{1/2} \tag{1-18}$$

$$\tau_{eff} = \frac{\tau_e\tau_L(\tau_L + \tau_i)}{\tau_e(\tau_L + \tau_i) + \tau_L\tau_i} \tag{1-19}$$

where τ_{eff} is the effective heat diffusion time during laser irradiation. In the case of nanosecond laser pulse ($\tau_L \gg \tau_i$),

$$\tau_{eff} = \frac{\tau_e\tau_L}{\tau_i} \tag{1-20}$$

In this way, the initial ablation condition can be described [57].

- **Critical density**

The critical density is an important threshold where the laser cannot propagate into the plasma anymore, resulting in an energy deposition at the critical density region where heating is effective.

The critical density n_c for a laser with a frequency ω as given by,

$$n_c = \frac{m\omega^2}{4\pi e^2} \tag{1-21}$$

where *m* is the electron mass [58]. Therefore, a Nd:YAG laser pulse with a wavelength of 1064 nm can only penetrates the plasma when the electron density is lower than 10^{21} cm^{-3}.

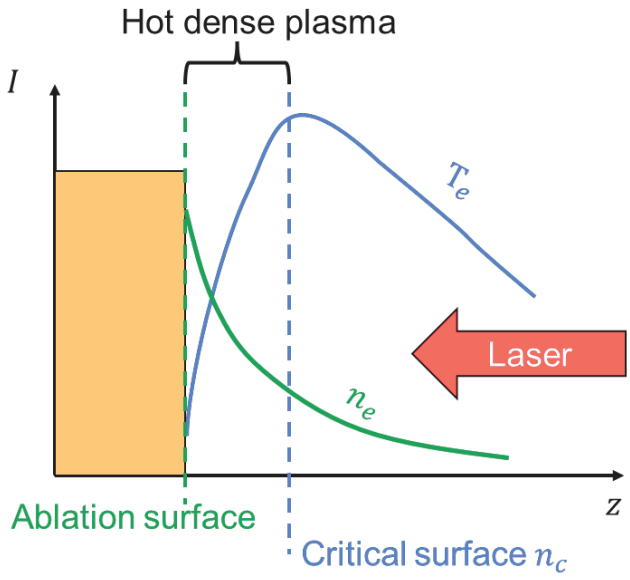

Fig. 20: Schematic of the critical density where laser can no longer penetrate. The energy deposited at this region, heating the plasma effectively.

1.3.2 Unresolved transition array from laser-produced Au plasma

In the LPP scheme, plasma is generated from laser–target interactions. The target material and shape strongly affect the x-ray emission yield. Two types of the emissions in the WW region are usually used for developing light source, line spectra from the low-Z elements and band/continuum spectra from high-Z elements.

For low-Z element targets, gas such as argon and nitrogen can emit strong line spectra in the WW region [59]. A comprehensive investigation for solid targets (Al, Si, Ti, Cu, Ta, and W) in [60] also revealed that emissions from low-Z elements (Al, Si, Ti, Cu) tend to be narrow compared to the high-Z elements (Ta and W).

These line emissions are effective for zone plates and multilayer mirrors, as these optics exhibit high reflectivity only within a narrow bandwidth specific to the wavelength of interest. Contrastingly, the grazing incidence mirror has a comparatively large bandwidth, making it suitable for chromatic emissions from high-Z plasma. Furthermore, the combination of the high-Z plasma and grazing incidence mirror makes it favorable for contact-type Scanning X-ray Microscopy (SXM), as the objective lens can focus chromatic lights.

Various target types for LPP, including foil [61,62], gas [63,64], liquid [65], foam [66], aerosol [67], and nanostructures [68,69], have also been reported for WW x-ray radiation.

According to the quasi-Moseley law proposed by Ohashi *et al*. [70], x-ray spectra emitted from plasma of high-Z elements exhibit strong radiative transitions from the highly

ionized ions, resulting in an unresolved transition array (UTA). The peak of the UTA emission from n=4-4 transitions in the elements with atomic number Z=50-83 was calculated, expressing as,

$$\lambda = (21.86 \pm 12.09) \times R_{\infty}^{-1} \times (Z - (23.23 \pm 2.87))^{-(1.52 \pm 0.12)} \qquad (1\text{-}22)$$

where R_{∞} is the Rydberg constant. The plot for this result is shown in Fig. 21. The elements lying in the blue region exhibit strong emission in the WW region. Atomic numbers ranging from 79 (Au) and beyond are predicted to be suitable for WW x-ray emission. However, considering the toxicity and radioactive, only Au and Bi can be practically used as the LPP target. Another strong UTA emission in the WW region is attributed to the n=4 - n=5 transitions in the highly-charged Au, Pb, and Bi plasma as illustrated in [71].

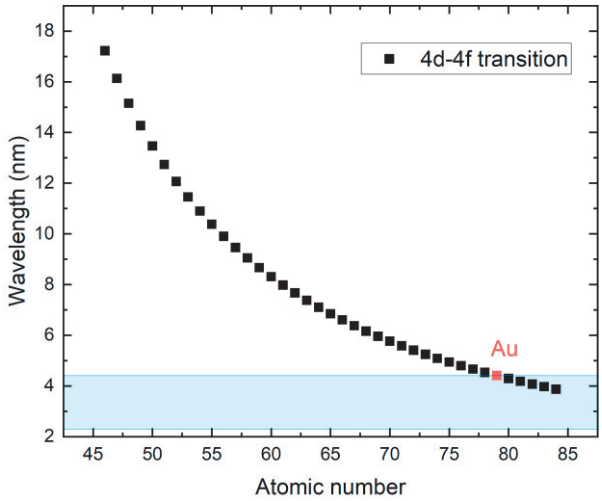

Fig. 21: The peak wavelength from 4*d*-4*f* transition for elements with atomic number Z=46-84, calculated by the quasi-Moseley law.

1.3.3 Enhancement of WW emission under N_2 gas atmosphere

One of the reasons that make laser-produced Au plasma essential for developing WW x-ray sources is, an emission enhancement from 2.9 nm to 6 nm was observed when adding a low-pressure nitrogen to the Au plasma [72]. A high-power laser was utilized to generate a 120 J/pulse energy, 600-ps duration pulse on an Au foil with a thickness of 200 μm. Nitrogen gas was introduced into the vacuum chamber during laser ablation, resulting in an enhancement of up to 5 times when the gas pressure was 400 Pa. This setup was applied to a contact SXM, achieving a spatial resolution of 80 nm with a photon number of 4.4×10^{11} photons/mm^2 in the wavelength of 2.2 - 4.4 nm. Although the laser energy was much stronger than that by the commercial laser device, the same results was soon reproduced using a compact commercial Nd:YAG laser.

Jonh *et al*. [73] have reported anomalous enhancement of WW emission from Au plasma

under a nitrogen gas atmosphere using a table-top Nd:YAG laser. Similar enhancement in the spectral intensity was observed using a grazing incidence spectrometer (shown in Fig. 22). The drop at 3.1 nm was attributed to the K-edge of nitrogen, which is possible to be suppressed if injecting the gas at a precise time before the laser ablating with optimal volume. The Auger electrons emitted from the nitrogen ions were considered to be the reason. The KLL Auger electron had an energy of ~360 eV [74], which excited the 4*f*-5*g* transition and its satellite transitions to emit WW x-rays.

The results strongly encourage efforts to develop a practical contact SXM utilizing the laser-produced Au scheme. However, the cost of the Au target can become substantial if multiple exposures are required for imaging, especially when employing a high-repetition system.

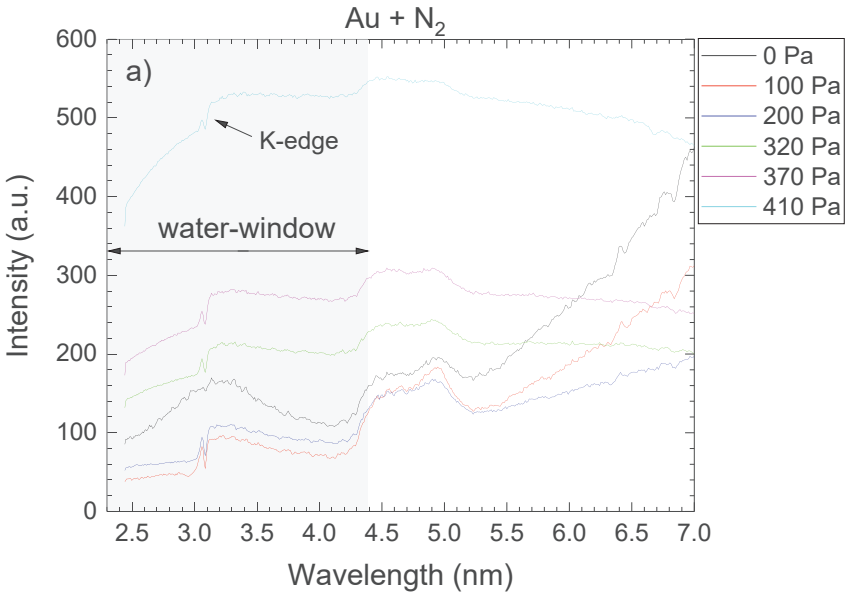

Fig. 22: Spectra generated from a laser-produced Au plasma under the nitrogen atmosphere with different pressures.

1.3.4 High-frequency tape target for SXM

To develop a practical WW x-ray source using laser-produced Au plasma, the target supply is one of the most important technical issues. For an Au target, foils can be employed as tape targets and irradiated at a 1-kHz repetition rate [75], making it possible to generate almost continuous WW emission. The prior research conducted at the Kansai Institute for Photon Science [76] successfully developed a laser-produced-Au-plasma-based contact SXM. A rotary disk composed of several samples was used to give attempts on developing a high-repetition imaging system (as shown in Fig. 23). However, replacement for the Au target limit the repetition, a tape target system was consequently craved to give a continuously plasma generation.

Thinner Au targets are favorable for x-ray emission, as they not only tend to yield less debris, which is essential for extending an x-ray mirror's lifetime, but also significantly reduce the cost of the expensive Au target. Although various WW radiation conditions for Au thin foils have been investigated [61,77,78], no optimal thickness for WW radiation has been reported yet. The optimal focus condition of the incident laser beam also needs to be clarified, as the spot size drastically changes the laser intensity (fluence) as well as the size of the generated plasma plume. In an LPP, self-absorption (radiation trapping) occurs, where the x-rays emitted from the center of the hot dense plasma are re-absorbed by the peripheral plasma [79,80]. Thus, the effective x-ray yield that can be practically utilized is reduced considerably. The absorption coefficient for the plasma and the absorption length are strongly coupled with the fraction of self-absorption [81–83]. As the initial plasma condition is determined by laser ablation, optimizing the irradiation conditions is important for increasing the system CE.

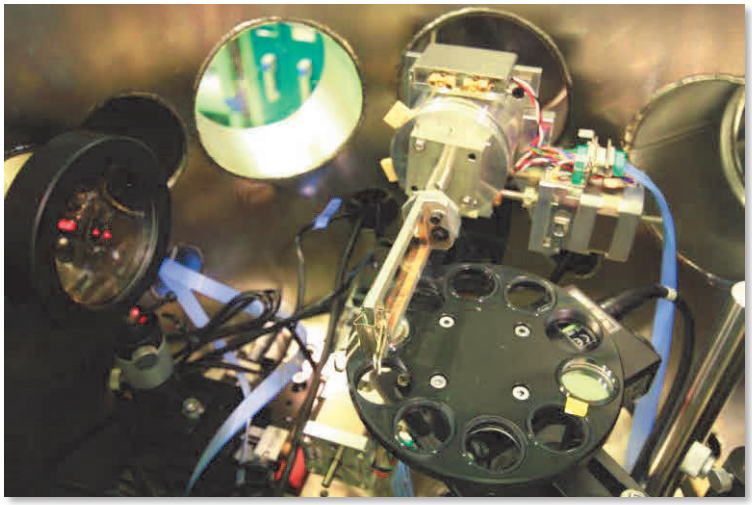

Fig. 23: Rotary sample stage and the Au foil target.

1.3.5 Objectives

In this work, WW UTA spectra emitted from Au laser plasma with different Au target thicknesses and laser focus conditions were investigated. The limit of Au layer thickness for a maximal WW emission with a fixed laser pulse energy was investigated. The optimal laser spot size at a fixed laser energy was also determined, where a larger plasma plume with a longer density scale length can emit more WW x-rays than a tight focus condition. Furthermore, the spatial distribution of the spectra in the Au plasma was investigated to efficiently utilize the light source.

2. EXPERIMENTAL SETUP

Experimental setup for studying laser produced Au plasma consisted of a driving laser beam line, a laser-target interaction vacuum chamber (3D overview in Fig. 24), and plasma diagnostic tools. The driving laser pulse having p-polarized with gaussian energy profile was focused into the vacuum chamber, where Au target and diagnostic tools were installed. Soft x-rays emitted from Au plasma were captured by several diagnostic devices to investigate the spectra, emission size/ shape, and other characteristics of the plasma. The overview of the experimental apparatus is shown in Fig. 25.

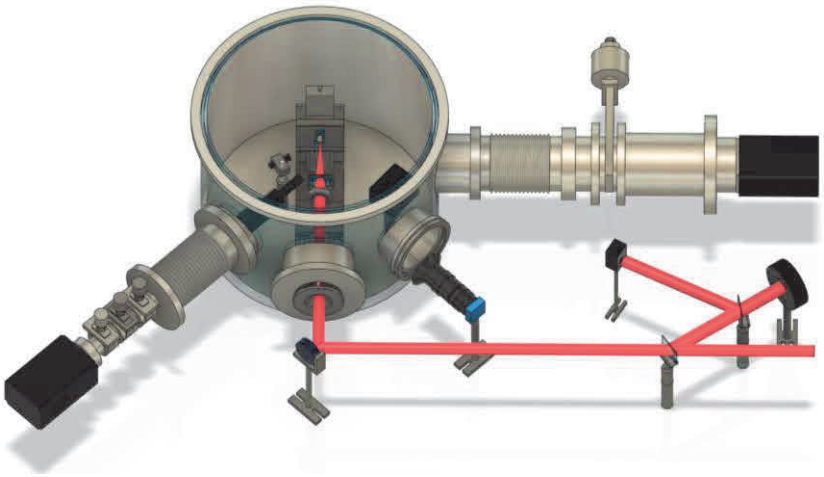

Fig. 24: 3D model of the vacuum chamber used in this work.

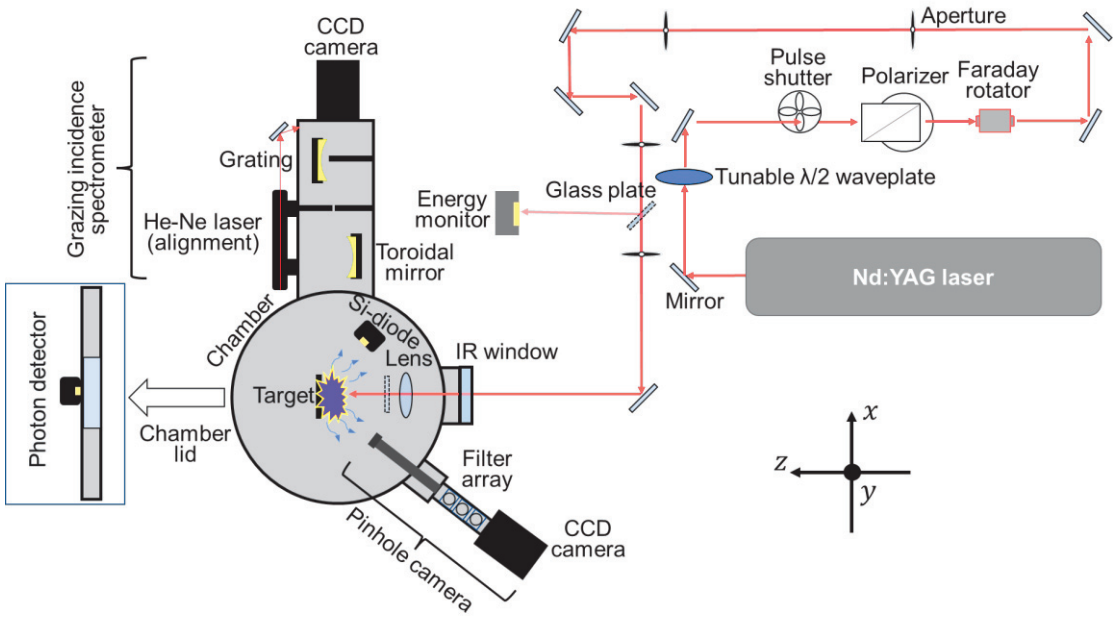

Fig. 25: Schematic of the setup for laser produced Au plasma.

The Au targets used for laser interaction were prepared in three different ways: commercial bulk target, foil target, and thermal evaporation target. Thicknesses of the targets were precisely controlled from 300 μm to 0.1 μm, ensuring the dependence of target thickness can be measured accurately. The setup details will be explained in the following sections.

2.1 Driving laser pulse

A table-top seeder-injected commercial Nd:YAG laser (Continuum Powerlite Precision II 8010, wavelength 1064 nm) was utilized as the driving laser for plasma generation. Laser pulse properties were measured as: pulse duration $\tau = 6.2$ ns, beam size= 7 mm (FWHM), wavelength 1064 nm, gaussian spatiotemporal profile. The laser was operated in 10 Hz, with a maximum energy of 1.65 J/ pulse. The view of Continuum laser and its inner structure is shown in Fig. 26 and Fig. 27.

Although the laser was operated by single shot mode in the system, the unignorable energy fluctuation caused by timing jitter made it unable to use. Since the continuous 10 Hz mode produced much more stable pulse train, an external mechanical shutter (Fig. 28) was set to pick up a single pulse, while the laser itself operated in a stable 10-Hz mode. The synchronization between the shutter and the laser pulse was achieved by connecting the laser's output flash lamp signal to the shutter's host. A pulse generator DG535 was added to fine-tune the timing of the shutter rotation movement.

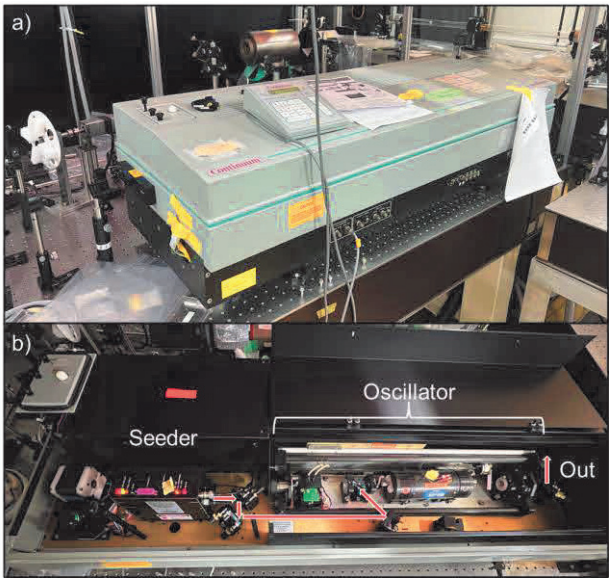

Fig. 26: (a) Continuum laser set on the optical table during the experiment. (b) Inside view of the laser device. The seed laser was generated from the seeder and led into the oscillator and amplifier. The arrows show the laser path in the device.

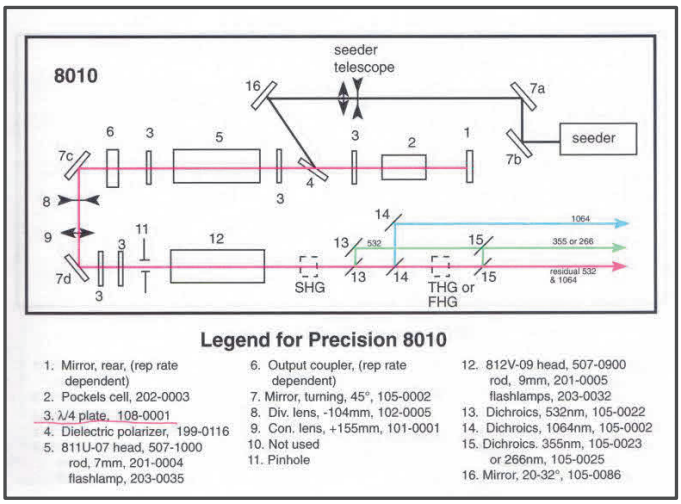

Fig. 27: Internal structure of the Continuum laser device.

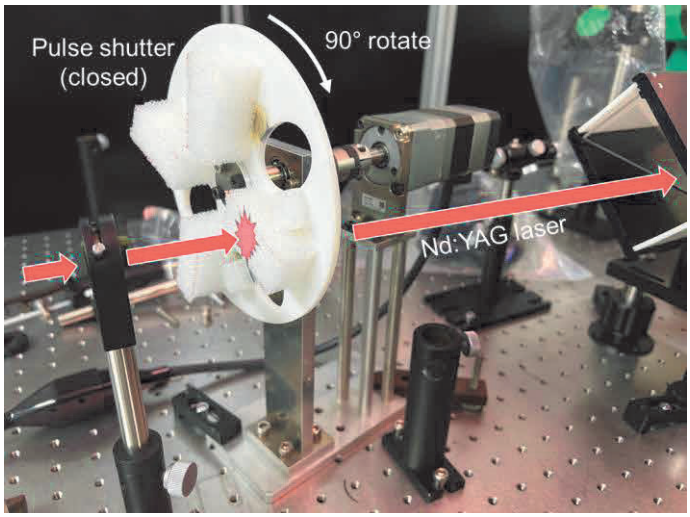

Fig. 28: View of the pulse shutter. The red line shows the laser beam path. The sponges pasted on the shutter blocked pulses while it was closed. When the rotate signal received, the shutter rotated 90 degrees to allow one pulse from the 10 Hz pulse train pass through the hole on the shutter plate between the two sponges.

Both Q-switch and flash lamp signals could be used as the trigger signal for the pulse shutter. However, the timing jitter from the Q-switch output signal was unignorable during the experiment, the vibrations and drifts in the sync output signal from the Q-switch made shutter cannot separate single pulse precisely. Therefore, flash lamp signal was selected as the trigger signal. Schematic of the setup is shown in Fig. 29, and the signal processing is illustrated in Fig. 30. The shutter started a reservation when received the “fire” command, waiting for the next delayed signal from the flash lamp. The delayed signal triggered the shutter, letting the second pulse pass through the hole on the shutter disk.

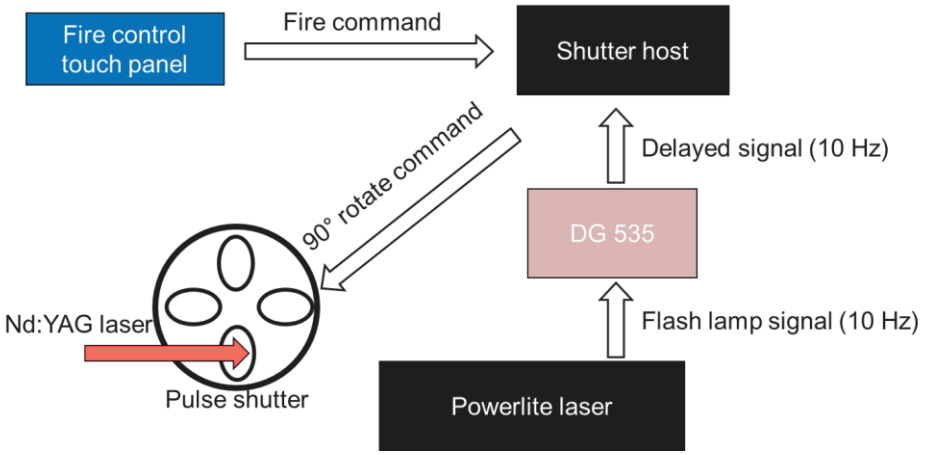

Fig. 29: Schematic of the digital pulse shutter.

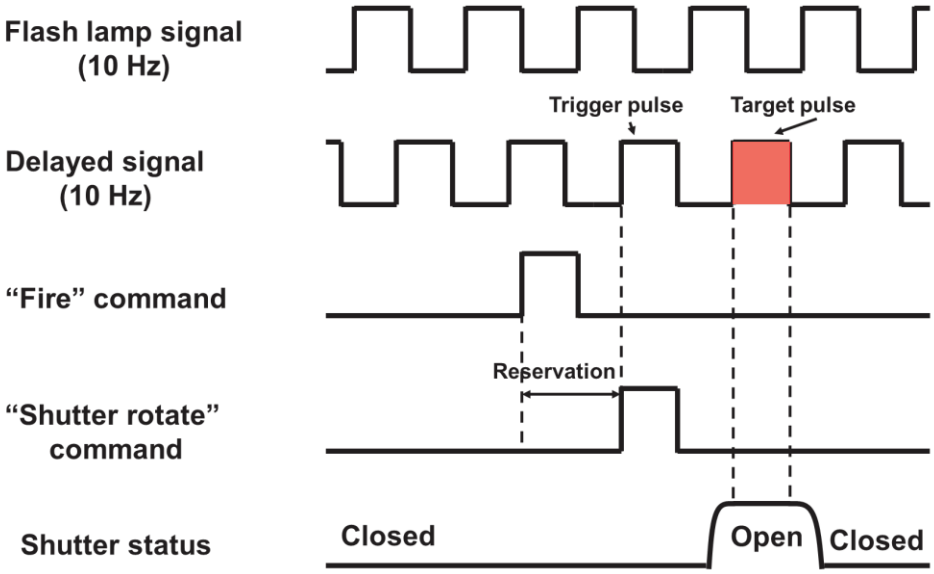

Fig. 30: Signal processing of the pulse shutter.

2.1.1 Optical isolator

The polarization of the normal incident laser beam in this experiment did not have an impact on the emission behavior and the size/shape of the hot dense plasma since the collisional absorption was dominant in the plasma and the polarization of the nanosecond pulse tail could be disturbed when propagating into the peripheral plasma. The laser light could only propagate into the plasma up to the critical density surface, so the partial unabsorbed laser light could be reflected at the critical surface. To prevent this reflection from backing into the laser cavity and cause damage, an optical isolator was set behind the pulse shutter. The set included a polarizer and a Faraday rotator (shown in Fig. 31).

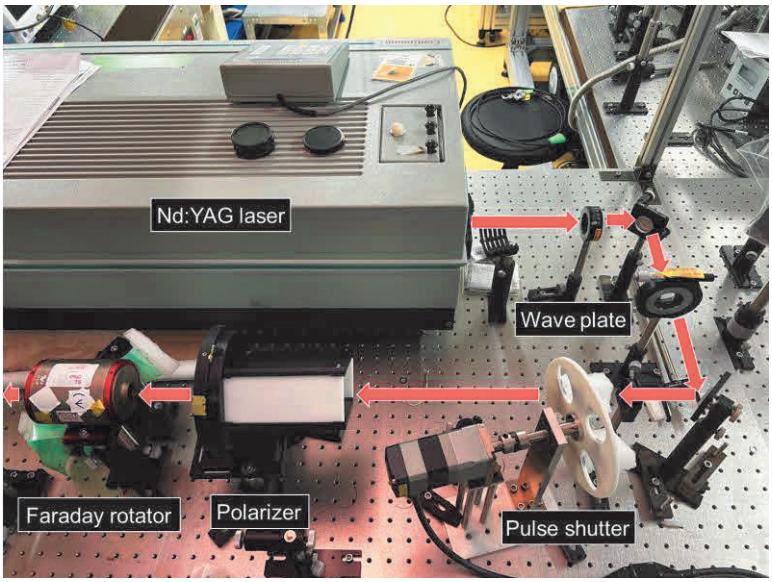

Fig. 31: Setup of optical isolator, pulse shutter, and wave plate.

The initial Nd:YAG laser pulse from the laser cavity had a horizontal polarization (s-polarized light). The optical isolator works as follows: the half-waveplate first adjusts the laser polarization into 45 degrees to fit the polarizer. After passing through the polarizer, it is rotated 45 degrees in the same direction by the Faraday rotator. The vertical polarized laser pulse propagates to the chamber, interacts with the target and plasma. The target surface and the plasma critical density surface reflects a small fraction of laser light back into the Faraday rotator and rotates 45 degrees again. Finally, the 135-degree polarized laser pulse can be fully blocked by the polarizer.

2.1.2 Fluctuation monitor

During the experiment, pulse-to-pulse laser energy could fluctuate due to the room temperature, humidity, and other parameters. To solve this problem, a glass plate was used as a beam splitter to split 4% laser energy from the beamline to the branch (shown in Fig. 32). A calorimeter (Gentec-eo Maestro) was set in this branch to monitor the pulse-to-pulse energy. The fluctuation was controlled within 10%.

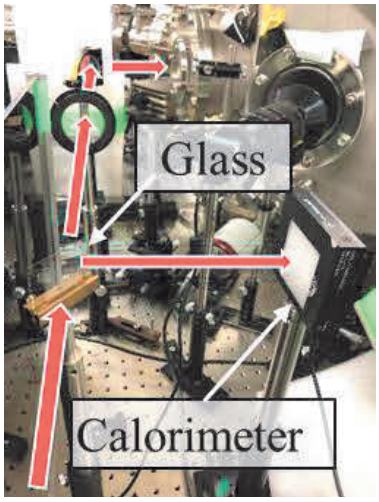

Fig. 32: Photo of the laser fluctuation monitoring branch in the beamline. The glass plate could split 4% of the laser energy to the calorimeter.

2.1.3 Spot size measurement

Accurately measuring the focused laser spot size is important for evaluating experimental results. However, the low laser-induced damage threshold of the CCD camera cannot stand for directly measuring the focused laser spot image. Also, the theoretical focused laser spot diameter, which will be calculated in Chapter 4, is several tens of micrometers. Since the CCD camera used in this experiment (Imaging Source, DMK 21AU04 Monochrome Camera) has a sensor unit size of 13×13 μm for each pixel, the original spot image on the camera would be only a few pixels which is difficult to evaluate. Therefore, a beam monitoring system that can reduce the laser energy and magnify the spot image into suitable size at the same time is constructed for the measurement (shown in Fig. 33).

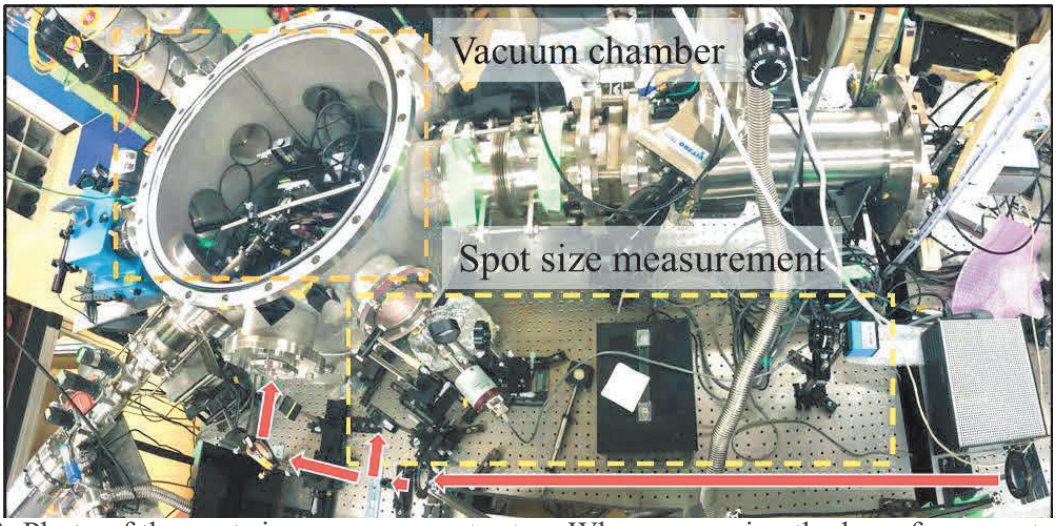

Fig. 33: Photo of the spot size measurement setup. When measuring the laser focus spot size, a mirror was placed in the main beamline, leading the laser propagate into the branch. After finishing the measurement, this setup was removed.

Details of the spot size measurement is shown in Fig. 34. The entire setup was regarded as a focusing system for reproducing the focused laser spot out of the chamber, and a magnifying observation system. Len 1 was an f=100 mm focus lens, which was also used in the chamber for later experiments. Lens 2 and the CCD camera were combined as a magnifying observation system, which could observe the spot size with a magnification of 6.5. The wedge glass and the IR attenuation filters were used for laser energy reduction. The tungsten wire (diameter 60 μm) served as a reference size indicating the focal point of the observation system.

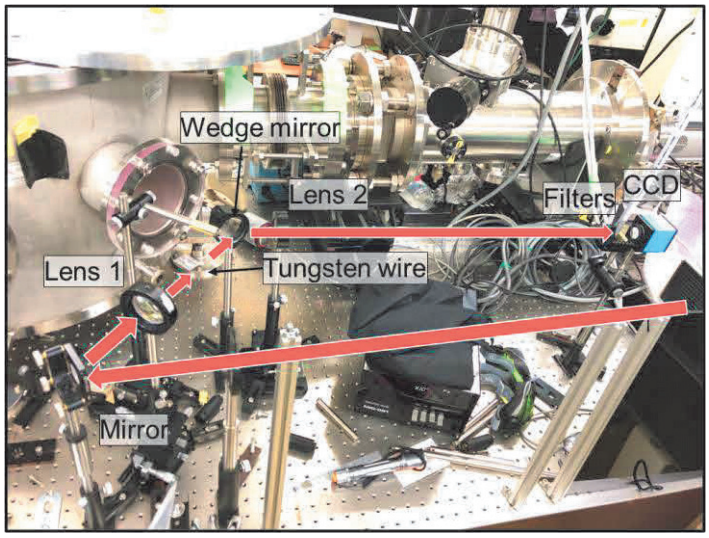

Fig. 34: Setup for the laser focus spot size measurement. Lens 1 was an f=100 mm focus lens, which also used in the vacuum chamber for laser focusing. The tungsten wire served as an auxiliary focusing reference to assist the CCD in finding the proper focus. The wedge mirror and the filters were used to weaken the laser energy for matching the CCD's energy threshold. Lens 2 functioned as a tunable focus lens to transmit the magnified laser spot image to the CCD sensor.

2.2 Plasma generation and diagnostic tools

The Au target and laser focusing lens for plasma generation were set in a vacuum chamber, connected with three diagnostic tools. The overview is shown in Fig. 35. The Nd:YAG laser pulse was delivered into the chamber through a coated SiO_2 window, focused by an f=100 mm lens on the Au target. A thin glass plate was set behind the lens as a protective shield to prevent plasma debris from damaging the lens. A grazing incidence spectrometer (GIS) was attached to the chamber perpendicular to the laser incidence direction, comprising an Au coated toroidal mirror (size: 50×30 mm^2), a 2400 grooves/mm flatfield grating (Hitachi, size: 50×30 mm^2), an entrance slit, and a back illuminated x-ray charge-coupled device (X-CCD) camera (Andor iKon-M 934, pixel size: 13×13 μm^2). A pinhole camera, consisting of a 25-μm pinhole, an x-ray CCD, and Ti filters (0.5- and 1-μm thicknesses), was installed at 45◦ to the target surface. A Si photodiode (PD; 400-μm pinhole, 1-μm-thick Ti filter) connected to

a charge amplifier was used to measure the integrated soft x-ray emission and was placed at 30 cm from the target surface in a 30° angle direction. The PD was triggered by another high-speed PD mounted on the top of the chamber, which received scattered laser light from the target as the trigger signal for the detector. Details are illustrated in the following sections.

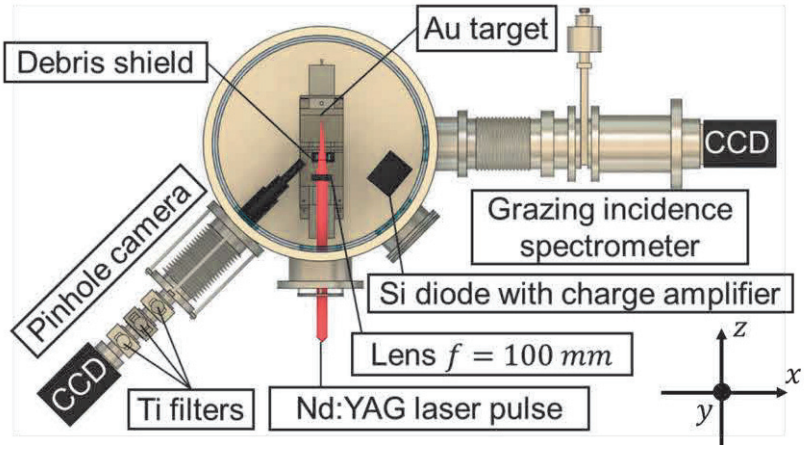

Fig. 35: Schematic of the plasma generation chamber and diagnostic tools.

2.2.1 Vacuum pump and pressure monitor

X-ray in the atmosphere pressure can be easily absorbed as shown in Fig. 36. To evacuate the vessel into an ideally pressure where x-ray absorption by air can be neglectable, vacuum pumping and pressure monitoring system were installed. Each pump set comprised a dry scroll pump connected a turbomolecular pump to keep the vacuum chamber under 10 mPa. The main pump set shown in Fig. 37 (b) and (h) (left) was connected to the target chamber, while Fig. 37 (c) and (h) (right) was connected to the GIS tube.

Chamber pressure was monitored by two pressure gauges plugged into the main chamber. The full range gauge (Fig. 37 (f)) operated as a cold cathode/ Pirani two-mode gauge, capable of measuring pressure over a wide range of 10^{-6}-10^{5} Pa. Another absolute pressure gauge MKS 626D served to measure pressure from 0.1 to 1000 Torr (~10-10^{5} Pa). Both gauges measured pressure without emitting x-rays, unlike hot cathode ion gauge, which ensured accurate plasma measurement.

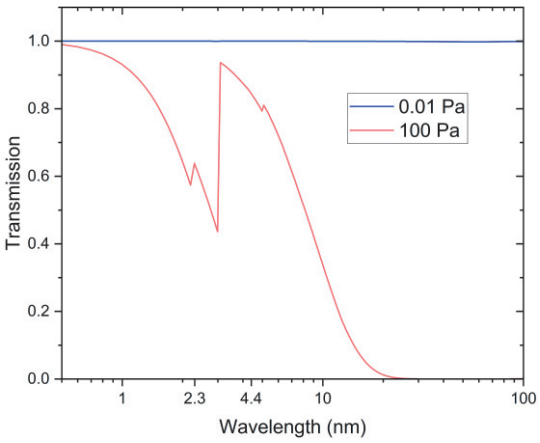

Fig. 36: Transmittance of short-wavelength light under a 30 cm path length at varying air pressures (0.01 Pa and 100 Pa) [1].

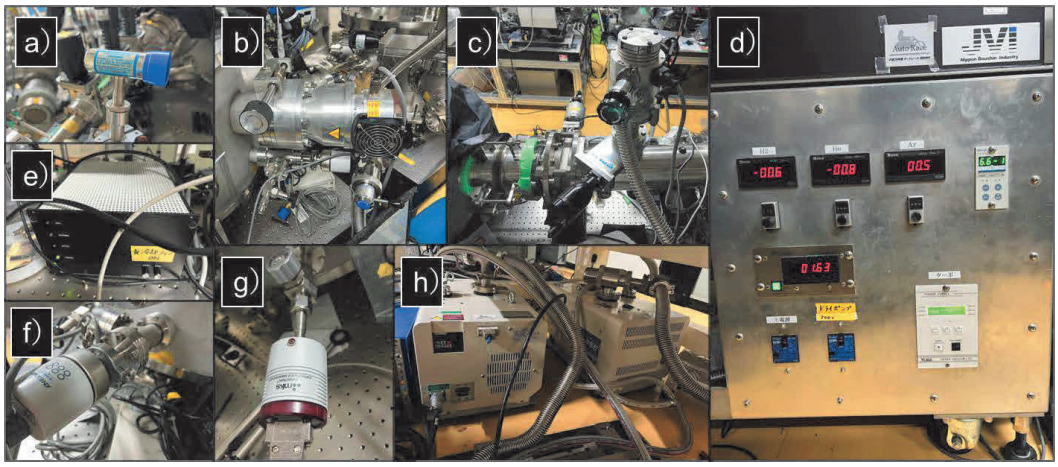

Fig. 37: a) Pressure gauge for pinhole camera pressure monitor b) Turbo pump for main chamber evacuation. c) Turbo pump for GIS. d) Control unit panel for pumps and pressure monitor. e) GIS turbo pump power source f) Canon Anelva PKR 251 full range gauge. g) MKS 626D 0.1-1000 Torr capacitance manometer. h) Dry pumps

2.2.2 Focusing and target system

Focusing lens, target, and debris shield were mounted on a multi-axis linear motorized stages which provided four degrees of freedom to the target and one degree to the lens, making it possible to achieve precise target-laser alignment. The linear stages were OptoSigma OSMS-X series which had a positioning accuracy of 3 μm. The lens and target were mounted on separate linear stages, all which were positioned on the same main linear stage, allowing for a 50 mm movement range for each component and 100 mm for the entire assembly in the direction of the incident laser (shown in Fig. 38). Au target was mounted on the target holder pressed by two holding plates. The incidence angle of laser beam was aligned using a precise square prism to be perpendicular to the target surface and the GIS observation direction.

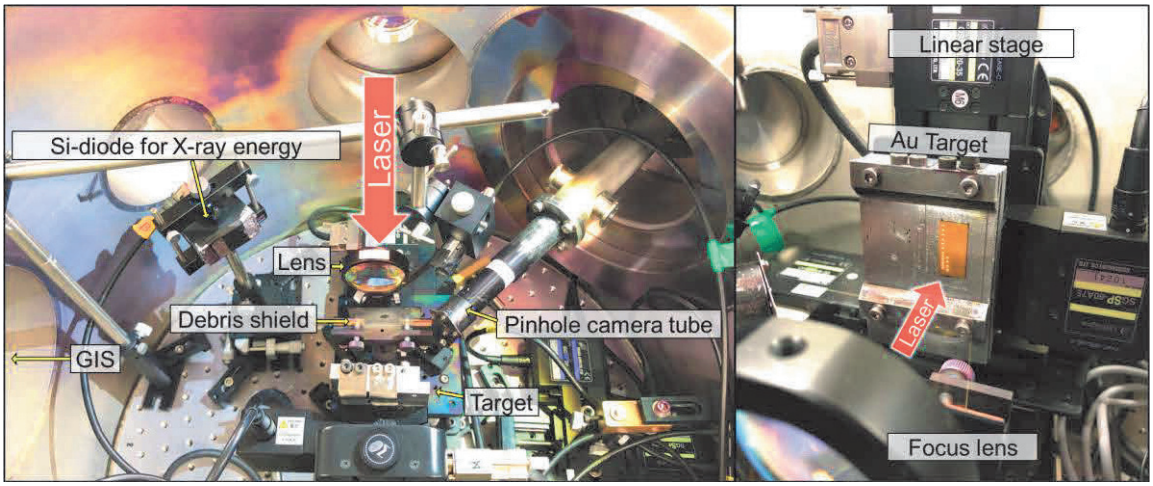

Fig. 38: Left: Top view of the vacuum chamber. Right: View of the target holder mounted on the linear stages. Au foil target was mounted on the holder.

2.2.3 Grazing incidence spectrometer

The GIS system was deployed following the equations described in the next chapter. Specific values and schematic are shown in Fig. 39.

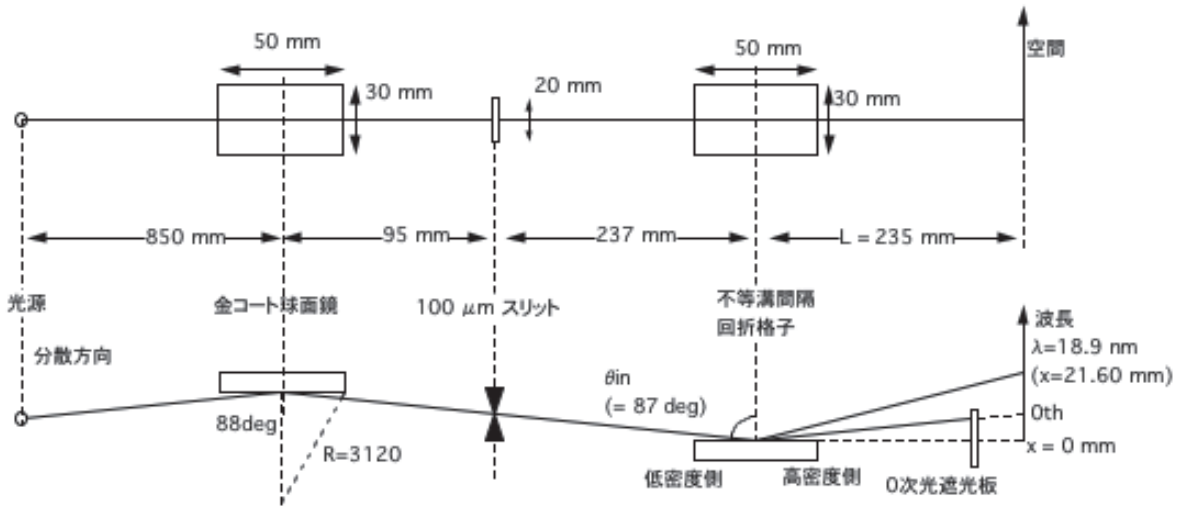

Fig. 39: Schematic of the spectroscopy principles in the GIS. The upper line shows the front view of the internal components. The lower line shows the top view. An example of the theoretical correlation between the wavelength and the x value is shown on the right side.

Schematic of the GIS is shown in Fig. 40. A toroidal mirror was set before the entrance slit to collect photons as much as possible, propagating toward the CCD sensor. This method could enhance the signal-noise ratio when dealing with the non-directional x-ray emission from the plasma. Two stray light blockers were placed to block stray lights generated from reflections in the chamber. A 0^{th} light cut mirror was set to block the 0^{th} light from the grating

and reflect He-Ne laser for the alignment. The GIS focus was aligned with the Nd:YAG laser focus point on the target surface, when the He-Ne laser beam pass through the center of the grating, the toroidal mirror, and focused on target surface where the focused Nd:YAG laser pulse irradiated.

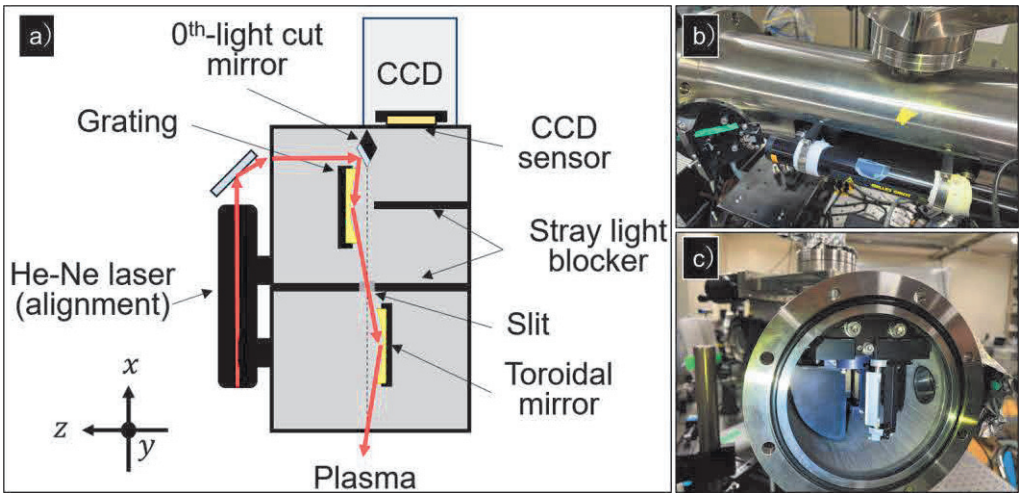

Fig. 40: a) Schematic of the GIS. Red arrows show the alignment laser path to the plasma diagnostic area. Dash line shows the center of the slit. b) Alignment laser mounted on the GIS. c) Inside view of the GIS

2.2.4 Pinhole camera

The pinhole camera was installed in the direction of 45 degrees to the target surface to measure the soft x-ray emission distribution and intensity (as shown in Fig. 41). The system comprised a pinhole cap, a tube mounted on a bellows for adjusting the angle, a filter array for selecting specific wavelength, and a CCD camera (Andor iKon-M 934, pixel size: 13×13 μm^2). Distance from the pinhole to the laser focus point was 75 mm, while the image distance was 1028 mm, giving a magnification of 13.7. The 25-μm pinhole used in experiment had a clear circular hole which transported pinhole images without significant deformation. The pinhole camera resolution determined by geometry and diffraction was 40 μm as calculated in Fig. 64. Glass and Ti filters were attached to the perforated valves, making it possible to adjust the observable wavelength during the experiments (shown in Fig. 42).

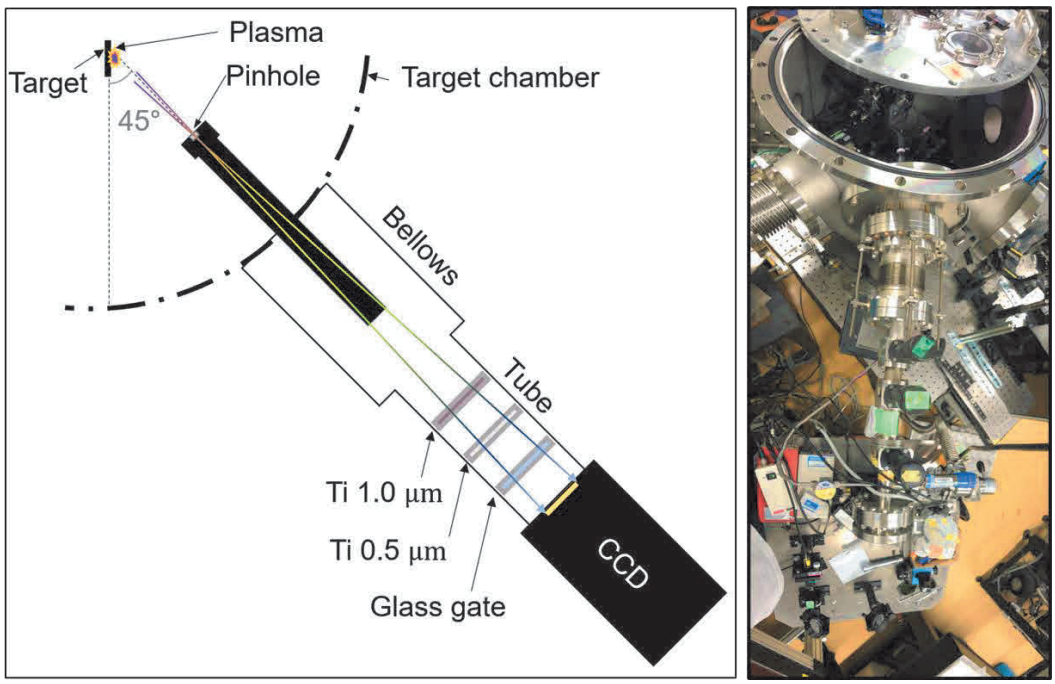

Fig. 41: Left: schematic of the pinhole camera. The colored arrow shows the path of emission from the plasma to the CCD sensor. Right: View of the pinhole camera during the alignment.

The reasons for setting the pinhole camera at 45 degrees are as follows. X-ray emissions from the LLP are nearly isotropic from the target surface though, the emission intensity is highly correlated with the emission angle. Due to the greater expansion of the plasma in the longitudinal direction compared to the transverse direction, the emissions are not homogenous in different directions. Moreover, it is difficult to achieve the alignment when using GIS and pinhole camera observe plasma perpendicularly from the target two sides, because of the focus characteristics of the toroidal mirror in the GIS. Therefore, observing plasma at 45 degrees is much more feasible, considering the x-ray emissions at 45 degrees also has higher intensity than at 90 degrees as studied in [84].

Fig. 42: a) Pinhole cap with the 25-μm pinhole. b) Ti-filter-attached perforated valves.

Two types of Ti filter were used to block out-of-band x-rays during the observation. The transmission of Ti filters with different thicknesses is shown below.

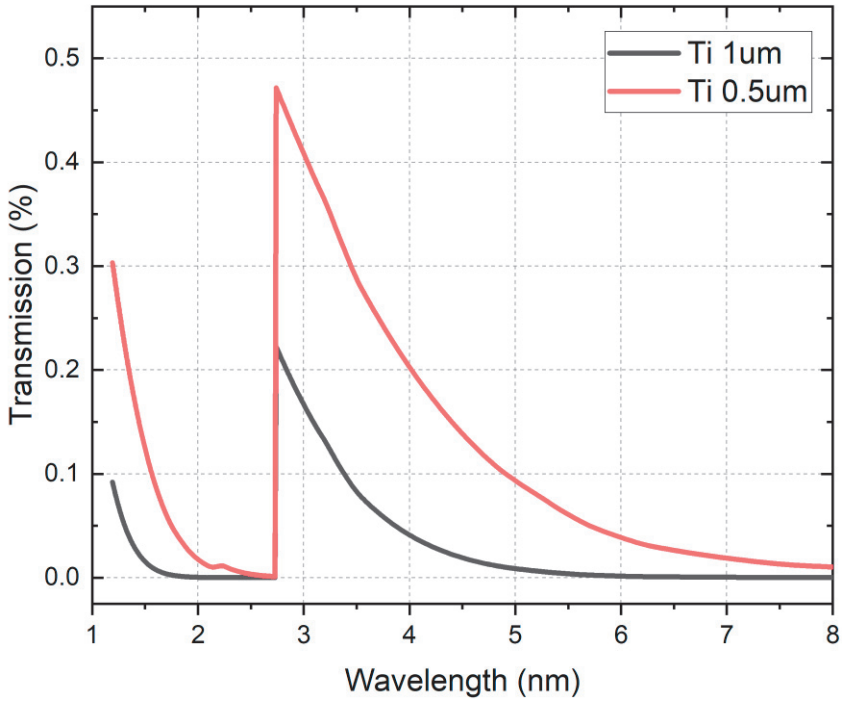

Fig. 43: Transmittance of Ti filter with different thicknesses. Black for 1.0 μm, red for 0.5 μm [1].

Besides the Ti filter, the sensitivity of CCD camera is important to perform a calibration for the pinhole camera system. Quantum efficiency for the CCD camera connected to the pinhole tube is shown in Fig. 44.

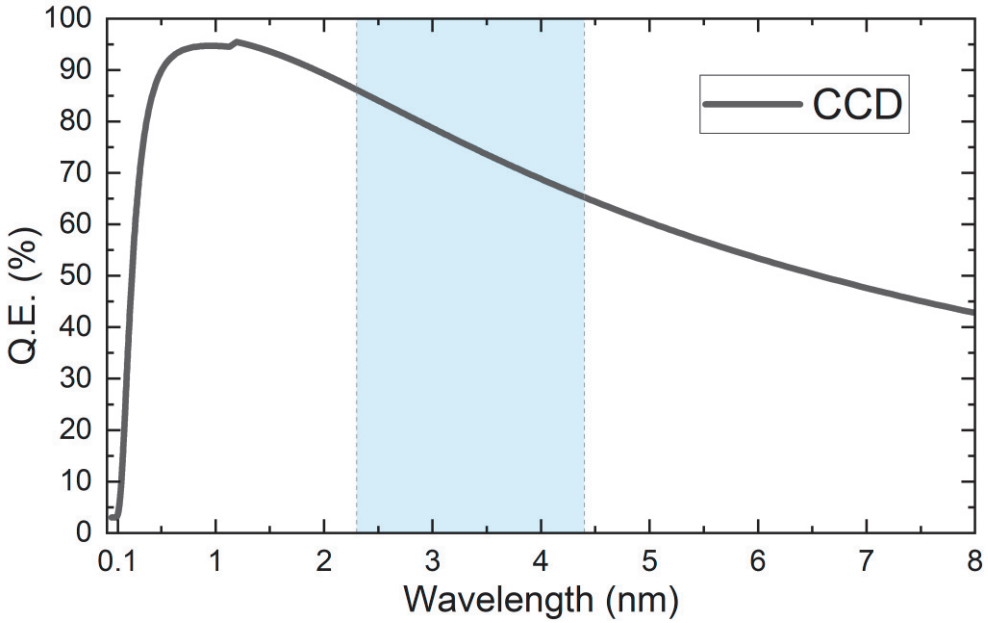

Fig. 44: Quantum efficiency datasheet for Andor ikon CCD camera. The dot-dash line in green corresponds to the efficiency of the back-illuminated CCD camera used in this work.

2.2.5 Soft x-ray detector

A soft x-ray detector assembled by a Si diode (Hamamatsu S3590), a 1-μm Ti filter and a charge amplifier (Hamamatsu H4083) was used to evaluate the soft x-ray intensity emitted from the Au plasma (shown in Fig. 45(a)). The detector was set at a 30-degree angle relative to the Au target surface, and the distance to the laser focus point was 30 cm. In the measurement, radiation from the plasma passed through a 400 μm pinhole, was filtered by a 1-μm Ti filter covering the detector sensor, and finally illuminated on the Si diode. Electric current generated by the electron movements inside the Si diode then produced a signal into the charge amp. The charge amp served as a signal amplifier and integrator to collect charge signals from the Si diode. Finally, the output signal from the charge amp was measured by a digital oscilloscope.

Although both power supplies for Si diode and charge amp were linear type, it was still necessary to address the filtering of high-frequency and low-frequency interference signals in the case of measuring nanosecond-scale x-ray signals. Therefore, several bypass capacitors and RC components were added in the circuit serving as band-pass filters to reduce noises. The circuit schematic is shown in Fig. 45(d).

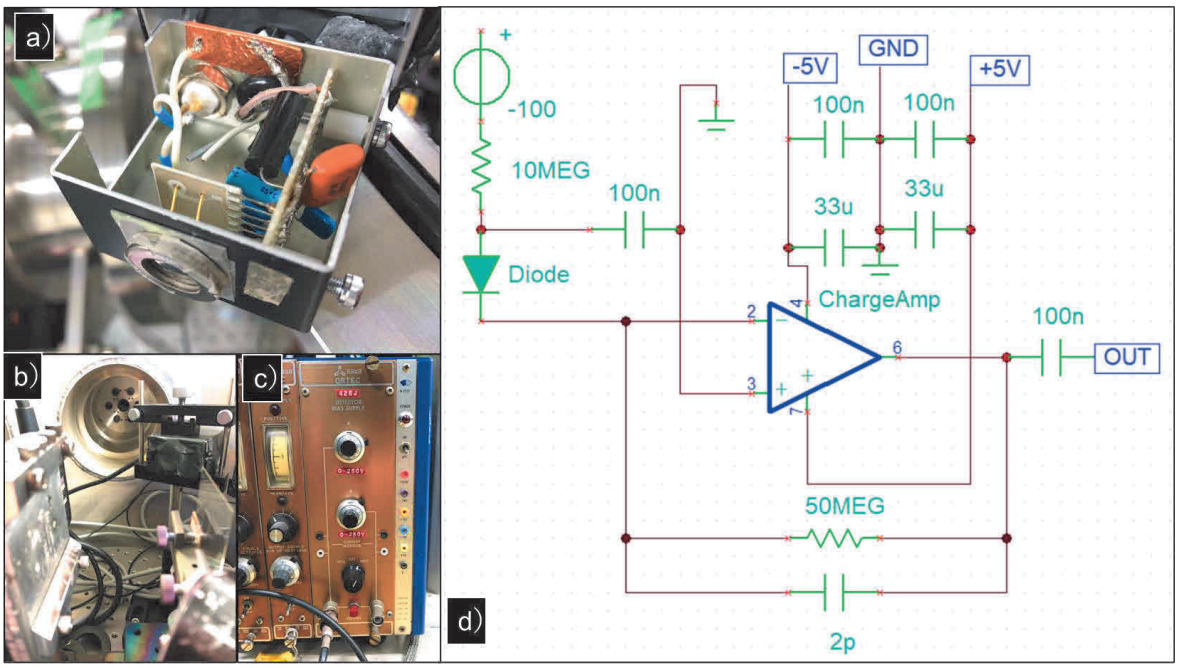

Fig. 45: a) View of the assembled soft X-ray dose detector. b) The detector set in the chamber. c) ORTEC 428J bias power supply used for producing -100V voltage for the Si diode. d) Equivalent circuit of the detector.

The basic idea for noise filtering is to lead all noise ripples in the circuit into the ground and ensure the signal from the diode could finally be introduced into the oscilloscope. The capacitor is widely used in such kind of scene to pass AC signal but block DC signals. For the capacitor, its capacitive reactance X_c is inversely proportional to the frequency, which is given as,

$$X_c = \frac{1}{2\pi f C} \ [\Omega] \qquad (2\text{-}1)$$

where f is the frequency (Hz), C is the capacitance of the capacitor (Farad). For the capacitors added between +5V, -5V, and GRD in Fig. 45(d), their capacitive reactance approached infinity when the DC power supply was applied as f=0. While for the high-frequency noise, the capacitive reactance acted as $X_c \longrightarrow 0$ which leads the noises to the ground. For the 100 nF capacitor connected in series at the circuit output Fig. 45(d), similar process is utilized.

For the RC (Resistor-Capacitor) component added between -100 V DC power supply and the Si diode in Fig. 45(d), the component serves as a band-pass filter to block typical frequencies noises. To explain how the filter works, equivalent series resistance (ESR) and equivalent series inductance (ESL) in the actual capacitor should be considered besides its capacitive properties, because of its internal components' characteristics. The impedance of the capacitor in the circuit is then derived as,

$$|Z| = \sqrt{ESR^2 + (2\pi f \times ESL - X_c)^2}\ [\Omega] \qquad (2\text{-}2)$$

This results in that (1) X_c dominates when the frequency is low. (2) ESL dominates when the frequency is high. (3) The impedance reaches its extremum when $2\pi f \times ESL = X_c$, which is known for the self-resonance frequency. In the actual case, the ESL and ESR value varies depending on the frequency. This variation is plotted in Fig. 46 [85].

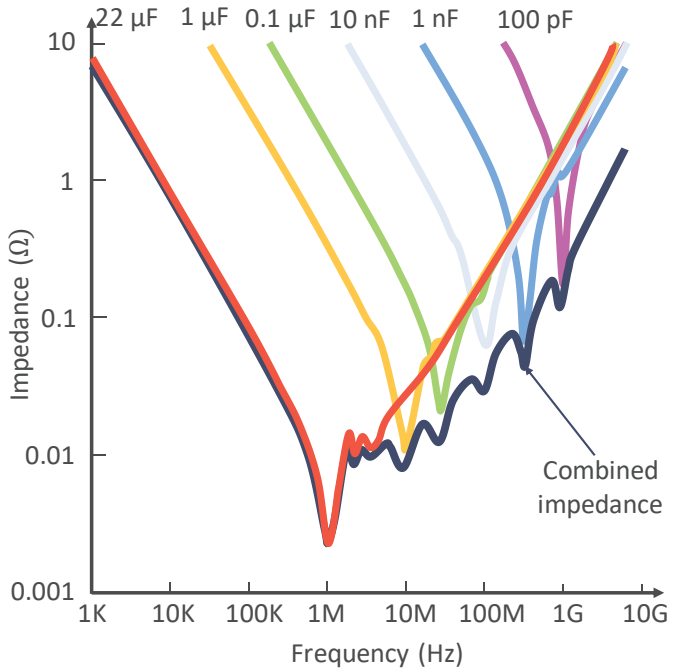

Fig. 46: An example of impedance characteristics when paralleling multilayer ceramic capacitors with different capacitances. Black line shows the combined impedance [85].

By utilizing the optimal combination of capacitors, it is possible to attenuate noise at specific frequencies while allowing the charge amplifier signal to be output.

2.2.6 Surface assessment tools

Surface assessment tools, including an Atomic Force Microscope (AFM) and a Scanning Electron Microscopy (SEM) with Energy Dispersive X-ray Spectroscopy (EDS) were employed to evaluate the surface roughness and post-laser irradiation effects on Au targets.

- **AFM**

A Scanning Probe Microscope SPA300 (AFM type, Seiko Instruments Inc.) (Fig. 47(c)) was used to scan the surface conditions of the Au targets. It was set to Lateral Modulation Friction Force Microscope (LM-FFM) mode. A triangular-shape cantilever with a length of 200 µm was used to scan an area of $150\ \mu m \times 150\ \mu m$ in a scanning speed of 1 Hz.

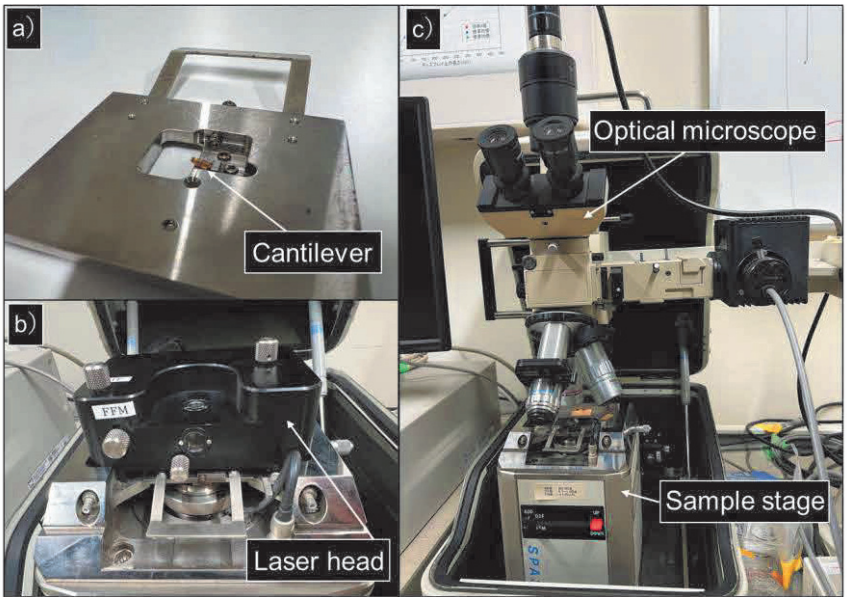

Fig. 47: a) Cantilever mounted on the lever head. b) Laser head covered on the cantilever head over sample stage while diagnosing. c) Locate the assessment area of the sample using optical microscope.

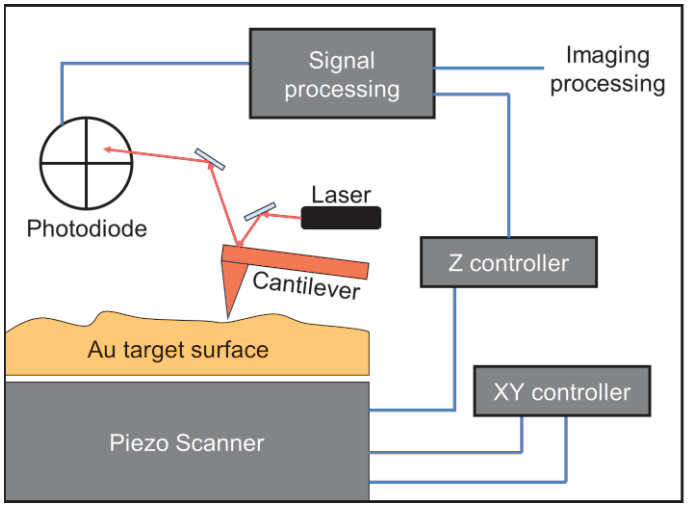

Fig. 48: Schematic of the AFM signal processing.

The AFM utilized forces between particles, such as van der Waals forces and electrostatic forces, to detect surface condition of objects. As the cantilever (Fig. 47(a)) approached to the sample surface, it continued to vibrate during the scanning process. The repulsive force from the sample surface subsequently induced an error in the cantilever's vibration. On the other hand, a laser head (Fig. 47(b)) was positioned above the cantilever, irradiating laser beam onto the tip of the cantilever, which was then reflected onto a photodiode. This error motion led to a displacement of the laser light on the photodiode. Ultimately, this

displacement signal was processed and output to create the scanning imaging, while concurrently transmitting signals to the z controller to maintain the distance between the cantilever and the sample. The schematic diagram is shown in Fig. 48.

- **SEM with EDS**

The SEM was utilized to evaluate the crater on the Au surface after laser irradiation. Due to the presence of explosive Au residues around the crater caused by shockwaves, these remaining components cannot be scanned by AFM. The SEM emitted an electron beam onto the sample surface, resulting in collisions that generated secondary electrons from the inner shell of the sample atoms through inelastic interactions. These secondary electrons were collected and processed by an Everhart-Thornley detector to create a 3D image of the sample surface.

In addition, an EDS detector integrated with the SEM was also used to obtain information about elements distribution on the sample surface. The electron beam emitted from the SEM could also interacted with the electrons in the inner shell orbits of the sample atoms. When an inner shell electron was ionized due to the collision, another electron from the outer shell would fall into this lower energy level, emitting characteristic x-ray with specific wavelengths. The EDS system measured these characteristic x-rays to identify the elements distribution on the sample surface.

2.3 Target preparation

During the experiment, size of the laser spot could reach 15 μm FWHM when target surface was set exactly at the focal point of the lens, bringing the potential optimal Au thickness range to several micrometers level or even lower. Depending on the thickness ranges, three types of Au were utilized to produce Au targets: bulk, foil, and deposition. The target stage was vertically/horizontally moved for each laser pulse irradiation, shot by shot, and then advanced to the next line once the available space was exhausted.

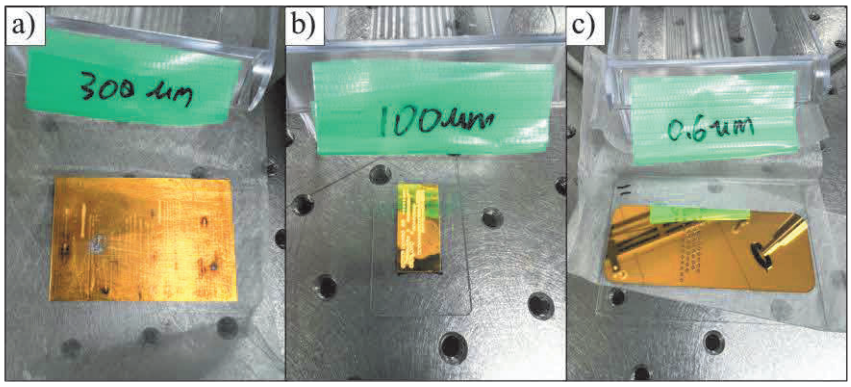

Fig. 49: Three types of Au target: (a) Bulk target (b) Foil target (c) Deposition target.

- **Bulk target**

A bulk Au target with a thickness of 300 μm was employed for the initial optical system alignment during the experiments. The main challenge in its use was its high cost, exceeding 30 thousand yen per unit. Additionally, its thickness posed difficulties in bending it into a perfectly flat shape.

- **Foil target**

Commercial Au foils (Nilaco Corporation) in size of 100 mm × 100 mm were purchased for targets. Their thicknesses were 100 μm, 80 μm, 50 μm, 30 μm, 20 μm, 10 μm, 5 μm, 2.5 μm. The foils were produced by rolling machine, which could remain processing patterns on the foil surface. Procedures for foil targets preparation are shown in Fig. 50. It was necessary to adjust the Au size to fit the target holder mounted on the stages in the vacuum chamber. Therefore, Au foils were sliced into 25 mm × 12 mm, glued onto the glass substrate using the water-soluble foil deposit liquid (Acrylic ester copolymer). Initially, the glue was diluted and spread onto the surface of the glass plate using a writing brush. A uniform liquid surface was attained using an air gun. Subsequently, the Au foil was cut using a hammer and blade to ensure sharp and smooth edges. Tweezers were then employed to delicately transfer the Au slice onto the glass plate surface, ensuring the roughness of the target surface.

The size of each Au foil permitted a minimum of 30 laser irradiation shots. This selection of a suitable target area effectively reduced the frequency of chamber evacuation and the need for target replacement. The vertical interval of each shot varied from 750 μm to 2500 μm, depending on the crater left after laser irradiation. This variation ensured that there was no overlapping of laser shockwave regions between the two shots. The buffer area at the head of the foil was prepared for fine-tuning alignment after target replacement. While the shooting area was for data collection. Finished Au foil targets are shown in Fig. 51.

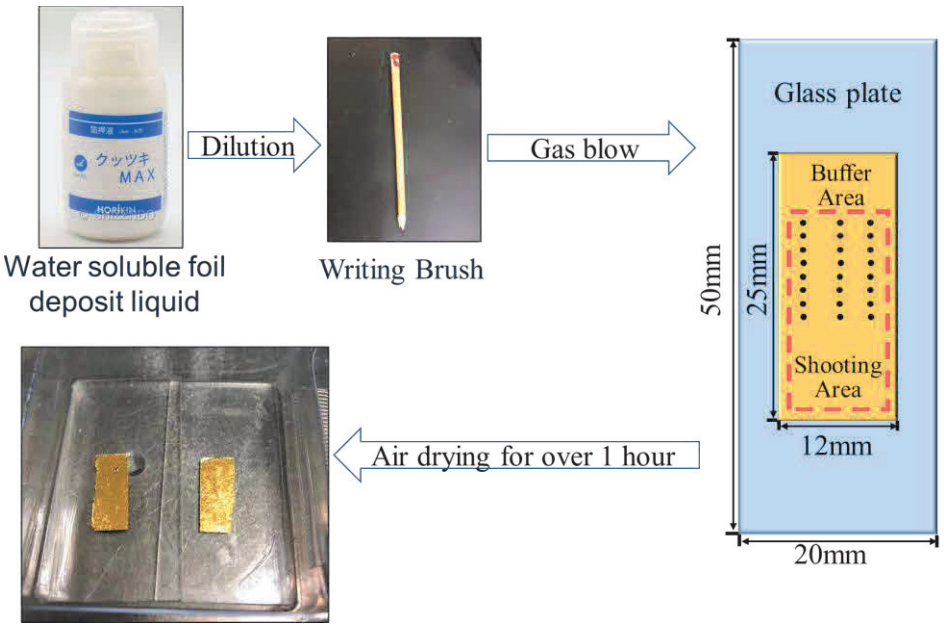

Fig. 50: Procedures for Au foil target preparation. The adhesive was diluted and applied onto the glass plate by using the writing brush. The consequent gas blow helped adhesive to form a more uniform distribution. Size of foil target was shown on the right. Photo of finished foil targets is shown at the end of the process.

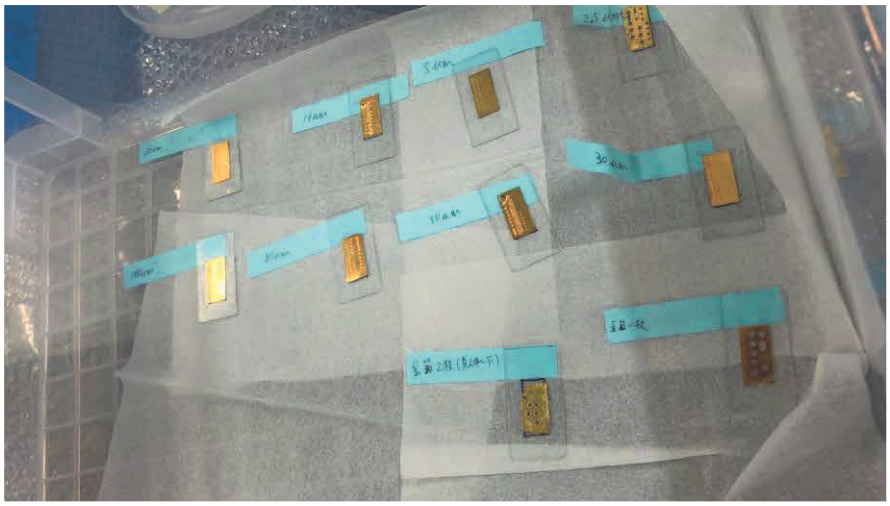

Fig. 51: Au foil targets with thickness label below. The two targets with label "金箔" were used as practice for target manufacture.

- **Deposition target**

Au thickness thinner than 2.5 μm became unreachable using the rolling method. Therefore, a thermal evaporation device was used to produce Au deposition targets with thickness under 2.5 μm. Thicknesses produced using this method were as follows: 1.8 μm, 1.3

μm, 1.0 μm, 0.8 μm, 0.6 μm, 0.2 μm, and 0.1 μm. The view of the device is shown in Fig. 52.

Fig. 52: a) Photgraph of the thermal vapor deposition device. b) Bright Au under heated by the tungsten holder below. c) Glass plate set on the substrate stage. The tungsten holder down below connected with high voltage power source. The mesh at the bottom prevented debris from falling into the cooling system.

The thermal evaporation was one of the common methods of physical vapor deposition (PVD) for thin film production. The device utilized high voltage applied onto a long-narrow tungsten holder to melt Au solid into vapor. Tungsten, with its high melting point of 3422 ℃, enabled the material holder to maintain a temperature exceeding 1400 ℃ for the evaporation of Au onto the glass substrate. The Au vapor rose and clung to the underside of the glass plate, which was placed at the hollow part (30 mm × 75 mm) of the substrate stage. The subsequent cooling coated the Au atoms onto the glass plate surface to form a film.

The entire process was conducted under high vacuum conditions to prevent impurities from mixing with the Au vapor. A combination of a rotary pump and an oil diffusion pump was utilized to evacuate the chamber to below 5×10^{-6} Torr (6.7×10^{-4} Pa), as illustrated in Fig. 53 (a). The rotary pump generated a low vacuum pressure, enabling the diffusion pump to function. Liquid nitrogen (Fig. 53 (b)) was introduced into the diffusion pump for oil trapping and to combine with water molecules.

Au film thickness deposited on the glass substrate could be controlled by changing the mass of Au particles placed on the material holder. The thickness of Au layer was calculated using the weight different before and after the deposition divided by the deposition area. The glass plate (size: 75 mm × 50 mm) cleaned by the ultrasonic cleaner was dried and weighed before deposition using an electric scale. After the deposition, the target was measured again after some time of cooling. The calculation was simply given by,

$$t = \frac{m_{after} - m_{before}}{S_t \times \rho_{Au}} \tag{2-3}$$

Here, t represents the thickness of the deposition layer, m_{after} and m_{before} are the mass of target after and before the deposition, respectively. S_t is the area of the deposited Au layer. ρ_{Au} is the density of the Au. Given the small deposition area, a uniform deposition surface was approximated during the thickness calculation. The deposition rate of the device was around 3% as calculated.

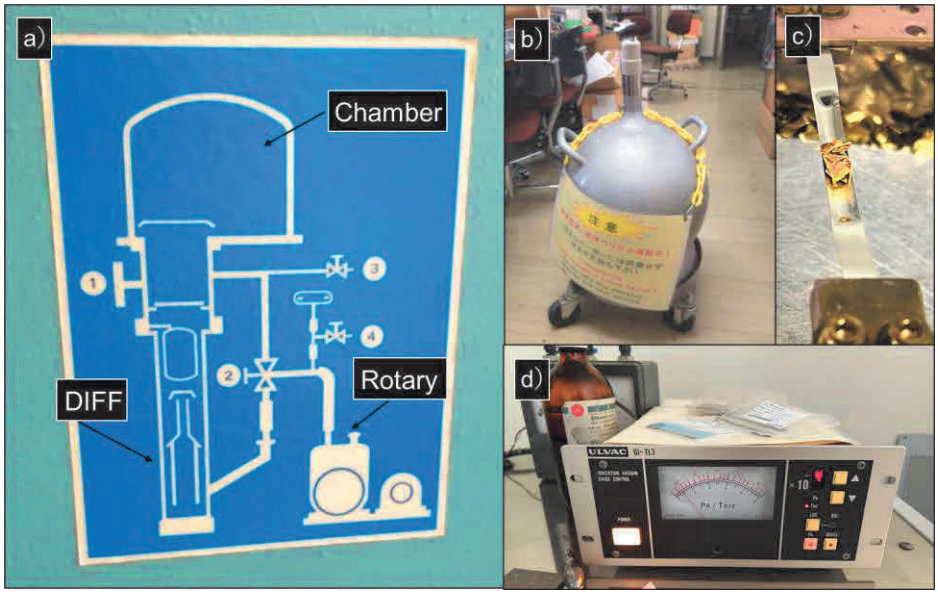

Fig. 53: a) Schematic of the thermal evaporation device. Vacuum chamber, diffusion pump, and rotary pump were marked in the figure. The 4 numbers refer to the gate valves for vacuum and exhaust. b) Tank for liquid nitrogen. c) Au particles lay on the tungsten holder. d) Ionization vacuum gauge.

3. RESULTS AND DISCUSSIONS

In this chapter, all experimental and simulation data obtained using the setups introduced in the previous chapter were discussed. Both raw data and analysis results are shown to deeply understand the interaction between laser pulse and target with various thicknesses.

The results are divided into four parts. The first part explains the fundamental aspects of laser-produced plasma, encompassing the characteristics of the initial pumping laser beam and emissions from the Au plasma. The second part delves into the spatial distribution of the Au spectra from the target surface, utilizing the GIS with a narrow-width entrance slit. The third and fourth parts present the optimal conditions for Au target thickness and laser focusing for WW x-ray generation. Experimental data are compared with simulation results to provide a comprehensive understanding of plasma emission behavior.

3.1 Fundamental aspect of Au laser plasmas

Before delving into the optimal conditions for WW x-ray generation, a thorough investigation of the basic properties of the laser pulse and Au plasma emission is necessary. The following measurements were conducted to ensure that all parameters were finely controlled during the experiment.

3.1.1 Characteristics of pumping laser pulse

The Nd:YAG laser pulse used for plasma generation was measured using the setup shown in 2.1. Although the laser device has a datasheet for pulse properties, time jitter in the oscillator, electromagnetic interference, and even thermal effects from the optical components could slightly affect the generated laser pulse. Fig. 54 shows the pulse width of the Nd:YAG laser at maximum laser energy with seeder injected. The FWHM of the pulse time evolution is shown to be 6.2 ns.

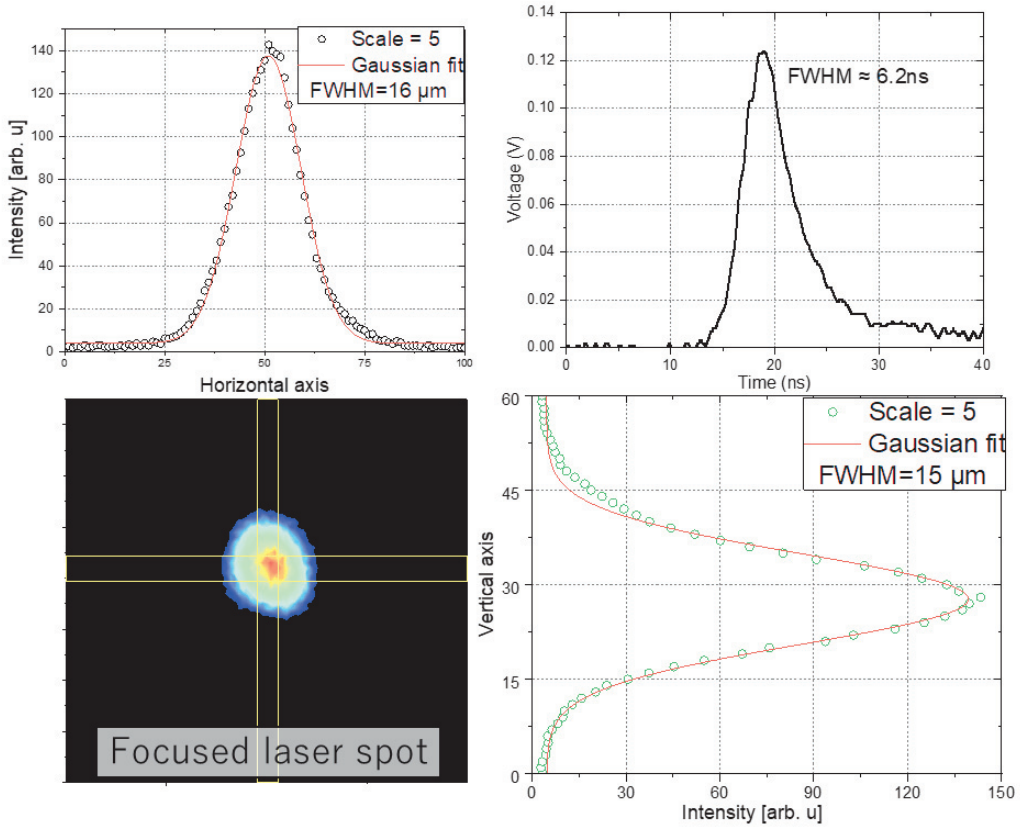

Fig. 54: Pulse width and cross-sectional profile of the Nd:YAG laser beam.

The laser intensity incident on the target was different based on the size of the focused laser beam. Typically, the target surface was positioned at the focal point of the focusing lens. Therefore, the focused beam size at the lens focal point was measured using a coated lens with a focal length of $f = 100$ mm. The narrow cross-sectional profile of the beam is also depicted in Fig. 54. With an initial beam diameter of 7 mm, the focused spot size was approximately 15 µm in FWHM, exhibiting a Gaussian spatial intensity distribution in both vertical and horizontal directions. The beam profile with a wider cross section range is shown in Fig. 55. The size difference in vertical direction could be explained by the aberrations and resolution limit during the spot size measurement. Because magnified spot image was measured using a zoom lens. The spatial resolution defined by the magnification rate and the pixel size of the CCD camera was 2 µm. Hence, the FWHM difference in the two directions was negligible.

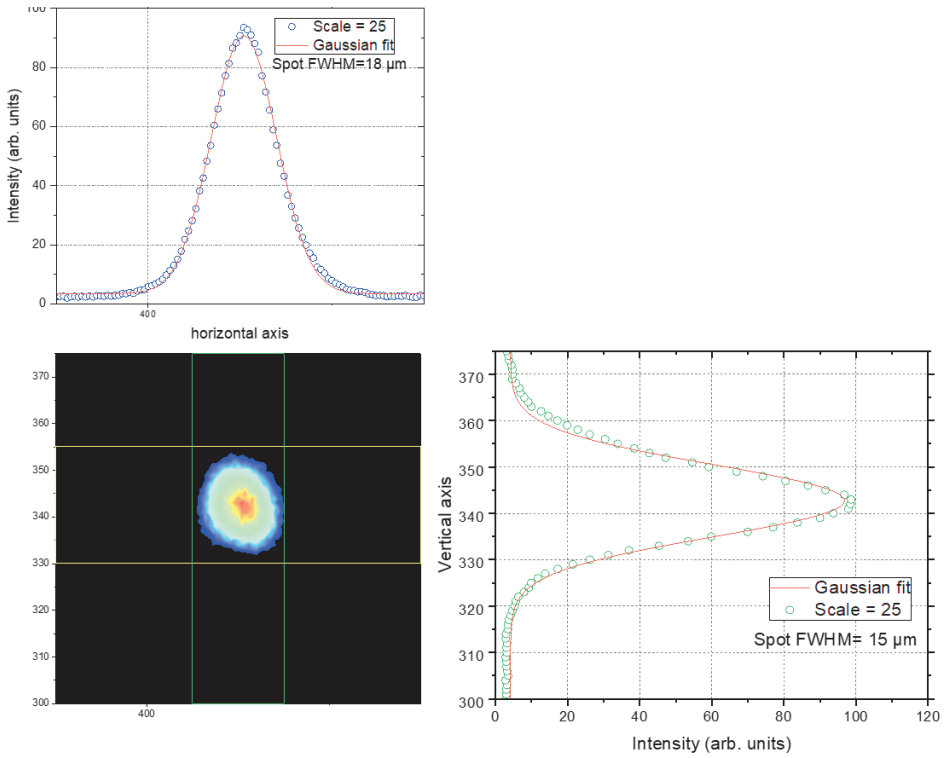

Fig. 55: Cross section of the laser beam in a wider range.

The adjustment for laser energy was performed using the optical filter as shown in Fig. 56 (a). In some cases, the optical isolator can serve as a linear laser energy tuner, as the energy blocked by the polarizer can be fine-tuned by the tunable wave plate. But a variation in the laser transverse electromagnetic mode (TEM) was found when tuned the polarization of the beam from full-pass direction into full-block direction. As depicted in Fig. 56 (b) and (c), The TEM_{00}-like beam spot was transformed into a TEM_{11}-like mode when the waveplate was rotated. This transformation was attributed to the fact that the laser energy blocked by the reflection-type polarizer remained partially on the glass plate, creating a thermal area where nonlinear effect influenced the beam pattern. This effect was initially negligible when most of the laser energy passed through polarizer but became significant as the blocked energy increased. As a result, IR attenuation filters were set behind the digital pulse shutter to control the laser energy during the experiment.

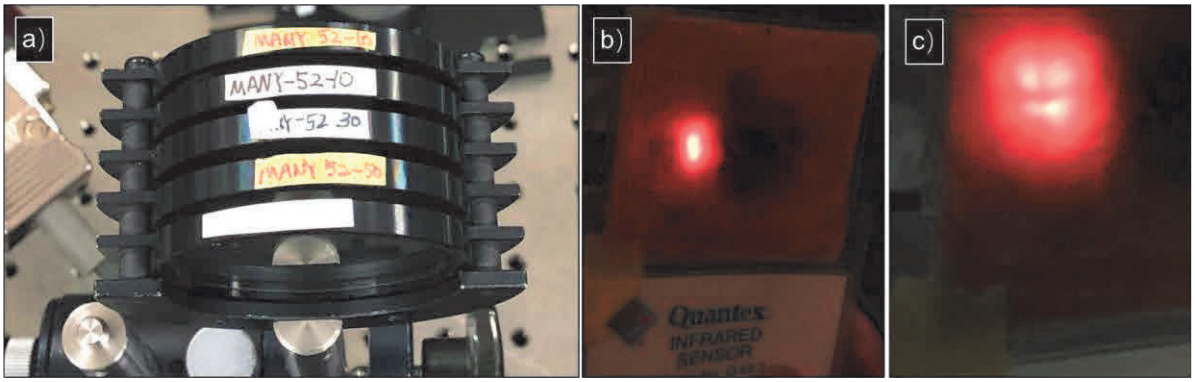

Fig. 56: a) IR filters for laser energy attenuation. b) The laser beam pattern observed by the IR card, when the laser polarization was parallel to the passing direction of the polarizer. c) The beam pattern observed when the laser polarization was changed to vertical with respect to the passing direction of the polarizer, by rotating the tunable waveplate.

3.1.2 Spectra from laser-produced Au plasma

- **Wavelength calibration**

The equations for wavelength calibration of a flat-field grating are described in the next section. However, the distance from the 0^{th} order light to the target wavelength was difficult to measure practically. Aberrations from the system could also affect the theoretical value as calculated. Consequently, a more practical method for the GIS wavelength calibration was performed using the well-known carbon line spectra from the laser-produced C plasma. As the H-like C spectra have been well studied and the database for the spectra is easily accessible from [86] (shown in Fig. 57).

Ion	Observed Wavelength Vac (nm)	Ritz Wavelength Vac (nm)	Unc. (nm)	Rel. Int. (?)	A_{ki} (s^{-1})	Acc.	E_i (cm^{-1})		E_k (cm^{-1})	Lower Level Conf., Term, J	Upper Level Conf., Term, J	Type	TP Ref.	Line Ref.
C VI		3.373417110	0.000000003		8.1219e+11	AA	0.0000	-	(2 964 353.25787)	$1s\ ^2S\ _{1/2}$	$2p\ ^2P^*\ _{3/2}$		T7771	
C VI		3.373957711	0.000000003		8.1273e+11	AA	0.0000	-	(2 963 878.2865)	$1s\ ^2S\ _{1/2}$	$2p\ ^2P^*\ _{1/2}$		T7771	
C V	3.4973	3.49728	0.00010	110	2.554e+11	AA	0.0	-	2 859 368.6	$1s^2\ ^1S\ 0$	$1s3p\ ^1P^*\ 1$		T5997	L1113
C V		3.49953	0.00010		1.946e+07	AA	0.0	-	2 857 530.3	$1s^2\ ^1S\ 0$	$1s3d\ ^1D\ 2$	E2	T3908	
C V	4.0268	4.02678	0.00010	450	8.873e+11	AA	0.0	-	2 483 372.8	$1s^2\ ^1S\ 0$	$1s2p\ ^1P^*\ 1$		T5997	L1113
C V		4.07283	0.00010		2.62e+04	A	0.0	-	2 455 293.2	$1s^2\ ^1S\ 0$	$1s2p\ ^3P^*\ 2$	M2	T1494	

Fig. 57: The example database containing Lyman-alpha series information from H-like and He-like C ions is accessible on the NIST website [86].

A bulk C target was used to produced C plasma. The Nd:YAG laser pulse with a maximum energy of 650 mJ irradiated onto the C target, producing H-like and He-like C line spectra as shown in Fig. 58. The spectra were observed using the GIS with a slit width of 350 μm. The upper figure in Fig. 58 shows the raw data obtained from the CCD camera. The background was subtracted before the data analysis. The horizontal direction refers to the wavelength diffracted by the flat-field grating. As derived in Eq. (3-22), a narrow width of the entrance slit can increase the wavelength resolution power. While increasing the slit width in

this case could enhance the throughput of the GIS. The heights of the vertical spectral lines in the raw image are proportional to the height of the light at the GIS entrance slit. This height, in turn, is proportional to the vertical length of the x-ray emissions from the plasma focused by the toroidal mirror.

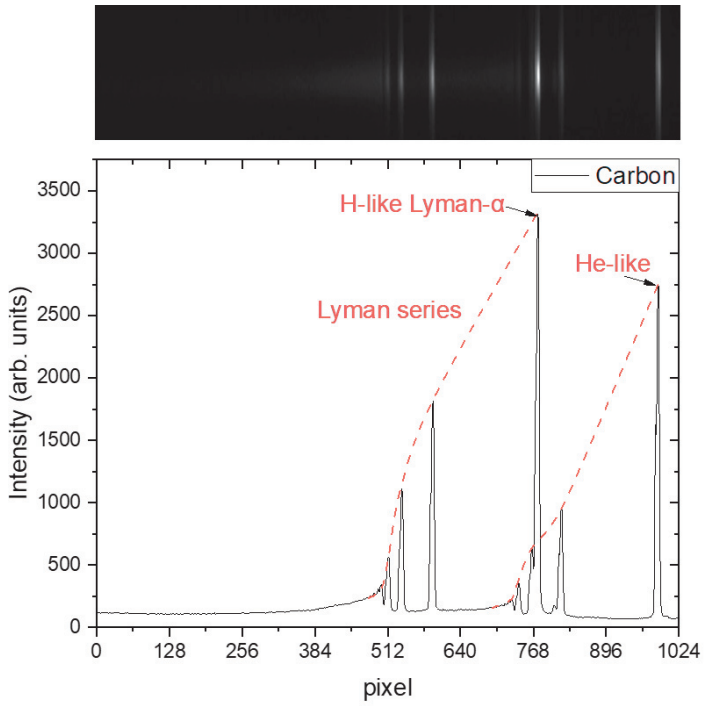

Fig. 58: C spectra observed by the GIS was used for wavelength calibration.

The lower plot in Fig. 58 was created by integrating the spectra from the raw image in the vertical direction. Lyman series spectra from H-like and He-like C ions are observed clearly in this case. Because the electron temperature was high when the laser was tightly focused on the C surface. Transition of 1s-2p attributed to H-like C ions is then dominated in the plasma emission, resulting in a strong line emission at around 3.37 nm. The second highest line spectrum is attributed to the $1s^2$-1s2p transition from He-like C ions. The line spectra following the Lyman-alpha line consist of the remaining transitions in the Lyman series, such as 1s-3p and 1s-4p.

Fig. 59 (a) shows the Au spectra in WW x-ray region [87]. The spectra were acquired by irradiating the bulk Au target (thickness: 300 μm) with laser pulses of 650 mJ (3.86×10^{13} W/cm^2) and 240 mJ (1.43×10^{13} W/cm^2), respectively. Different from the line spectra from C plasma, the broadband spectra are produced the UTA emission from the countless energy levels in the highly ionized Au ions. Two UTA spectra are observed as one is around 2 nm and the other one is beyond 4 nm, which are attributed to the different transitions from the Au ions. A slight drop at around 2.3 nm is observed, which is attributed to the K-edge of the O atoms present in the oxide debris adhering to the optical components in the GIS.

The small peaks on the spectra are attributed by the 4*f*-5*g* transition from different charged Au ions and their satellite transitions. The small peaks are more distinguishable in the high intensity spectra due to its high average intensity.

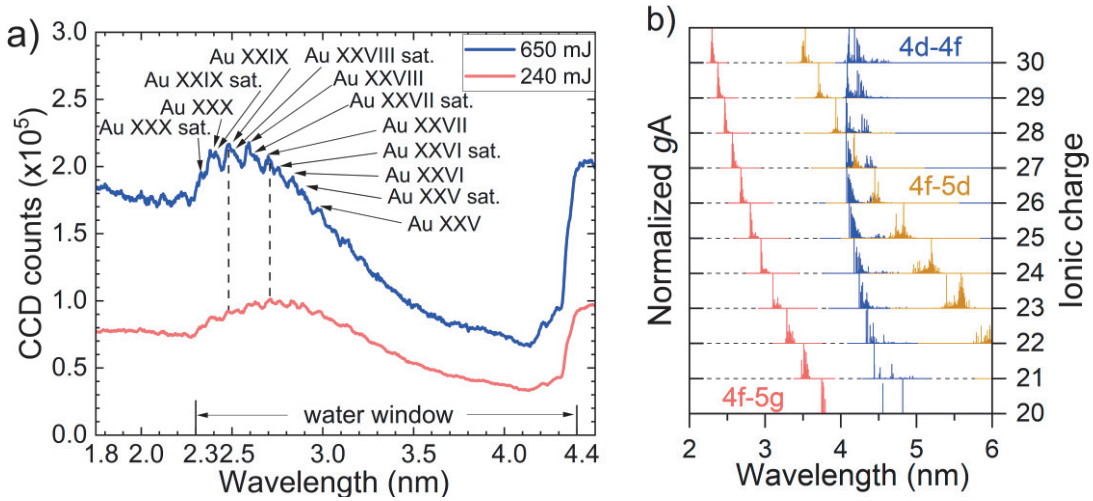

Fig. 59: a) Spectra for 300-μm-thick Au target produced by 650 mJ (3.86×10^{13} W/cm^2) and 240 mJ (1.43×10^{13} W/cm^2) laser pulses. Each line was averaged from 5 laser shots. Using the wavelength table [87], the charge states and surrounding satellite transitions were identified. The dashed lines indicate the peaks of the two spectra. (b) Weighted transition probabilities (gA) contributing to WW emission, calculated by FAC. The values of gA (product of statistical weight and transition possibility) for 4*d*-4*f*, *4f*-*5d*, and 4*f*-5g transitions from Au XXI to Au XXXI are shown.

Comparing the two spectra using different laser pulse energies of 650 and 240 mJ, a peak for 650 mJ irradiation case shifts from 2.7 nm to 2.5 nm (dash line shown in Fig. 59 (a)). To investigate this behavior, numerical calculations using the Flexible Atomic Code (FAC) [88] was conducted.

The FAC code is an open-source computational software package developed by [88]. It could generate weighted transition rate (gA) of a given single multipole's (element) initial and final states. Here, the g is the statistical weight of the upper level in the transition, and A refers to the Einstein coefficient for spontaneous emission. Wavelength of these transitions are also exported in the results, so it is helpful to evaluate the contributors to the spectra obtained from the experiment. However, the gA is normalized and one cannot be compared to the gA from other ionic stages or transitions.

The package employs a fully relativistic approach based on the Dirac equation, which allows it to calculate a wide range of radiative transition, direct collisional excitation, and ionization by electron impact nonresonant photoionization and radiative recombination, autoionization and dielectronic recombination. With the help of the incorporated collision radiative model, it is possible to construct synthetic spectra emitted from plasma under different physical conditions.

In Fig. 59 (b), the wavelength of x-ray emissions from the three calculated transitions in Au ions of 20+ to 30+ are shown in different colors. The normalized transition probabilities for each single transition at each single ionic stage are shown as the height of the emission line. While this simulation result cannot generate spectra with intensity distribution, it does allow for the confirmation of contributing transitions for the WW emissions at the corresponding wavelength.

The $n = 4 - 4$ and $n = 4 - 5$ transitions for Au ions mainly contribute to the UTA emissions in the WW x-ray region. Emissions from 4*f*-5*g* tend to be of shorter wavelength as the ionization state of the dominant ions increases. This is in a good agreement with the peak shift from ~2.7 nm to ~2.5 nm between the two Au spectra shown in Fig. 59 (a). Due to the higher electron temperature generated by the higher laser energy, more Au ions with higher ionization states are produced and the peak shifts to shorter wavelength.

A subsequent investigation into the incident laser energy dependency was conducted. Spectra generated by 100% (3.86×10^{13} W/cm^2), 30% (1.08×10^{13} W/cm^2), and 10% (3.86×10^{12} W/cm^2) of the energy from the 650 mJ laser pulse were observed and normalized, as depicted in Fig. 60. The intensity for each spectrum is rescaled to facilitate the comparison of their wavelengths at the peak. A clear peak shifting from 3 nm to 2.6 nm can be found as the laser energy increases. The emission wavelength distribution from 4*f*-5*g* transition in Au 20+ to 30+ are shown in black, illustrating the emissions from highly charge Au ions like 27+ and 28+ are gradually dominated in the plasma.

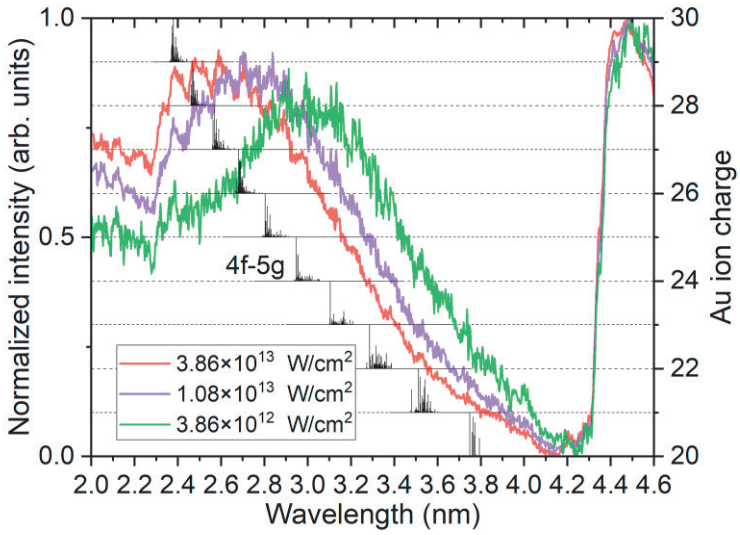

Fig. 60: Normalized Au spectra under different laser power compared with the 4*f*-5*g* transition probabilities from Au20+ to Au 30+ calculated by the FAC code.

3.1.3 Pinhole images of the soft x-ray emission

The pinhole camera proved to be a valuable tool for assessing the soft x-ray emission area and integral soft x-ray yield. The x-ray emission image captured by the CCD camera is used to evaluate whether the plasma expansion is nearly isotropic or not. Additionally, the total x-ray emission volume in the direction of the pinhole can be calculated.

The photons emitted from the Au plasma propagated into the CCD camera only through the Ti filter. Hence, it was possible to calculate the wavelength range that pinhole camera observed and the corresponding total photon numbers.

Since the Ti filter transmission (Q_{Ti}) is not perfectly matched with the WW region and

the CCD sensor has inconstant quantum efficiency (QE) ($Q_{\text{Q.E.}}$) within this wavelength range, the following calibration procedure is employed to specify the x-ray wavelength observed by the pinhole camera. The theoretical sensitivity of the pinhole camera is determined to be the product of the Ti filter transmission and the CCD quantum efficiency. The total sensitivity Q_{total} is calculated as,

$$Q_{total} = Q_{Q.E.} \times Q_{Ti} \tag{3-1}$$

Using the Au spectra obtained from Fig. 59 (a), reference x-ray spectra for emissions observed by the pinhole camera are calculated, shown as red and blue lines in Fig. 61 (a). According to the results, out-of-band x-rays, shorter than 2.3 nm or longer than 4.4 nm, still contribute significantly to the pinhole image after filtering by the Ti.

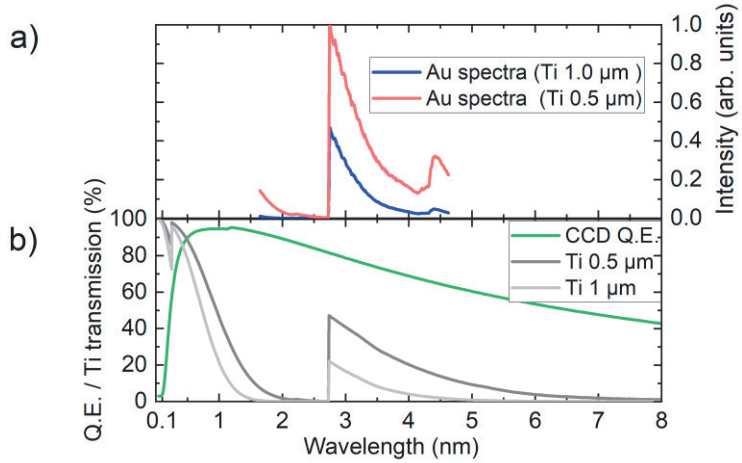

Fig. 61: (a) CCD QE and Ti foil filter transmission as function of wavelength (green and grey lines). (b) The Au spectra (650 mJ laser energy) in Fig. 59 (a) were used as reference spectra observed by the pinhole camera (blue and red lines).

Soft x-rays emitted from the Au plasma were observed through the pinhole camera with 0.5-μm and 1.0-μm Ti filters, as shown in Fig. 62. Intense soft x-rays are emitted from the center of the plasma, near the critical density region where the plasma is effectively heated by the Nd:YAG laser. The outer regions generate emissions from the subsequent expanded plasma, where the plasma is relatively cold and emitted longer-wavelength x-rays.

The attenuation rate was used to evaluate the difference between the emission intensities obtained using the two Ti filters. For the pinhole images, the attenuation rate was calculated by evaluating the integration counts for the images, while the theoretical WW attenuation rate was calculated using the WW spectra from the two reference x-ray spectra in Fig. 61. Although the GIS in this experiment was not calibrated, a comparison of the two attenuation rates was still valid in this case. The attenuation rate for the pinhole image is found to be 6 times larger than the WW attenuation rate in the reference x-ray spectra. This indicates that out-of-band x-rays contribute significantly to the emission in the pinhole images.

The FWHM values for the soft x-ray emission size are shown in Fig. 62, illustrating a WW emission area smaller than 40 μm, where highly-charged Au ions were generated.

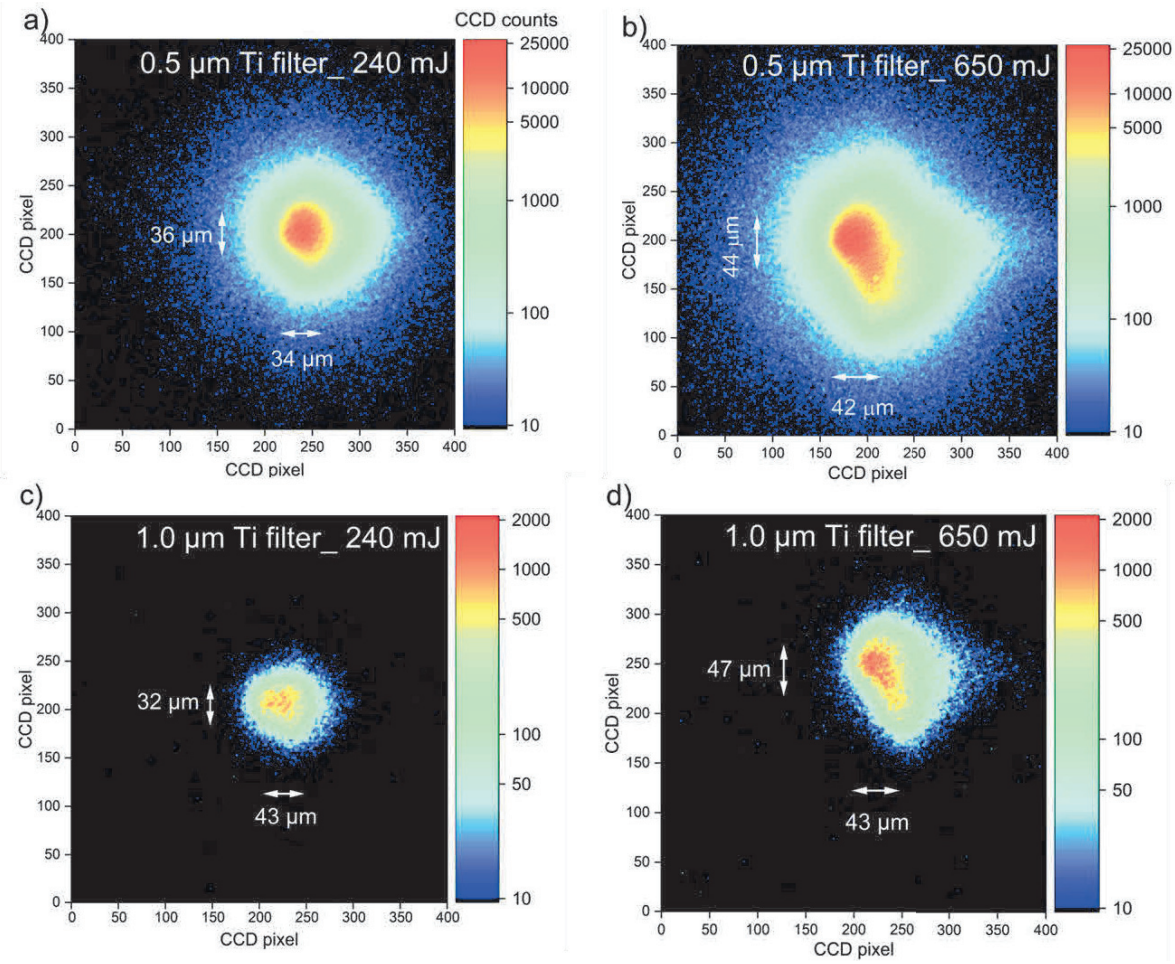

Fig. 62: Emissions from Au plasmas observed by pinhole camera for different laser energies and Ti filters. A 30-μm-thick Au foil was used as the target. (a) 0.5-μm-thick Ti filter, 240 mJ (1.43×10^{13} W/cm^2), (b) 0.5-μm-thick Ti filter, 650 mJ (3.86×10^{13} W/cm^2), (c) 1-μm-thick Ti filter, 240 mJ, and (d) 1-μm-thick Ti filter, 650 mJ. The solid arrows indicate the FWHM for the emission cross-section intensities in the horizontal and vertical directions.

The sensitivity of the CCD camera in the unit of photoelectrons per analog-to-digital (A/D) count was provided by Andor [89]. Unlike the quantum efficiency, the performance for each CCD was slightly different and this test data was accessible in the performance datasheet for each individual CCD. As shown in Fig. 63, the sensitivity Q_{CCD} was measured as 4.6 photoelectrons/count. The total photoelectrons generated at the sensor can be calculated as,

$$N_{eles} = (Counts_{signal} - Counts_{offset}) \times Q_{CCD} \qquad (3\text{-}2)$$

where ($Counts_{signal} - Counts_{offset}$) is the effective counts of the measured intensity. The relation between photon number N_{photon} at a given photon energy and the number of photoelectrons is,

$$N_{eles} = Q_{total}(\lambda) \cdot \frac{hc}{\lambda} \cdot N_{photon} \tag{3-3}$$

where $Q_{total}(\lambda)$ is calculated from Eq. (3-1). A rough calculation from the pinhole image for the soft x-ray brilliance is 10^{12} photons/(s · sr ·μm).

Summary of System Test Data

Readout Noise *♦1 and* **Base Mean Level**

A/D Rate (MHz All 16 bit)	Preamp setting	CCD Sensitivity ♦3 eles per A/D count	Single Pixel Noise electrons	Full Vert Bin Noise electrons	Base Level ♦2 (Counts)
5	x1	6.2	36.4	33.8	1804
5	x2	3.2	22.7	21.5	3474
5	x4	1.4	14.5	14.3	3531
3	x1	4.9	17.6	17.3	720
3	x2	2.5	12.4	12.7	1458
3	x4	1.2	10.8	9.5	1746
1	x1	4.6	10.1	10.5	570
1	x2	2.4	7.8	8.2	725
1	x4	1.2	6.9	7.5	1028
0.05	x1	4.7	4.1	5.1	562
0.05	x2	2.4	3.0	4.6	695
0.05	x4	1.2	2.7	4.1	972
Saturation Signal per pixel			120015	Electrons/pixel	

Fig. 63: Performance datasheet for the CCD used for the pinhole camera. The CCD sensitivity is shown in the third line in photoelectrons/count. The A/D rate was set 1 MHz during the experiment with a preamp setting of ×1.

3.1.4 Blur of pinhole image

Geometrical and diffraction effects should be considered when choosing the proper width of the pinhole. For geometrical regime, all emission points in the plasma are projected onto the CCD camera surface, which causes an overlapping of the images. The geometrical size of the pinhole in this case could not be neglected then, and the resolution d_{geo} is calculated by,

$$d_{geo} = d_{pinhole} \times (1 + M) \tag{3-4}$$

where M is the magnification of the system, d_{pinhole} is the width of the pinhole.

On the other hand, resolution in the diffraction regime is also considered as diffractions could produce an Airy-disc blur for the image, when the width of the pinhole is close to the emission wavelength. According to the Rayleigh criterion, one has

$$\theta = 1.22\frac{\lambda}{d_{pinhole}} \tag{3-5}$$

where θ is the angle between the two incident borders of the object, λ is the wavelength of the emission. Since θ is small when observing the plasma emission, then $(\tan\theta \approx \theta)$. The resolution in diffraction regime can be calculated as,

$$\begin{aligned} tan\frac{\theta}{2} &= \frac{\frac{d_{diff}}{2}}{u} \\ d_{diff} &= \theta \cdot u \\ d_{diff} &= 1.22 \cdot \frac{u \cdot \lambda}{d_{pinhole}} \end{aligned} \tag{3-6}$$

where u is the distance from the pinhole to the CCD sensor. By using Eqs. (3-4) and (3-6), the resolution of the pinhole camera in this work is calculated as shown in Fig. 64.

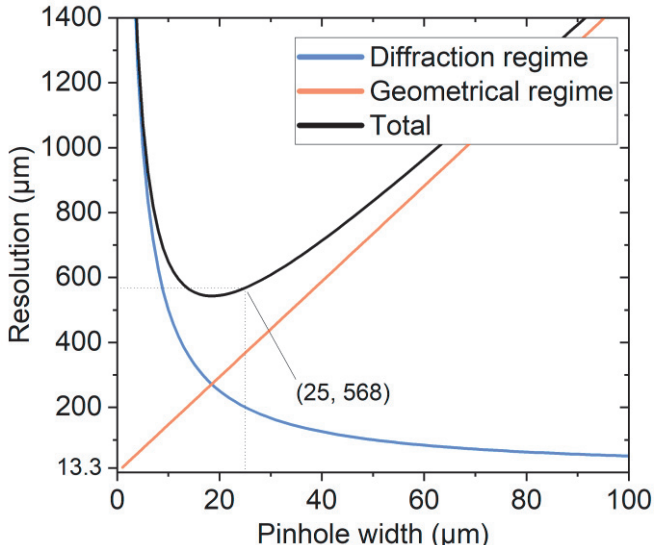

Fig. 64: Pinhole camera resolution as a function of pinhole width in the geometric limit and diffraction limit.

3.1.5 Soft x-ray yield measured by Si-diode

Similar measurement for soft x-ray yield was achieved using the Si-diode connected with a charge amplifier. X-ray emissions filtered by the 1-μm Ti was converted into single charge pulse Q_s by the Si-diode. The intensity of the pulse is proportional to the x-ray intensity. The output signal from the Si-diode causes a potential rising at the input-end of the charge amp., with a potential with reverse polarity generated at the output end immediately [90]. Since the open loop gain of the charge amp is large enough, the output voltage does not reach the threshold and can be given by,

$$V_{out} = -\int_0^t Q_s \frac{dt}{R \cdot C} \tag{3-7}$$

where R is the resistance and C is the capacitance. The discharge time constant for the charge amp. is given by,

$$\tau = R \cdot C \tag{3-8}$$

An example of the obtained signal is shown in Fig. 65. The blue line shows the $V_{\text{out}}(t)$ and the red line is the trigger signal as the laser pulse irradiation time. Although attempts for reducing the noise and electromagnetic interference were conducted, the discharge time was longer than expected value. A pre-pulse could be generated together with the main pulse, resulting in a pulse pileup effect. This displacement also limited the accuracy of the output voltage [91]. As a result, the data obtained from the Si-diode with charge amp is only used as a reference value for the results obtained from other detectors.

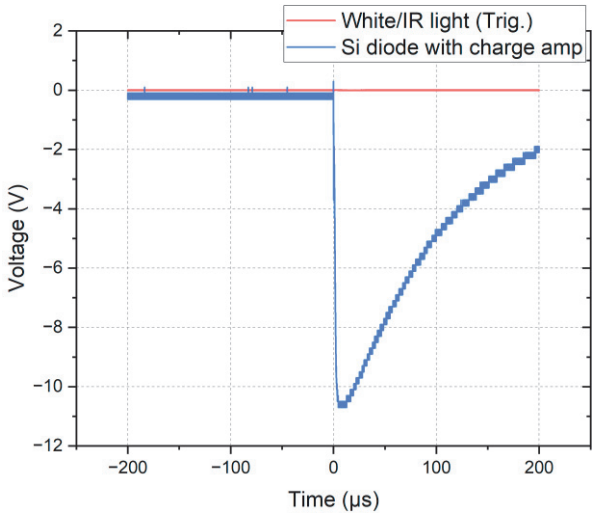

Fig. 65: X-ray yield signal obtained from the charge amplifier.

3.2 Spatial distribution of WW spectra

The laser-produced plasma expanded from the laser spot area in a 2π direction, along with emitting radiations. The spectra observed by the GIS in 3.1.2 refers to a small fraction of the radiation from the plasma collected by the toroidal mirror. As the entrance slit in the GIS was set vertically, spatial resolution in the vertical direction was not accessible. However, the longitudinal spatial resolution (laser incident direction) was tunable by changing the entrance slit to a narrower width. A scanning on the longitudinal spatial distribution can be very useful when combined with other plasma diagnostic tools, such as the Thomson scattering as described by Pan, Y., *et al*. [92], where the spectra information is compared with the electron temperature and density information. This combination also renders it a powerful tool for evaluating simulation results.

3.2.1 Principle of GIS

- **Principle of grating**

The grazing incidence spectrometer (GIS) used was composed of a flatfield grating, a toroidal mirror, an entrance slit and an X-CCD camera. The ultimate principle of the spectrometer involved using a spherical concave mirror to diffract incident light into spectra arranged vertically on the Rowland circle [93]. One of the most comprehensive developments for this was given by H. Beutler [94]. It is necessary to explain the basic principles of the spectrometer using a spherical reflection grating before introducing the schematic of the GIS. This will provide fundamentals for a deeper discussion on the results obtained from the GIS.

The flat-field grating diffracts incident light into spectra on a flat surface (such as the CCD camera sensor surface), however, the spherical concave grating can only image the spectra onto a curved line, known as the Rowland circle. The surface of the grating is full of grooves manufactured with a constant distance d. If an incident parallel light is diffracted by a grating as shown in Fig. 66, spectrum that can be reinforced by the diffractions from different grooves must satisfy the formula as,

$$d(\sin\alpha - \sin\beta) = m\lambda \tag{3-9}$$

where λ is the wavelength of the spectrum, m is the order of the spectrum (integer value only). When $m = 0$, all the wavelengths satisfy the equation (1-11), which leads to a chromatic diffraction light at the same position. The grooves on the grating surface are produced by mechanical ruling or holography, and the distance of grooves can be unequal spacing in some cases (like flat-field grating) to give an aberration correction.

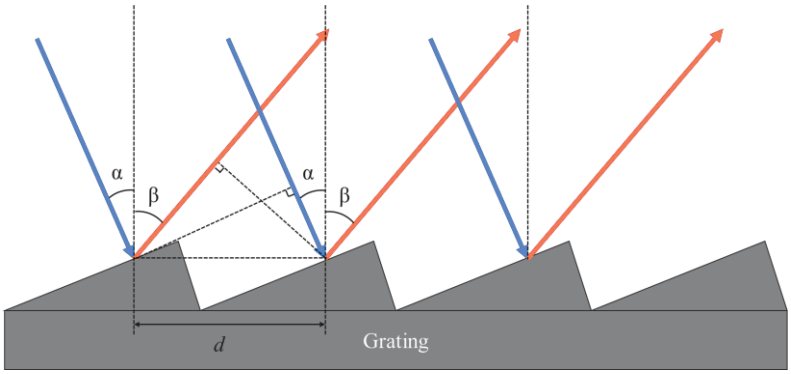

Fig. 66: Reinforced reflections diffracted by the grating. The color lines show the light path at different grooves, α and β are the incident angle and diffraction angle, respectively. The distance *d* refers to the groove distance.

The surface of the grating is usually curved, as all spectra with the same wavelength are required to be focused onto the same line. Therefore, it is necessary to give a deeper explanation on grating, especially the relation between the space resolution of the GIS and the entrance slit width as discussed in Chapter 4. Also, it gives theoretical basis for the GIS alignment procedures.

A Cartesian coordinate system is placed in the grating surface as shown in Fig. 67. The dash lines on the grating surface show the direction of the ruling of the grooves. The origin point O is the center of the grating ruling, with the *x*-axis being horizontal and normal to the grating surface, and the *z*-axis being vertical and parallel to the ruling. An incident beam AP originates from the entrance slit A (*x*, *y*, *z*) and reaches the grating surface at P (*u*, *v*, *w*), where it is diffracted to point B (x', y', z'). The angle α and β are the incidence angle and diffraction angle relative to the original point O, respectively. The *r* and r' are the distances from O to the projections of A and B on the *x*-O-*y* plane, respectively. Thus,

$$\begin{aligned} x &= r\cos\alpha \\ y &= r\sin\alpha \\ x' &= r'\cos\beta \\ y' &= r'\sin\beta \end{aligned} \tag{3-10}$$

The purpose to set this system is to solve the light path that satisfies with the ray APB. To simplify the coordinate of P in *y* direction (*v*), the *y*-axis is defined as only having discrete equidistant values as the distance *d* between the two adjacent grooves. Then, the light path from A, reinforced at B must satisfy with

$$F = < AP > + < BP > + N_i m\lambda \tag{3-11}$$

where *F* is the length of the light path of APB and N_i is the order of the groove obtained from

$$N_i = \frac{v}{d}\ (N_i = 0, \pm 1, \pm 2, \cdots) \tag{3-12}$$

Since the $N_i m$ is an integer value, all possible rays being reinforced at B are integer multiple of the wavelength longer than APB.

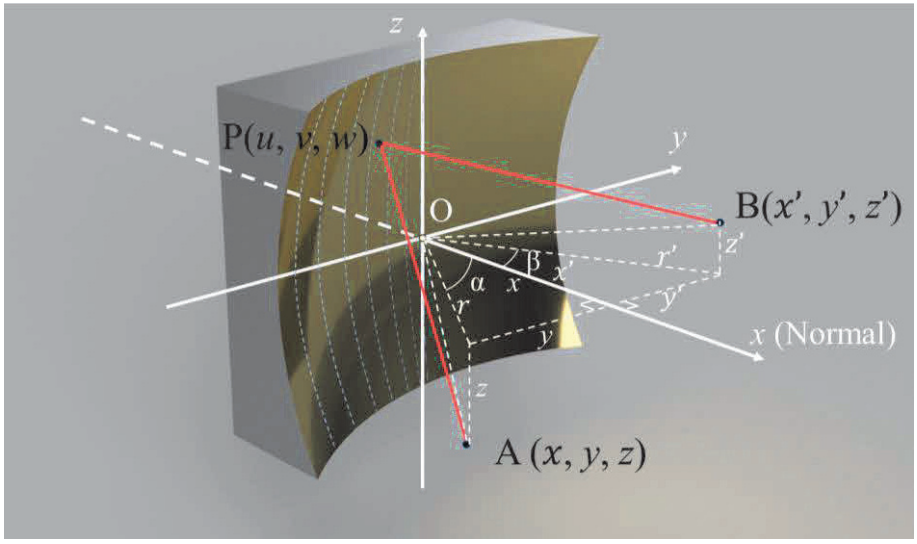

Fig. 67: The grating diffracts incident ray AP into PB within in a Cartesian coordinate system. O is the original point at the center of the grating ruling. $AO = r,\ OB = r'$, $\angle AOx = \alpha,\ \angle BOx = \beta$.

Next, the length of AP and BP are calculated as,

$$< AP >= (x-u)^2 + (y-v)^2 + (z-w)^2 \tag{3-13}$$

$$< BP >= (x'-u)^2 + (y'-v)^2 + (z'-w)^2 \tag{3-14}$$

Besides, since all possible P lie on a spherical surface with a radius of R, the u can be replaced by

$$u = R \pm [R^2 - (v^2 + w^2)]^{\frac{1}{2}} \tag{3-15}$$

Only the minus symbol is significant in this case due to the shape of the grating. To solve this formula, the power series expansion is brought into use as,

$$u = R - \sqrt{R^2}\sqrt{1 - \frac{(v^2 + w^2)}{R^2}}$$
$$= R - R(1 - \frac{(v^2 + w^2)}{2R} - \frac{(v^2 + w^2)^2}{8R^3} - \frac{(v^2 + w^2)^3}{16R^5} - \cdots) \quad (3\text{-}16)$$
$$= \frac{(v^2 + w^2)}{2R} + \frac{(v^2 + w^2)^2}{8R^3} + \frac{(v^2 + w^2)^3}{16R^5} + \frac{5(v^2 + w^2)^4}{128R^7} \cdots$$

To solve the ray path APB, Fermat's principle is employed. If the ray is reinforced at B, then all possible Ps for light passing through A and B satisfies with

$$\frac{dF(v)}{dv} = 0 \quad (3\text{-}17)$$

and

$$\frac{dF(w)}{dw} = 0 \quad (3\text{-}18)$$

This is because the coordinates of A and B are fixed, and the variables in Eq. (3-11) can be replaced using Eqs. (3-10), (3-15) and (3-16). The condition for this diffraction to occur is that both Eqs. (3-17) and (3-18) hold simultaneously.

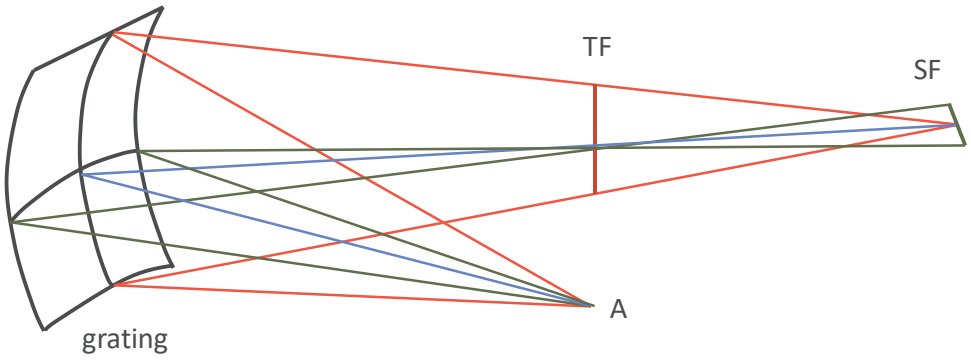

Fig. 68: Monochromatic light source A is focused into a tangential focus (TF), and then into a sagittal focus (SF) [95].

However, the characteristics of the spherical mirror determine that it focus the light from point A onto a vertical line (horizontal focus) firstly, and then into a horizontal line (vertical focus) (as shown in Fig. 68). A simplification of series is required to solve these formulae as written in [94] and [95]. The calculation process is skipped here, as it is not essential for the current argument. The solution for this at the horizontal focus is when,

$$\frac{\cos^2\alpha}{r} - \frac{\cos\alpha}{R} + \frac{\cos^2\beta}{r'} - \frac{\cos\beta}{R} = 0 \tag{3-19}$$

and the two solutions for Eq. (3-19) are

$$r = R\cos\alpha\,, \qquad r' = R\cos\beta \tag{3-20}$$

$$r = \infty, \qquad r' = \frac{R\cos^2\beta}{\cos\alpha + \cos\beta} \tag{3-21}$$

Equation (3-20) refers to the principle of the Rowland circle, which elucidates that all rays originating from A are diffracted into spectra arranged horizontally along the circle curve with a radius of R when the entrance slit A and the grating surface lie on the same Rowland circle. The r in Eq. (3-20) is a function of the incident angle α, expressing that the width of the entrance slit is significant. A wide width of the entrance slit can cause an overlapping of the spectra diffracted onto the Rowland circle. While the height of the slit is not significate in this case, because the ruling direction is parallel to the slit height. Schematic of the grating diffraction using a slit with height and width is shown in Fig. 69. Specific relations for the image (monochromatic) variation on the slit size are given by

$$\frac{Width_{slit}}{Width_{image}} = \frac{r\cos\beta}{r'\cos\alpha} \tag{3-22}$$

$$\frac{Height_{slit}}{Height_{image}} = \frac{r}{r'} \tag{3-23}$$

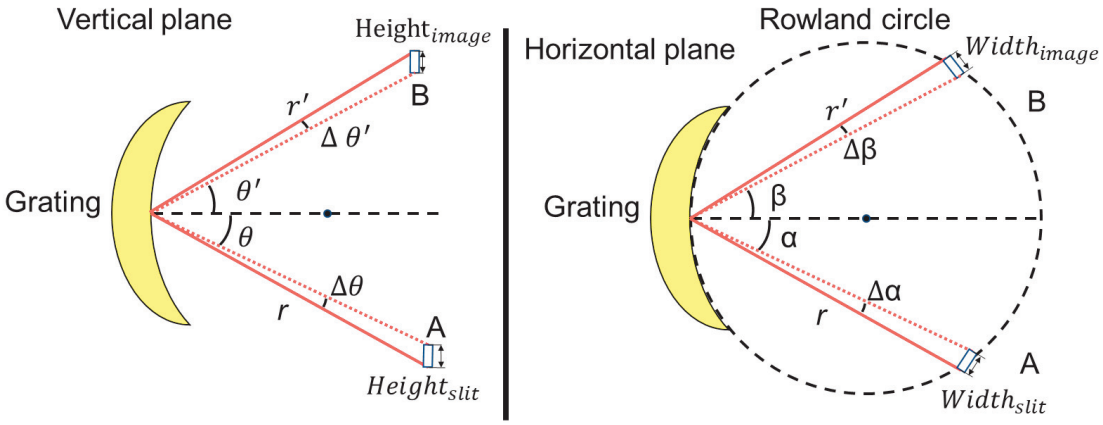

Fig. 69: Effect of entrance slit width and height on diffracted light. A and B are the points on the Rowland circle.

The difference between the image magnifications in the two directions is due to the focus

mechanism of grating in these two directions.

Another important thing is when calculated Eqs. (3-17) and (3-18), only finite terms are calculated. The neglect of other terms brings aberrations for the image on the Rowland circle, depending on the term, different aberrations such as defocus and coma can be generated.

For the vertical focus (second focus), solutions for Eqs. (3-17) and (3-18) are given by

$$\frac{1}{r}-\frac{cos\,\alpha}{R}+\frac{1}{r'}-\frac{cos\,\beta}{R}=0 \tag{3-24}$$

Two solutions for this equation are as follows:

$$r=\frac{R}{cos\,\alpha},\qquad r'=\frac{R}{cos\,\beta} \tag{3-25}$$

$$r=\infty,\qquad r'=\frac{R}{cos\,\alpha+cos\,\beta} \tag{3-26}$$

Equation (2-2) shows that both A and B lie on the same line tangent to the Rowland circle of the grating with a distance of *R*. Noting that these solutions are completely different from Eqs. (3-20) and (3-21). If inputting $r = R\cos\alpha$ as the entrance slit on the Rowland circle into the vertical focus term in Eq. (3-24). The locus of B in this case is

$$r_v{}'=\frac{R}{cos\,\beta-sin\,\alpha\,tan\,\alpha} \tag{3-27}$$

where $r_v{}'$ refers to the vertical focus curve on the Rowland circle. However, since this light follows the rule of Rowland circle, both slit and image point locate on the same circle with the same radius *R*. This illustrates the image is suffering astigmatism from the vertical focusing.

One special situation is when point P coincides with the original point O. Equation (3-9) can then be derived from Eqs. (3-17) and (3-18).

- **Grating with toroidal mirror**

To reduce aberrations in focusing and enhance the throughput of the system, the addition of a toroidal mirror before the entrance slit proves to be a practical method. Curvatures of the toroidal mirror in vertical and horizontal directions usually have different angel for an aberration-correction. Fig. 70 shows the condition when a toroidal mirror M is added before the entrance slit s_2. s_h and s_v are distances from M to the horizontal focus and vertical focus. A vertical line is focused by the toroidal mirror at S_2, which is consequently diffracted by the grating onto the Rowland circle. The radii for toroidal mirror and its relation to the grating are given by

Horizontal $$\frac{1}{s}+\frac{1}{s_h}=\frac{2}{R_h\,cos\,\phi} \tag{3-28}$$

Vertical $$\frac{1}{s}+\frac{1}{s_v}=\frac{2\cos\phi}{R_v} \quad (3\text{-}29)$$

where R_v and R_h represent the radii of the Rowland circle at vertical and horizontal focusing, respectively.

In the previous section, the image point B is suffered from astigmatism on vertical focusing as Eq. (3-27). However, the toroidal mirror in Fig. 70 can help grating to produce a stigmatic image, when

$$s_v = s_h + < S_2G > + < GB > \quad (3\text{-}30)$$

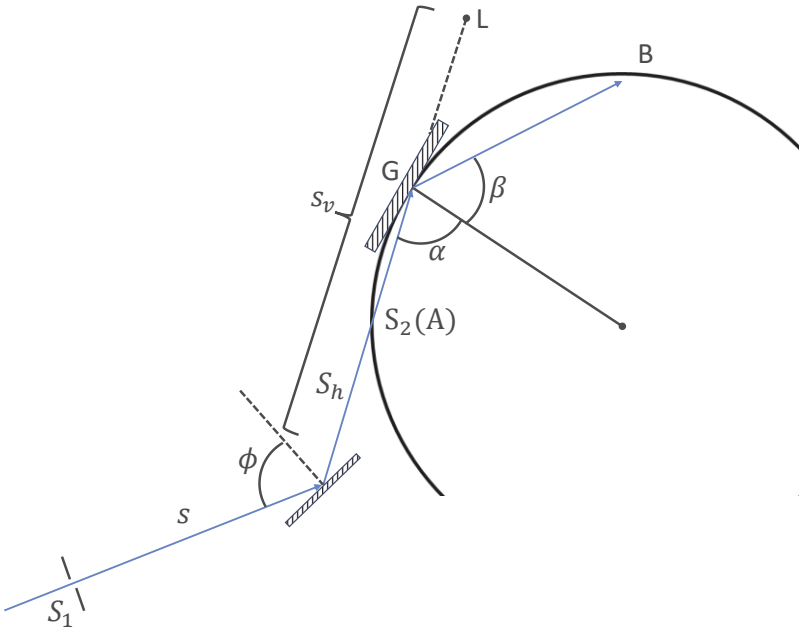

Fig. 70: Schematic of the spectrometer using a grating with a toroidal mirror in front of the entrance slit [94].

- **Flat-field concave grating with toroidal mirror**

Although the Rowland circle brings great convenience for spectra analyzing, its curvature locus of the horizontal focus makes it difficult to use most of the detectors with flat plane sensors. Aberration-corrected flat-field gratings with a varied groove distance are consequently developed [96], as shown in Fig. 71. Focus of the image point B is given as,

$$r' = \frac{L}{\sin\beta} \quad (3\text{-}31)$$

where L is the distance between grating center O and CCD sensor surface. R_h, R_v, s_h, and s_v represent the same terms as in Eqs. (3-28) and (3-29).

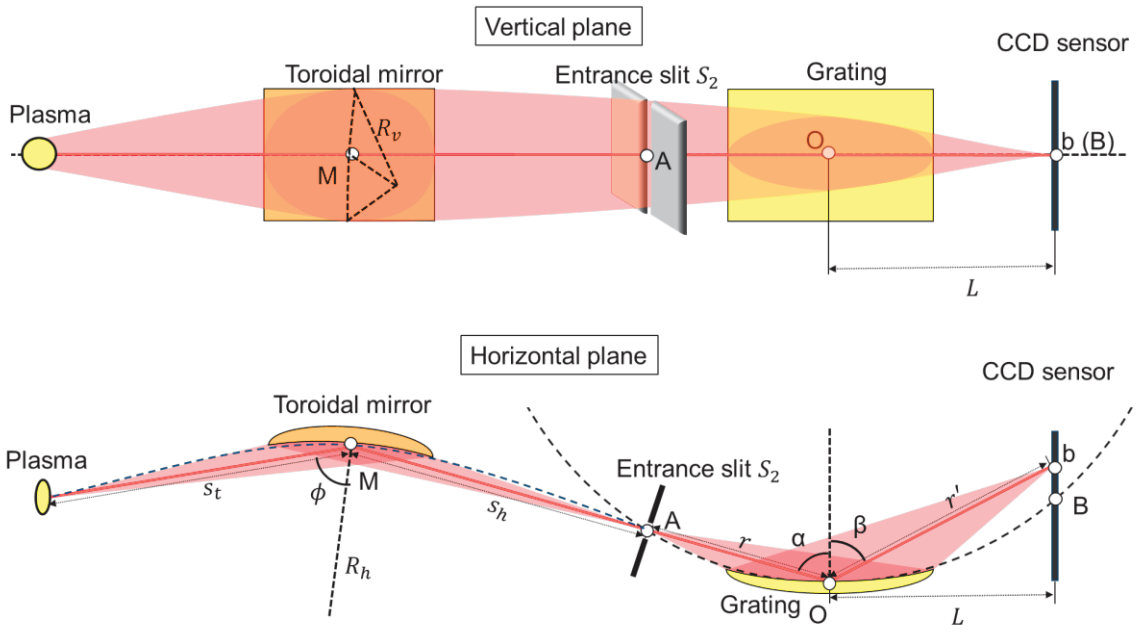

Fig. 71: Schematic of a flat-field grating with a toroidal mirror. s_t is the distance from light source (plasma) to the center of the toroidal mirror. s_h is the distance of MA, where A is coincided with the entrance slit S_2, and is situated on the vertical focus point of both the toroidal mirror and the grating. The dash lines show the Rowland circle locus for the two components.

To give a stigmatic image on the CCD sensor plane, horizontal focus and vertical focus of the toroidal mirror must locate on the Entrance slit S_2 (A) and CCD sensor surface, respectively. In the meantime, A and B should also lie on the horizontal focus of the flat-field grating. These relations can be written as,

$$s_v = s_h + r + |r'| \tag{3-32}$$

The absolute value sign is added for r', because the relation between r' and r in the case of grazing incident has,

$$\frac{1}{r} + \frac{1}{r'} = \frac{1}{\frac{R}{\cos\alpha + \cos\beta}} \tag{3-33}$$

where R is the radius of the grating curvature, $R/(\cos\alpha + \cos\beta)$ is the focus distance f of the system. Utilizing Eqs. (2-1) and (3-33), one can obtain,

$$\frac{1}{r} = \frac{\cos\alpha + \cos\beta}{R} - \frac{\sin\beta}{L} \tag{3-34}$$

where *r* is a negative value in the case of grazing incident.

3.2.2 Spatial resolution of the GIS

The spectral distribution in the 1D dimension is typically scanned using an optical structure known as push broom [97][98]. An example of a push broom spectrometer produced by [99] was installed in a satellite to analysis spectra from moons of Mars. The simplified schematic is shown in Fig. 72. The spectrometer scans the ground surface along the satellite motion direction, focusing the image using a telescope through an entrance slit. Consequently, the image is diffracted by the dispersing element and re-imaged into a 2D image with spectra information in one spatial dimension. The width of the slit determines the resolution of each strip on the final image.

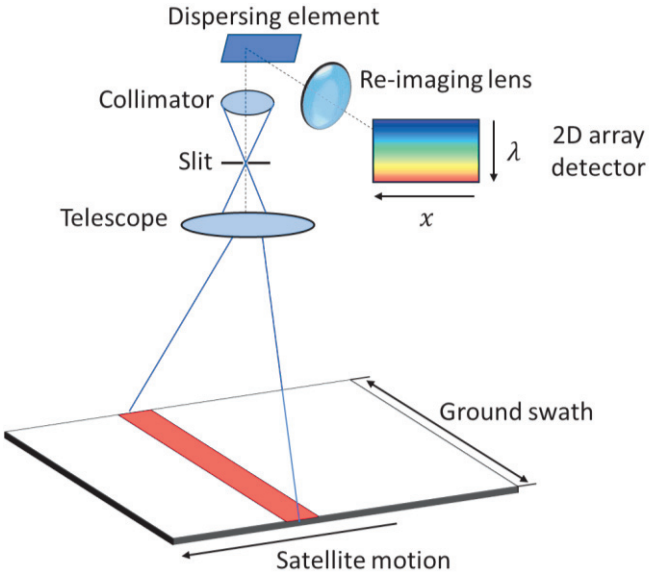

Fig. 72: Schematic of an image spectrometer using push broom acquisition principle [99].

In the case of using a toroidal mirror as the objective focusing, x-ray emissions at the horizontal focus region (shown as yellow region in Fig. 73) are focused onto a vertical line at the entrance slit of the GIS. The spot in this case suffers from the astigmatism as discussed in 2.2.3. By using the following focusing formula of toroidal mirror at the horizontal focus,

$$\frac{1}{S_h} + \frac{1}{S_t} = \frac{2}{R_h \cos\phi} \tag{3-35}$$

the relation between the two foci S_h,S_t and the horizontal curvature R_h of the toroidal mirror is described. The magnification rate between the objective width and the imaging width

defined by the slit width is given by,

$$\chi = \frac{w_{slit}}{w_{objective}} = \frac{S_h \cdot \Delta\phi}{S_t \cdot \Delta\phi'} \tag{3-36}$$

when the light passes through the center of the toroidal mirror. $w_{objective}$ and w_{slit} are the width of objective and the slit, χ is the magnification, S_t and S_h are the distances from objective to the toroidal mirror center and from center to the slit, $\Delta\phi$ and $\Delta\phi'$ represent the changes in angles of the incidence and reflection between the two edges of the objective, respectively (see Fig. 71). Because ϕ and ϕ' are the same in the case of mirror reflection, and the objective and the slit are located on the Rowland circle of the toroidal mirror, one has

$$\Delta\phi = \Delta\phi' \tag{3-37}$$

$$S_h = S_t = R_h \cos\phi \tag{3-38}$$

Therefore, the magnification is nearly 1. Furthermore, it is possible to adjust the spatial resolution of the GIS by changing the w_{slit}.

The scanning axis is coincided with the incident laser beam, as illustrated in Fig. 73. x_{GIS} refers to the distance from the Au target surface to the strip observed by the GIS. As the GIS is not movable, target and lens are instead moved, maintaining a fixed focal distance to ensure consistent irradiation power.

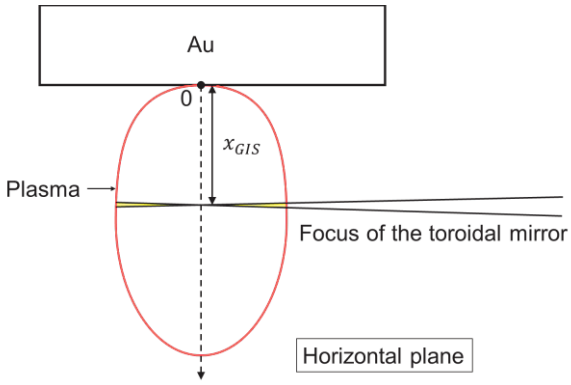

Fig. 73: Schematic of the push broom spectrometer using a toroidal mirror.

The flat-field grating provides convenience for spectral measurements, but aberrations from the two foci of the toroidal mirror and the grating still persist in practical cases. The focused spot shape at the foci of the toroidal mirror could be observed during the GIS alignment as illustrated in Fig. 74. The focus is similar to the proportion symbol as "∝". This is considered to be the result of the modification of the GIS. To reduce the aberrations at the horizontal focal point as discussed in above, a modification for balancing the aberrations from the two foci is possible as explained in [95] (see Fig. 75). Horizontal focusing (thick line) and vertical focusing (thin line) at different conditions are listed. The focus patterns in (b) and (c) are similar to the one that observed during the practical experiments, which is reasonable for

a flat-field grating.

Fig. 74: Focus spot of the GIS alignment laser on the Au target surface. The bifurcation is formed by the aberrations from the focusing in two dimensions.

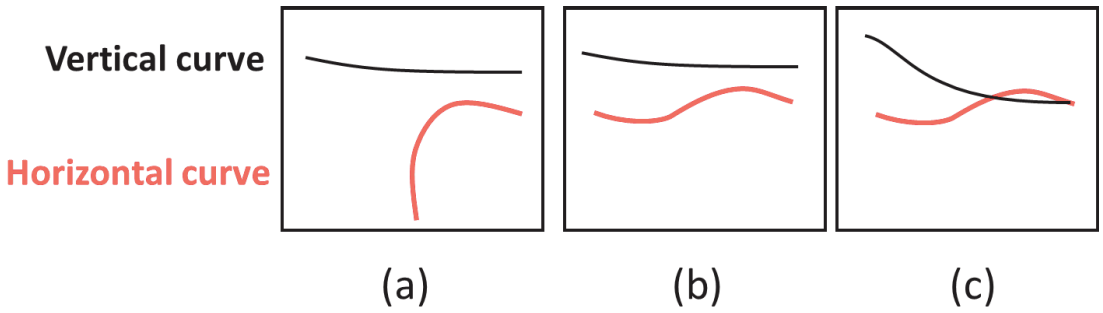

Fig. 75: Focal curves at different conditions: (a) non-modification for the grating (b) modification applied for horizontal focus curve, suitable for the flat-field imaging. (c) modification applied for the vertical focus curve, a stigmatic point is formed at the cross of the two lines [95].

The shape formation of the focal spot is important for evaluating the observation position x_{GIS} during the experiment, because the location of the GIS focus can only be evaluated from the CCD image. Summarized CCD images of GIS at different typical x_{GIS} are illustrated in Fig. 76. Three columns show: (a) Schematic of the different GIS observation. (b) Obtained CCD image at the corresponding position. (c) Diagram of the light focused by the toroidal mirror at the entrance slit. The focused image in (b) is simplified as it does not consider the variation in the focus shape for the light source at different positions.

However, a rough comparison is possible because when the focusing is behind the Au surface, the bifurcation on the slit is observed as two diffracted spectra on the CCD image. On the other hand, spectra are still possible to be observed when $x_{GIS} > L_{plasma}$ (L_{plasma} is the longitudinal length of the plasma) as the shown in Fig. 76(a). In conclusion, the aberrations of the GIS focusing may limit the spatial resolution during the push broom measurement.

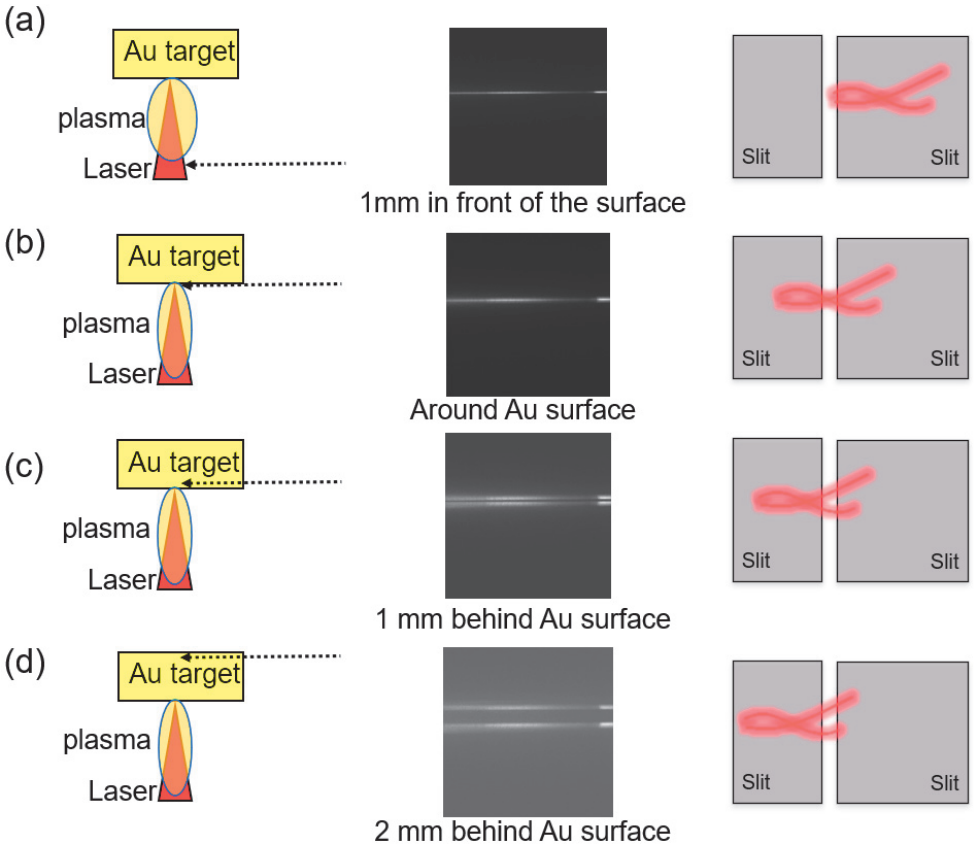

Fig. 76: GIS images observed at different observation positions (x_{GIS}). The dashed arrow line indicates the focus of the GIS, and the plasma region is depicted within the yellow ellipse. The GIS focus was positioned at (a) 1 mm in front of the surface, (b) around Au surface (c), 1 mm behind Au surface, and (d) 2 mm behind Au surface.

3.2.3 Spectra scanning

To obtain a spatially spectral emission distribution, a 2D spectra scanning along the laser incident direction was conducted by utilizing the GIS with a 50-μm slit width (shown in Fig. 77). A 30-μm Au foil was irradiated by a pulse energy of 3.86×10^{13} W/cm^2. A peak CCD count at the observation position of 200 μm has been observed where both n=4-4 and n=4-5 transitions emitted the intense UTA. Noting that the difference in emission size between the pinhole camera image and the GIS result was caused by the aberrations from the GIS focusing, and the difference in the observed wavelength ranges.

The surface of the target referred to as the observation position x_{GIS}= 0 μm, which was confirmed by evaluating the vertical cross-section width of the spectra in the GIS image, as shown in Fig. 78. When the vertical width of the spectra exceeded 10 μm, the observed spectra in the GIS image represented the overlapping of two spectra lines from the bifurcation. While the width became smaller when the observation was deviated.

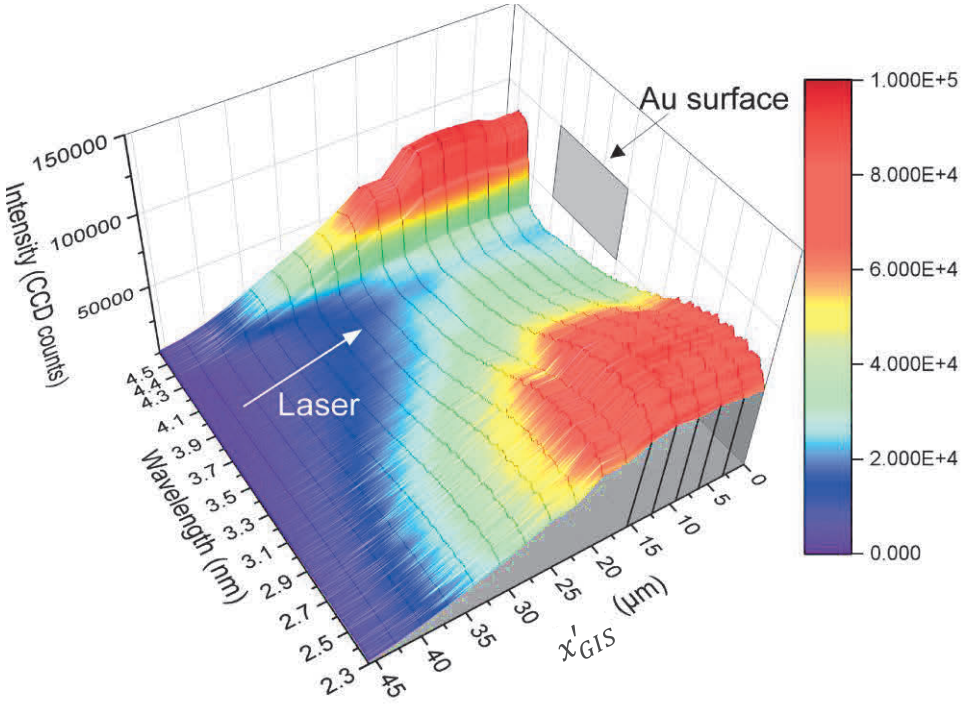

Fig. 77: 2-D spectral emission behavior irradiated with a laser intensity of 3.86×10^{13} W/cm^2. $x'_{GIS} = 0$ is the position where GIS observed on the Au surface. The x'_{GIS} is calibrated from the x_{GIS} using the FWHM of the soft x-ray emission region in the pinhole images.

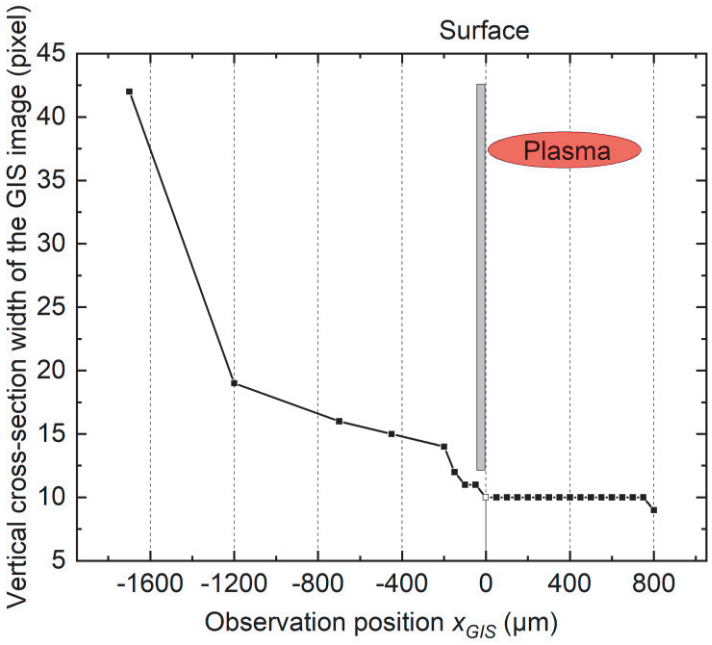

Fig. 78: The variation in the vertical width (FWHM) of the spectra in the GIS images.

3.3 Optimal Au target thickness for WW x-ray source

In this section, WW emissions from Au laser plasmas generated by targets with different thicknesses were evaluated. Dependence of x-ray emission on Au thickness at fixed laser energy was illustrated in 3.3.1. Since two types of the Au target were used in the experiment, an evaluation of the Au surface manufactured by the two methods was conducted in 3.3.2, which will be later compared to the simulation results in 3.4.3.

3.3.1 Dependence of x-ray emission on Au thickness

The optimal Au thickness was investigated by evaluating x-ray emissions from plasmas produced from various Au targets for two different laser energies (650 mJ and 240 mJ). All the plasmas were generated by tightly focused laser pulses with intensities of 3.86×10^{13} W/cm^2 and 1.43×10^{13} W/cm^2, respectively. The spot size was 15 μm FWHM under the tight focus condition.

Fig. 79 shows the Au spectra produced by deposition and foil targets for a laser energy of 650 mJ. The foil targets generate nearly constant spectral intensities. However, a prominent enhancement is seen between the foil targets and 1.8-μm-thick deposition target. Line spectra from O and Si ions are also observed from the deposition targets. The spectral intensity gradually drops with decreasing deposition target thickness until a constant UTA can no longer be observed.

The initial plasma is generated by laser ablation, where the laser has a characteristic heat conduction length. Depending on the Au layer thickness, this heat conduction length can lead to different thermal conduction processes in the initial period of ablation. For foil targets with thicknesses above 10 μm, the heat conduction length is independent upon the Au thickness, so 3D hemispherical thermal transfer from the laser spot in the Au layer occurs (as shown in Fig. 80(a)). However, when the Au thickness is thinner than the laser spot radius, the thermal transfer direction changes from hemispherical to horizontal because of the thin Au layer (Fig. 80(b)). The large difference between the Au and glass thermal conductivity and heat capacity also contributes to this 2D transfer mode [100–102]. Therefore, it is considered that the enhancement of the 1.8-μm-thick Au spectral intensity is caused by the different thermal transfer mode for the thick Au target, where laser interaction with the deposited Au atoms is more effective. The angle distribution of the emissions should also be considered due to the different thermal transfer mode, because the emission intensity is not uniform as studied before in [103]. The different microstructures of the two kinds of targets are also attributed to this effect. The results for the target surface observed by a microstructure scanning apparatus will be described later.

The reason for the spectral intensity drop for much thinner deposition targets can be explained by there being insufficient Au atoms in the irradiated region to emit intense WW x-rays. As the Au layer is too thin, a considerable portion of the laser pulse penetrates to the substrate glass plate (SiO_2) and generates glass plasma. Thus, O and Si line spectra are observed for thinner deposition targets.

The x-ray yields were evaluated by three approaches: integration of the CCD counts measured from the GIS spectra in the WW region, total CCD counts for the pinhole images (1.0-μm-thick Ti filter), and the integrated Si-photodiode signal from the charge amplifier (1.0-

μm-thick Ti filter,) as shown in Fig. 81. Each data point in the plot is averaged from three laser shots. The vertical and horizontal error bars represent fluctuations of intensity and deposited Au thickness, respectively. All the detectors show nearly constant values from 300 μm to 10 μm. The x-ray yields measured by the Si diode and pinhole camera do not show the same rise as the GIS data at 1.8 μm and 10 μm. This is because out-of-band X-rays, especially at wavelengths > 4.3 nm, significantly contributes to the x-ray yield for the former two detectors (see 3.1.3), while the GIS data only include the WW emission. The intensity rise observed by the GIS is caused by the different thermal conduction modes, as explained in the above. A clear drop between 1.3 μm and 1.0 μm for all three lines indicates that the thickness of the Au layer is no longer sufficient, though 70% of the x-ray yield could still be observed for targets with thicknesses of less than 1.3 μm.

For a laser energy of 240 mJ, thinner Au targets can be used to maximize the WW emission without ablating the SiO_2 layer than that in the 650-mJ case, as shown in Fig. 82. In Fig. 83, the WW yield calculated from the GIS data for Au thicknesses ranging from 0.1 μm to 1.8 μm is shown by the black square symbols and line. The WW yield rises as the Au thickness increases and then saturates at around 0.6 μm. The x-ray yields obtained from the pinhole camera and Si diode show similar trends to that for the WW yield, indicating that the Au thickness limit is around 0.6 μm for a laser energy of 240 mJ.

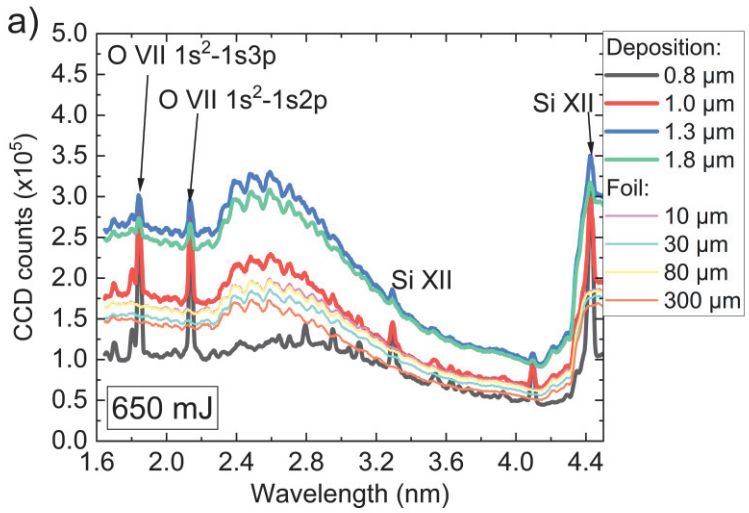

Fig. 79: Au spectra for targets with various thicknesses produced by 650 mJ laser pulses (3.86×10^{13} W/cm^2). O and Si line spectra originating from the laser–glass interaction are observed for the deposition targets (0.8–1.8 μm). The foil and deposition targets are shown as lines with different widths.

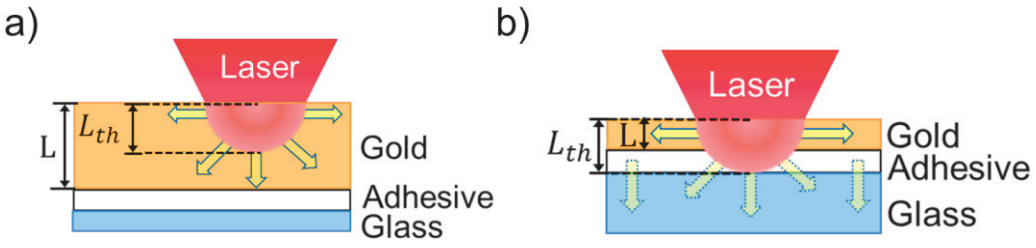

Fig. 80: Laser thermal transfer modes in different conditions. (a) The Au thickness L was longer than the laser heat conduction depth L_{th}. (b) The Au thickness was shorter than the heat conduction depth L_{th}.

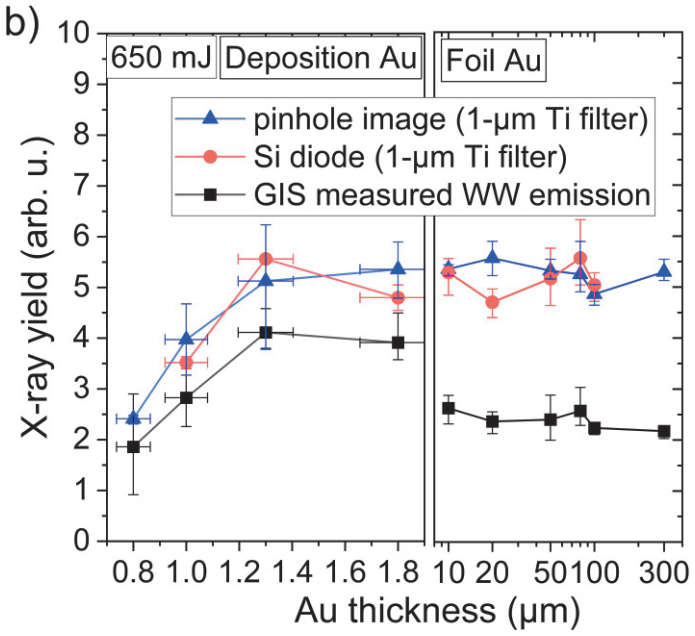

Fig. 81: X-ray yield as function of Au target thickness for 650 mJ (3.86×10^{13} W/cm^2) laser energy, calculated by integrated pinhole image counts (blue), integrated Si diode signal (red) and WW region of integrated GIS data (black). Note that the units for x-ray yield for the three results are largely irrelevant.

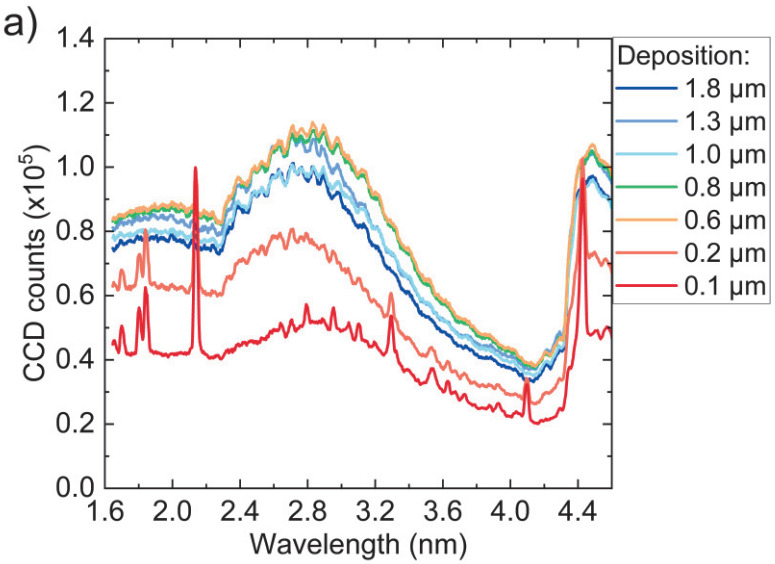

Fig. 82: Au spectra for targets with different thicknesses produced by 240-mJ (1.43×10^{13} W/cm^2) laser pulses.

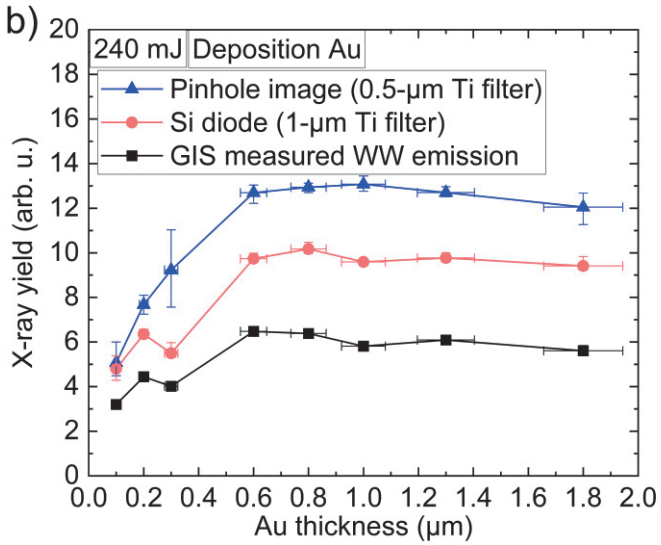

Fig. 83: X-ray yield as function of Au deposition target thickness for 240-mJ (1.43×10^{13} W/cm^2) laser energy.

3.3.2 Error analysis of different Au targets

An analysis on the Au surface microstructure was performed to elucidate the mechanism on the x-ray emission behavior from the different Au plasmas. The surface microstructure of the commercial foil targets was observed by an optical microscope, as shown in Fig. 84(a). Due to manufacturing limitations for these targets, the surface conditions show clear

differences, which give different laser–target interactions and results for the fluctuations of the x-ray yield. Craters on the deposition targets appear in the upper panel of Fig. 84(b), observed using the SEM. A dimple in the center of the crater is formed by the laser–target interaction, while the length marked in yellow indicates the melt zone for Au and glass, the area most affected by thermal heat conduction and subsequent ablation. The dimple on the glass plate for the 1.3-μm-thick target illustrates that the minimum Au thickness (1.3 μm) for sufficient WW x-ray emission is smaller than the characteristic depth of the dimple formed by laser ablation. Consequently, both normal level WW x-rays and Si/O line spectra are observed from the plasma at 1.3-μm target thickness. The surfaces were also analyzed to identify the elemental components by energy dispersive spectroscopy (EDS). The lower panels in Fig. 84(b) show that the deposited Au area is completely melted and ablated, and only Si and O elements are detected in the crater after 650-mJ (3.86×10^{13} W/cm^2) laser irradiation.

The foil targets were also examined using AFM to provide a detailed observation of the surface conditions (Fig. 85). By scanning the Au surface with the cantilever, a 3D image, including thickness variations, is generated. Different roughness conditions with micrometer-scale height errors are observed on the foil targets, which are in a good agreement with the results in Fig. 84(a).

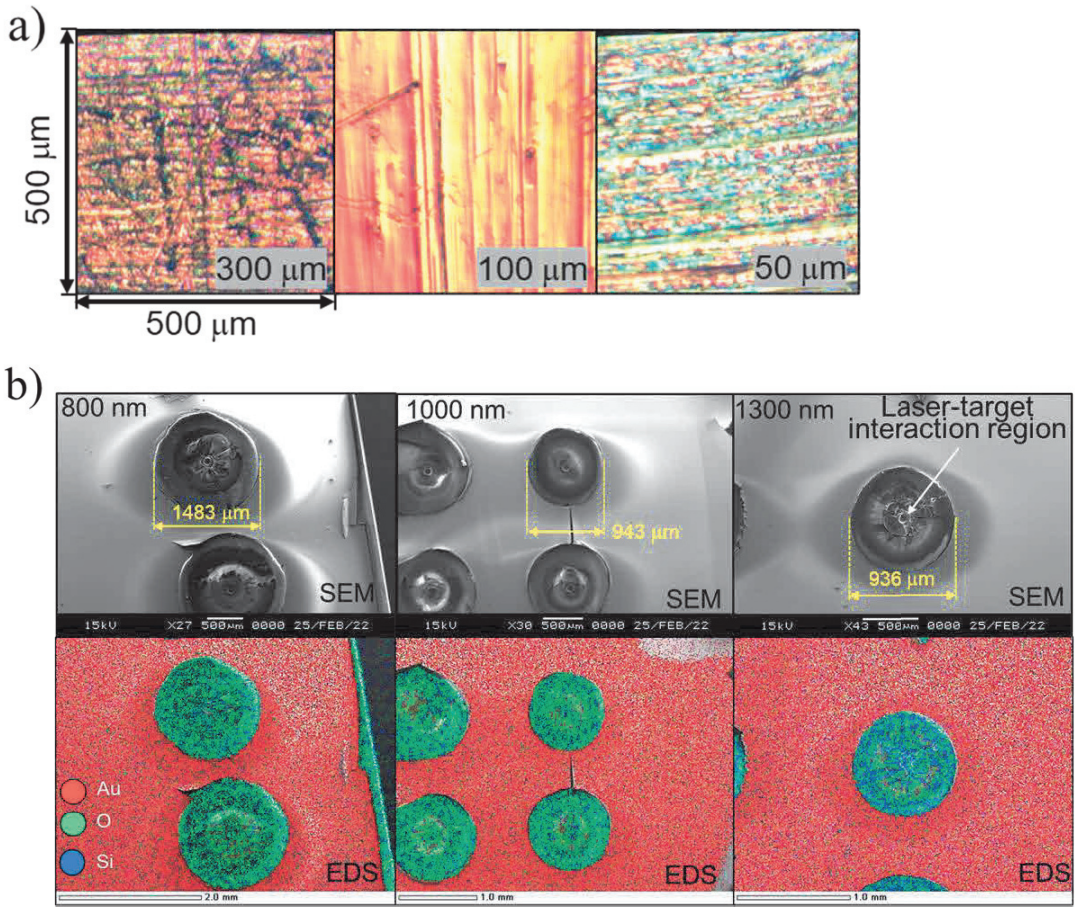

Fig. 84: (a) Au foil surfaces observed by optical microscope. (b) Upper panel: SEM images of Au deposition target surfaces after irradiation with 650-mJ (3.86×10^{13} W/cm^2) laser pulses. Lower panel: EDS element analysis of same area as upper panel.

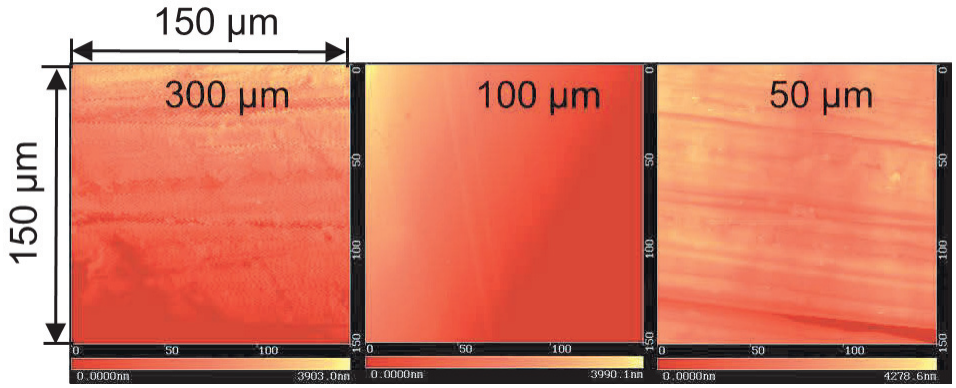

Fig. 85: Foil targets surface scanned by AFM.

Although good surface conditions were identified for the deposition targets, the

thickness error during the deposition process should also be considered. The thermal evaporation system can be simplified as Fig. 86. The Au particles were set at the center *S* of the tungsten holder. While the glass substrate center O was above the Au at a distance of *h*. X is a point on the glass substrate with a distance *x* to the center O. The mass of evaporated Au passing through a solid angle $\mathrm{d}\omega$ is given by,

$$dm = \frac{m}{4\pi} \cdot d\omega \tag{3-39}$$

where *m* is the evaporated mass of Au. For a deposited area $\mathrm{d}S_t$ on the glass surface, one has

$$cos\,\theta\, dS_t = dS = r^2 d\omega \tag{3-40}$$

where θ is the angle between the glass surface and the evaporation direction of the $\mathrm{d}\omega$, $\mathrm{d}S$ is the area of the solid angle at a distance *r*. The mass of the deposited Au at $\mathrm{d}S_t$ is,

$$dm = \rho \cdot t \cdot dS_t \tag{3-41}$$

where ρ is the density of the deposition layer and *t* is the thickness growth per unit time.

The deposition time can then be derived by combining Eqs. (3-39), (3-40) and (3-41).

$$t = \frac{m}{4\pi\rho} \cdot \frac{cos\,\theta}{r^2} \tag{3-42}$$

Since *t* is proportional to the deposited Au thickness, the deviation is,

$$\frac{t(x)}{t(0)} = \frac{1}{(1 + (\frac{x}{h})^2)^{\frac{3}{2}}} \tag{3-43}$$

where $t(x)$ is the growth speed of the Au layer at a distance of *x* to the glass center O. The calculated deviation is shown in Fig. 87, and the theoretical deposition rate for the deposition targets in this work is shown in Fig. 88.

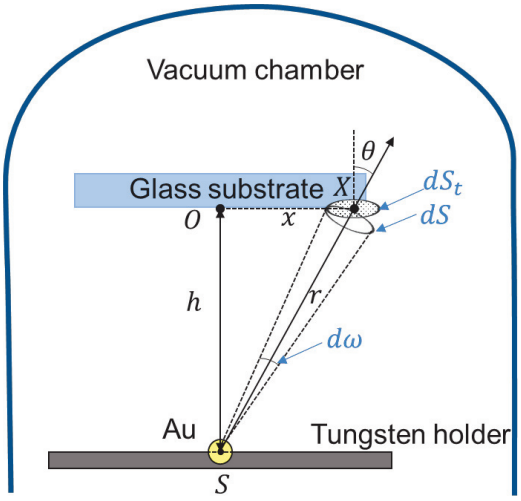

Fig. 86: Schematic of the thermal deposition device. The Au source is placed at point S on the tungsten holder was treated as a point source. The vapor passes the surface with a distance r to the S in a solid angle $d\omega$ in a unit time is expressed as dS.

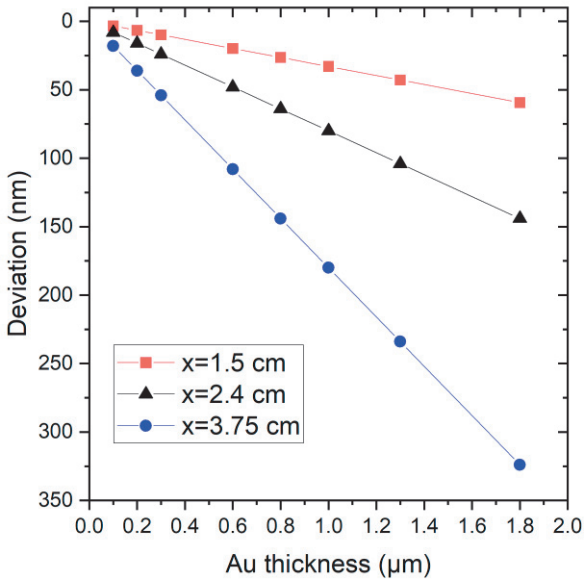

Fig. 87: Deviation of the depostion thickness at different distance from the substrate center.

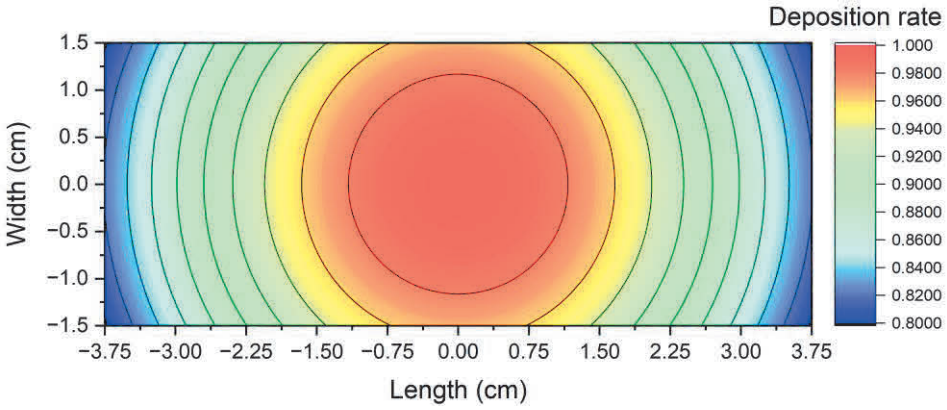

Fig. 88: Calculated relative deposition rate on the glass substrate.

A typical deposition target with a thickness of 1.8 μm is shown in Fig. 89. During the experiment, only the region within x = 2.4 cm was used for data collection, therefore, a deviation of 0.08 is considered as the target thickness error.

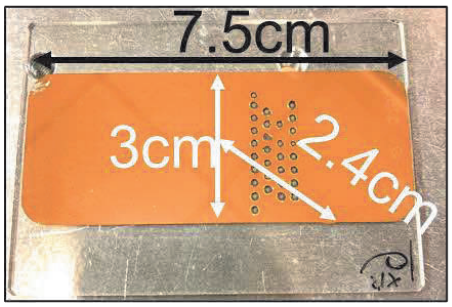

Fig. 89: The size of a typical depostion target, and the region used for data collection.

3.3.3 Plasma modeling

Numerical calculations for verifying the results obtained from the experiments are usually necessary. A deeper understanding of the potential mechanisms during the plasma expansion can be investigated by combining the experimental and theoretical results. Consequently, a theoretical description of the LPP is needed.

Many formulae can be used to describe a plasma in thermal equilibrium under ideal conditions. However, in practical cases, due to radiation energy transport and radiation trapping, complex radiation and absorption processes can occur during plasma generation, leading to unpredictable emission behavior and population distribution. To address this challenge, various plasma models have been developed to approximate the states of the plasma. In this part, basic equations for describing a practical plasma condition are discussed, because these equations are essential for the simulation tool, Star-2D code [104], used in this work to evaluate the optimal Au plasma conditions for WW emission.

- **Blackbody radiation**

The black body is an ideal object where the energy from the incident light is completely absorbed and converted into the radiation. The blackbody is in the thermal equilibrium and the radiation emitted from it has continuum spectra with respect to the frequency ν, the radiation energy density $u(\nu)d\upsilon$ between ν to $d\nu$ can be described by,

$$u(\nu)d\nu = \frac{8\pi h\upsilon^3}{{c_0}^3}\frac{1}{exp\left(\frac{h\nu}{kT}\right)-1}d\nu \tag{3-44}$$

Where h is the Planks constant, k is the Boltzmann constant. By using $\omega = 2\pi\nu$ and $\hbar = h/(2\pi)$, Eq. (3-44) can be written as

$$u(\omega)d\omega = \frac{\hbar\omega^3}{\pi{c_0}^3}\frac{1}{exp\left(\frac{\hbar\omega}{kT}\right)-1}d\omega \tag{3-45}$$

which expressed in terms of frequency. Also, Equation (3-44) in terms of wavelength λ with substitute the values,

$$u(\lambda)d\lambda = \frac{8\pi hc_0}{\lambda^5}\frac{1}{exp\left(\frac{hc_0}{\lambda kT}\right)-1}d\lambda \tag{3-46}$$

These formulae are known as the Plank's equation.

The blackbody radiation is useful when using the Wien's displacement law to calculate the temperature for a desired emission with a peak wavelength λ_{peak} from the black body,

$$\lambda_{peak} = \frac{2.898\times10^6 nm\cdot K}{T} \tag{3-47}$$

where K is the temperature in unit of kelvin. For example, a radiation with a peak wavelength of 3 nm can be generated when $T = 83$ eV. However, this value can be quite different from a LPP in the real case, due to the self-absorption and many other mechanisms during the plasma expansion.

- **Boltzmann distribution**

In a two-quantum-level system, the number density N of atoms in the level L_1 and L_2 are described as N_1 and N_2. The relation between N_1 and N_2 in a thermal equilibrium condition then follows the Boltzmann distribution as

$$\frac{N_2}{N_1} = exp[-\frac{(E_2 - E_1)}{kT}] \tag{3-48}$$

where k is the Boltzmann constant, E_1 and E_2 are the energy of L_1 and L_2, T is the temperature of the system. Considering the multiplicity g_J of the energy level, where J is the angular momentum quantum number and $g_J = 2J + 1$ (total number of the magnetic quantum number), Equation (3-48) can be transformed into the relation between N_2 and the total number density N of atoms in all kinds of states by,

$$\frac{N_2}{N} = \frac{g_2}{z(T)} exp[-\frac{(E_2 - E_1)}{kT}] \tag{3-49}$$

where g_2 is the multiplicity for L_2, $z(T)$ is the sum of the atomic states given by,

$$z(T) = \sum_m g_m \, exp[-\frac{E_m}{kT}] \tag{3-50}$$

The distribution of the atoms in different energy levels is then described as a function of energy and temperature.

- **Maxwell-Boltzmann distribution of the particle speed**

The Maxwell-Boltzmann equation, on the other hand, describes the speed distribution of the particles in a thermal equilibrium state. The distribution function $F(v)$ is given by,

$$F(v)dv = 4\pi v^2 (\frac{m}{2\pi kT})^{\frac{3}{2}} exp(-\frac{(1/2)mv^2}{kT})dv \tag{3-51}$$

where m is the mass of the particle, v is the derived by,

$$v = ({v_x}^2 + {v_y}^2 + {v_z}^2)^{1/2} \tag{3-52}$$

The v_x, v_y, v_z are the speed of the particle in the three dimensions. Using equation (3-51), the distribution of the kinetic energy for a set of particles can be determined. An example of the Maxwell-Boltzmann distribution for the hydrogen atoms at a temperature of 300 K is shown in Fig. 90.

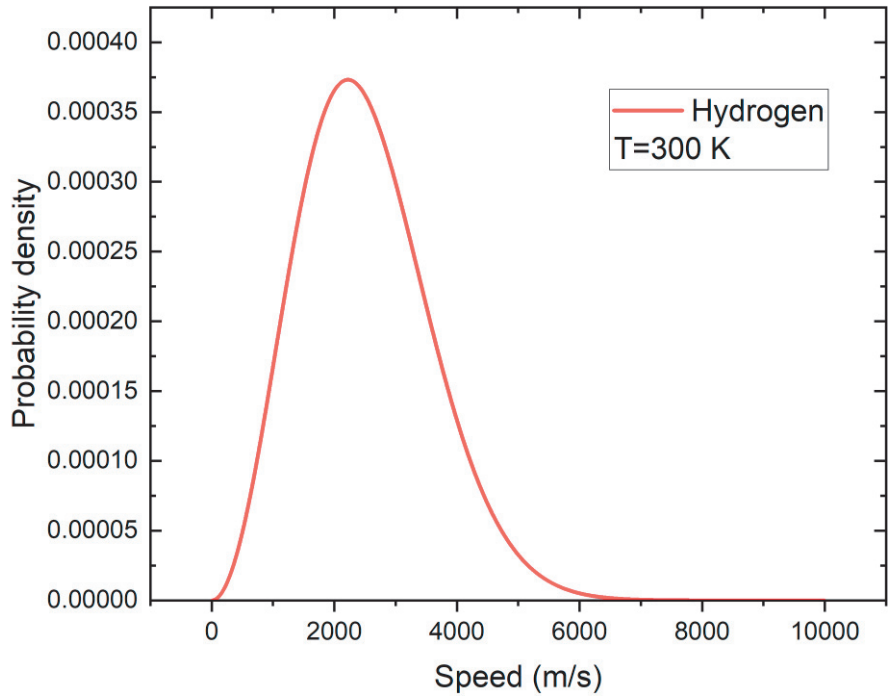

Fig. 90: Maxwell-Boltzmann distribution for hydrogen atoms at a temperature of 300 K.

- **Idea equation of state**

For an idea gas in the thermal equilibrium condition, its temperature T, pressure P, and the particle number density N follow by,

$$P = NkT \tag{3-53}$$

where k is the Boltzmann constant. This equation will be utilized in 3.3.4 to calculate the important factor P and N for the plasma thermodynamic simulations [105].

- **Saha equation**

The Saha equation describes the relation of the number density N between the ions with two different ionization states Z and $Z+1$, as a function of the temperature, density, and ionization energies of the atoms. The equation is given by,

$$N_e \frac{N_{Z+1}}{N_Z} = 2\frac{z_{Z+1}(T)}{z_z(T)}\frac{(2\pi m_e kT)^{3/2}}{h^3} exp(-\chi_z/kT) \tag{3-54}$$

where N_e is the electron density, N_Z and N_{Z+1} are the number density of the ions with corresponding ionization states, $z_z(T)$ is the sum of the states in ionization states Z, χ_z is the ionization energy from Z to $Z+1$, h is the Plank constant, m_e is the electron mass.

- **Opacity (Optical thickness)**

The opacity for the LPP plasma is important to estimate the self-absorption inside the plasma. The blackbody is an ideal radiation object; however, all radiations emitted can be reabsorbed and vice versa. When the short wavelength emissions are emitted from the hot dense center of the plasma, the radiation suffers from the self-absorption from the outer side of the plasma. The process may significantly reduce the brightness of the WW source.

To quantify this problem, a two-energy-level system was established, where the number densities are denoted as N_1 and N_2, corresponding to quantum levels L_1 and L_2. The number of emissions from L_2 to L_1 per unit time per unit volume is then given by,

$$A_{21}N_2h\nu_0 \tag{3-55}$$

where A_{21} is the Einstein A coefficient, which refers to the ratio of the number of atoms, n, over the time interval Δt for spontaneous emission per unit time (Δt is the time interval between two spontaneous emissions for n atoms). Assuming the emission is isotropic, the emission energy ε per unit solid angle, per unit time, per unit volume is given by,

$$\varepsilon = (1/4\pi)A_{21}N_2h\nu_0 \tag{3-56}$$

where ε is named as the emission coefficient for the emission spectra. This emission coefficient needs to be normalized by the normalized profile function $g(\nu)$ as,

$$\varepsilon = (1/4\pi)A_{21}N_2h\upsilon_0 g(\nu) \tag{3-57}$$

This is because the spectra are not homogeneous. Now considering an absorption coefficient $\kappa(\nu)$ (normalized by the profile $g(\nu)$) for a unit length in the plasma, the emissions are initially emitted from the ions and reabsorbed by other ions, where both absorption and stimulated emission occur.

$$\int \kappa(\nu)\delta\nu = \left(\frac{h\upsilon_0}{c_0}\right)[B_{12}N_1 - B_{21}N_2]\, g(\nu) \tag{3-58}$$

where B_{12} and B_{21} are the Einstein B coefficient. The equation describes the absorption and the stimulated emissions.

Next, the variation for the spectra radiance $L(\nu, z)$ in a distance $(z + \mathrm{d}z)$ is given as

$$L(\nu, z+dz)d\nu = L(\nu, z)d\nu - \kappa(\nu, z)L(\nu, z)d\nu dz + \varepsilon(\nu, z)d\nu dz \tag{3-59}$$

The first term on the right side of the equation is the initially spectra radiance, affected by the absorption term $\kappa(\nu, z)L(\nu, z)$ and spontaneous emission term $\varepsilon(\nu, z)$. Therefore, the

increasement for $L(\nu, z)$ in $(z + dz)$ is given by

$$\frac{dL(\nu, z)}{dz} = \varepsilon(\nu, z) - \kappa(\nu, z)L(\nu, z) \tag{3-60}$$

Integrating the equation (3-60) (calculation process refers to the Lambert-Beer law), the spectra radiance $L(\nu, z)$ can then be described as

$$\begin{aligned} & L(\nu, z) \\ & = L(\nu, 0)\, exp\left[-\int \kappa(\nu, z)dz\right] \\ & + exp\left[-\int \kappa(\nu, z)dz\right]\int \varepsilon(\nu, z)\, exp[\int \kappa(\nu, z)dz]dz \end{aligned} \tag{3-61}$$

Now if the plasma thickness in the z direction is l with a homogeneous condition, where $\varepsilon(\nu, z)$ and $\kappa(\nu, z)$ become $\varepsilon(\nu)$, $\kappa(\nu)$. The spectra radiance for the beam light at a propagating distant l can be described as

$$\begin{aligned} L(\nu, l) = L(\nu, 0)\, exp[-\kappa(\nu)l] \\ + [\varepsilon(\nu)/\kappa(\nu)]\{1 - exp[-\kappa(\nu)l]\} \end{aligned} \tag{3-62}$$

where $[\varepsilon(\nu)/\kappa(\nu)]$ is known as the source function, describing the ratio of the emission coefficient to the absorption coefficient.

- **Local thermal equilibrium (LTE) model**

The elementary processes discussed above satisfy thermal equilibrium conditions. In practical, the plasma produced by the laser pulse cannot reach such state. Therefore, an alternative method is required to break down this complex process into solvable parts. This section introduces different models in a non-equilibrium plasma, which focus on the dominate process within the plasma.

When the plasma is optically thin, meaning that re-absorptions and stimulated emissions are relatively weak within the plasma compared with the spontaneous emissions, some excitation processes are required to maintain the plasma in the condition as thermal equilibrium (for example, the number density follows the Boltzmann distribution). Usually, the process is the collision process (excitation/deexcitation and ionization/recombination). The LTE model describes a condition where the ion and electron densities are extremely high that, the collision process dominates and maintains the plasma in an equilibrium state, especially, high Rydberg states. It is clear that equations for describing the ideal gas, such as the Maxwell-Boltzmann equation is not satisfied with this condition. While the Saha equation is satisfied for the plasma in LTE.

The LTE model is often used to approximate the adiabatic expansion at the initial period of the LPP [104].

- **Boltzmann transport equation**

To describe the particles motion due to the collision, the Boltzmann transport equation is used. The system consists of a spatial coordinate (x, y, z) and a velocity coordinate (w_x, w_y, w_z). The velocity distribution function $f(t, \boldsymbol{r}, \boldsymbol{w})$ is then given by,

$$\frac{\partial f}{\partial t} + \boldsymbol{w} \cdot \frac{\partial f}{\partial \boldsymbol{r}} + \frac{\boldsymbol{F}}{m} \cdot \frac{\partial f}{\partial \boldsymbol{w}} = \left(\frac{\partial f}{\partial t}\right)_{collision} \tag{3-63}$$

where $\boldsymbol{r}$ and $\boldsymbol{w}$ are the vectors in the spatial coordinate and velocity coordinate, respectively. $\boldsymbol{F}$ is the external force applied on the particles, m is the mass of the particle. The first term refers to the variation of the distribution function f. The second term describes the gradient of the velocity $\boldsymbol{w}$, while the third term represents the external force affecting the velocity of the particles. The term on the right side of the equation is the distribution function caused by the collision process.

- **Equation of continuity**

To solve the upper equation during the numerical calculation, the following equations are required. For the particle density N, the equation of continuity is given by,

$$\frac{\partial N}{\partial t} + \nabla \cdot (N\boldsymbol{v}) = \left(\frac{\partial N}{\partial t}\right)_S \tag{3-64}$$

The first term represents the increasing of the particle density, while the second term describes the reduction of the density due to the out flowing in the velocity $\boldsymbol{v}$. The summation of the two terms is defined as the source term.

When treating the plasma as a fluid, equation (3-64) can be convert to the conservation of mass, written as [105]

$$\frac{\partial \rho}{\partial t} + \nabla \cdot (\rho \boldsymbol{w}) = 0 \tag{3-65}$$

where $\rho(\boldsymbol{r}, t)$ is the mass density and $\boldsymbol{w}(\boldsymbol{r}, t)$ is the velocity for a mass element positioned at $\boldsymbol{r}$ at time t. The source term is neglected at this condition.

- **Equation of motion**

The conservation of momentum for the particles are given by,

$$Nm\left[\frac{\partial \boldsymbol{v}}{\partial t}+(\boldsymbol{v}\cdot\nabla)\boldsymbol{v}\right]=Nq(\boldsymbol{E}+\boldsymbol{v}\cdot\boldsymbol{B})-\nabla\cdot\Psi-Nm\nabla\phi+\boldsymbol{P} \tag{3-66}$$

where Ψ is known as the stress tensor, which is defined as a vector field of forces in a unit volume. The left side of the equation (3-66) represents the rate of change of particle momentum within unit volume with time, and the transport of momentum. The first term on the right side of the equation (3-66) refers to the Lorentz force. The second term is the gradient driven term. The third term describes force from the potential energy ϕ in the electric field, and finally, the pressure P.

- **Energy conservation**

When treating the plasma as a moving fluid, the energy conservation can be written as [105],

$$\int_{\Gamma}\rho\frac{D(v^2/2)}{Dt}dV+\int_{\Gamma}\rho\frac{D_{\varepsilon}}{Dt}dV=Q_{ext}+Q_H+W_F+W_f \tag{3-67}$$

where the terms on the left side refer to the total kinetic energy and total internal thermal energy changed per unit volume with time. Q_{ext} is the external energy source (laser heating in this case). Q_{H} is the heat conduction, W_{F} is the work per unit time done by the volume force, and the work per unit time done by the surface force W_{f}. D/Dt is the Lagrangian derivative.

Another form of the equation (3-67) for the metal absorbing the laser pulse is written as [106],

$$c_e(T_e)\frac{\partial T}{\partial t}=\chi\Delta T_e-\alpha(T_e-T_i)+f(\boldsymbol{r},t) \tag{3-68}$$

$$c_i\frac{\partial T_i}{\partial t}=\alpha(T_e-T_i) \tag{3-69}$$

where $c_e(T_e)$ is the specific heat capacity of electrons, χ is the thermal conductivity coefficient, α is the parameter describing the energy transfer between ions and electrons (similar to the γ in equation (1-11)). Since electrons are much easier to transfer heat than the ions, the temperature changing for ions is described by equation (3-69). The parameter of $f(\boldsymbol{r},t)$ refers to the external energy source as $Q_{ext}.\nu$

- **Coronal model**

For the extreme opposite case to the LTE model, the coronal model was proposed. It describes the plasma with low electron density while still maintaining a quasi-thermal equilibrium. In this condition, the emission process dominates the plasma, while the collisional deexcitation process can be ignored. The sun is usually cited as an example for the coronal

model, as its electron temperature can reach 10^6 K while the electron density can only reach 10^{14}-10^{15} m^{-3} [107]

- **Collisional radiative (CR) model**

In the thermal equilibrium plasma, many equations such as the Boltzmann equation, the Maxwell-Boltzmann equation, the Planck's equation, and the Saha equation can be applied to calculate the relation between spectra and temperature, or the population density between the states in atom and ion. While in the case of local thermal equilibrium, the radiation process can be negligible for a collision-dominated plasma. In the coronal mode, the collision can be ignored from the deexcitation process due to the low density, high temperature plasma. However, the plasma generated by the laser pulse cannot be classified into a thermal equilibrium/corolal condition. Consequently, both radiation and collision are necessary to be considered. A general equation to describe the collisional radiative (CR) mode is,

$$\frac{\partial N_m^{(z+1)}}{\partial t} + \nabla \cdot \left(N_m^{(z+1)} v\right) = \sum C_i - \sum C_{j'} + \sum R_k - \sum R_{l'} \qquad (3\text{-}70)$$

where C_i and R_k are the increasing rate for $N_m^{(z+1)}$ from the i type collision and k type radiation, respectively. $C_{j'}$ and $R_{l'}$ are the decreasing rate for $N_m^{(z+1)}$ from the j' type collision and l' type radiation [107].

3.3.4 Principle of Star-2D code

The Star-2D code was utilized to validate the experimental results described in the next chapter. The system is shown in Fig. 91, where the 1D Lagrangian method combined with the Eulerian method is used to calculate the plasma expansion process, and the vacuum space is set as a thin Au gas atmosphere for the calculation. The element set for the substrate layer is also Au but with a density of SiO_2. Electrons and ions are treated in a one-fluid two-temperature mode. The SESAME EOS table [108] and the opacity table calculated based on the screened hydrogenic averaged ion model [109] are adopted. The system is assumed to be axially symmetry in cylindrical coordinates (z, r) and is unequally divided into cells as shown in Fig. 91. The intersections of the grids are defined as the local isodensity point. A 2D simulation box with 400(z) × 200(r) grid cells is shown in the left panel of Fig. 91, where the Au target surface is set at z = 0 μm and the substrate glass shown in yellow is set right behind it. The right panel in Fig. 91 shows a magnified view of the 1.2-μm-thick Au target surface as an example. The red lines represent the cells in the Au–gas and Au–glass boundaries. The laser parameters are set to be the same to the similar condition (spot size: 15 μm FWHM, laser power: 1×10^{13} W/cm^2) as using the 240-mJ pulse during in the experiment.

The basic equations to describe the particle motions in the Star-2D code are given by [104,110,111],

$$\frac{D\rho}{Dt} = -\rho \nabla \cdot \boldsymbol{v} \qquad (3\text{-}71)$$

$$\rho \frac{D\boldsymbol{v}}{Dt} = \nabla(p_i + p_e) \tag{3-72}$$

$$\rho c_{Vi} \frac{DT_i}{Dt} = -p_{thi} \nabla \cdot \boldsymbol{v} - Q_{ei} \tag{3-73}$$

$$\rho c_{Ve} \frac{DT_e}{Dt} = -p_{the} \nabla \cdot \boldsymbol{v} + Q_{ei} + \nabla \cdot (k_e \nabla T_e) + S_e \tag{3-74}$$

where ρ is the mass density, $\boldsymbol{v}$ is the velocity, T_e and T_i are the temperature of electrons and ions (or lattice), p_i and p_e are the pressure of ions and electrons (given by $p = p(\rho, T)$), p_{thi} and p_{the} is defined by,

$$p_{thi=} p_{thi}(\rho, T_i) = T_i (\frac{\partial p_i}{\partial T_i})_\rho \tag{3-75}$$

$$p_{the=} p_{the}(\rho, T_e) = T_e (\frac{\partial p_e}{\partial T_e})_\rho \tag{3-76}$$

which are based on the equation of state as illustrated in equation (3-53). The value Q_{ei} is the energy transfer between electrons and ions ($\alpha(T_e - T_i)$ in equation (3-69)), S_e is the external energy source (Q_{ext} in equation (3-67)), k_e is the thermal conductivity. c_{Ve} and c_{Vi} are the specific heat capacity of electron and ion, respectively, which are also defined as $c(\rho, T)$.

The equation (3-71) is the conservation of mass, as illustrated in equation (3-65). The equation (3-72) is the conservation of momentum, similar to the equation (3-66). The change in momentum (left side) equals to the momentum transport due to the pressure gradient. This equation is also known as part of the Navier–Stokes equations.

The equations (3-73) and (3-74) are the conservation of energy, which are slightly different with equations (3-68) and (3-69).

Utilizing the database illustrated above, these formulae can be solved and the thermodynamic of the particles can be investigated.

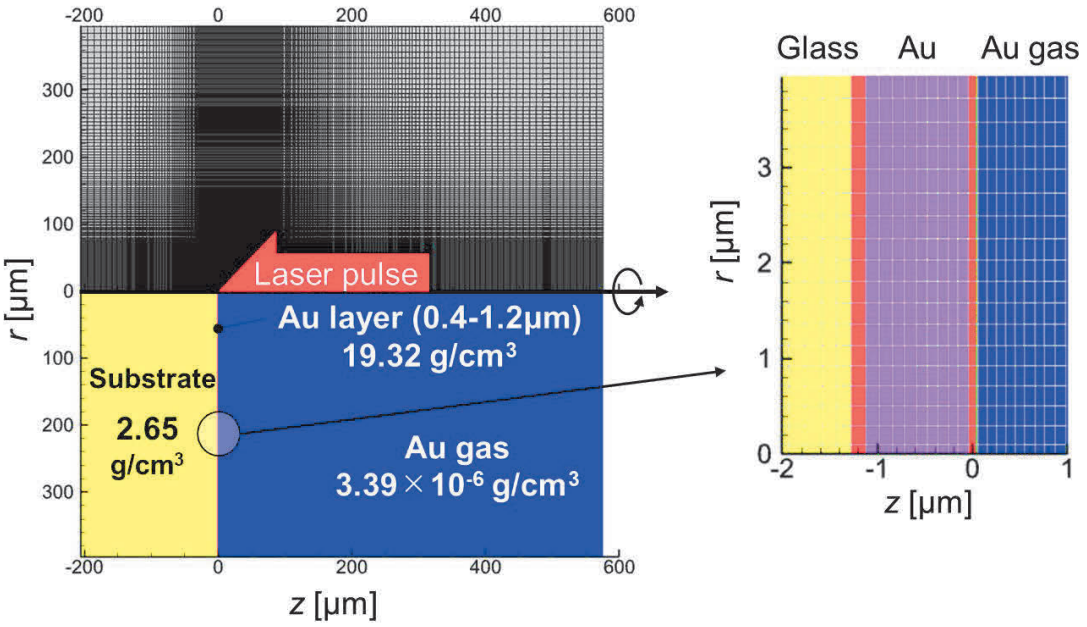

Fig. 91: Left panel: 2D simulation box shown in grid mode (upper) and schematic mode (lower). The laser incidence center axis is defined as the negative z-direction, while $r = 0$ is defined as the irradiation center. Right panel: Magnified view of grid cells around the target surface, showing glass (yellow), Au (pink), and gas (blue) layers. The red regions indicate the boundary between two layers, and $z = 0$ is set as the surface of the Au layer.

3.3.5 Simulation results of Au layer ablation

The underlying mechanisms of the emission behavior in Au plasma generated from targets of various thicknesses were attributed to the gradual decrease of Au atomic layer in the laser ablation region. Therefore, the motion of the Au-glass boundary $Z_{bnd}(r,t)$ was traced using the Star-2D code. The laser energy was set 240 mJ to give a comparison with the result in Fig. 83. Fig. 92 shows the distribution of the plasma 0.05 ns after the peak intensity of the Gaussian laser pulse reached the Au surface. The plasma status is described by the electron density n_e, electron temperature T_e, laser absorption, and totoal pressure, respectively. The most effective laser absorption is found at the critial density region $n_e = 10^{21}\ cm^{-3}$, where the laser could hardly penetrate. Electron temperature at the center of the plasma is found at around 300 eV which is suitable for the Au plasma to emit WW x-rays. The boundary of Au-galss is shown by the black and white line in each plot, which is compressed to the incide of the target as shown by the total pressure. The region where electron temperature is over 250 eV is shown to be less than 50 μm, and this is in a good agreement with the image observed by the pinhole image. Au atoms still exist on the target surface, which contributes to the WW emission.

However, the boundary is blown away to the outside of the target when the center of the total pressure propagates into the glass substrate. This happens about 1 ns after the laser peak time (11.4 ns) as shown in Fig. 93. The Au ions are displaced toward the outer region of the plasma center, while Si and O ions are effectively heated at this time. As a result, the GIS

image integrates intense line spectra attributed to the glass plasma. However, WW spectra could hardly be observed at this time since the boundary $Z_{bnd}(r,t)$ is distant from the center, and Au ions are only present in the low-temperature region.

To understand the physical dynamics and emission behavior when using targets with different thicknesses, the temporal evolution of the boundaries in the plasma generated by targets with various thicknesses were traced. Fig. 94 shows the average temporal evolution of the Au–glass boundary (upper panel) when using different Au targets (thicknesses of 0.4 μm, 0.6 μm, 0.8 μm, 1.0 μm, and 1.2 μm), compared with the time evolution of the laser irradiation $I_L(t)$ normalized by the peak intensity $I_{L,peak}$ (lower panel). The laser peak time is set to be t = 0. $Z_{bnd}(r,t)$ ranging from r = 0 μm to r = 7.5 μm is averaged and defined as $Z_{bnd}(t)$, which is exactly the half-width at half-maximum (HWHM) of the tightly focused laser spot. Note that the initial position of the boundary is defined as Z_{bnd} = 0. During the irradiation, the boundary moves initially in the negative z-direction due to shock propagation driven by the laser irradiation and the ablation pressure. After the thin Au layer is fully ablated, the SiO_2 layer is directly irradiated by the laser, and the boundary starts to move in the positive z-direction.

For Au thicknesses above 0.8 μm, the laser peak intensity (t = 0 ns) passes before the Au layer is fully ablated and only the Au layer is ablated at the peak intensity. For target thicknesses below 0.6 μm, the Au layer is fully ablated before the occurrence of the laser peak intensity, leading to intense ablation of the glass layer, causing intense line spectral emissions from the irradiation center, while the outer Au plasma continues emitting x-rays. Consequently, both line and UTA spectra are observed in this case, which quantitatively explains the dependence of the WW emission on the Au thickness in the experimental results.

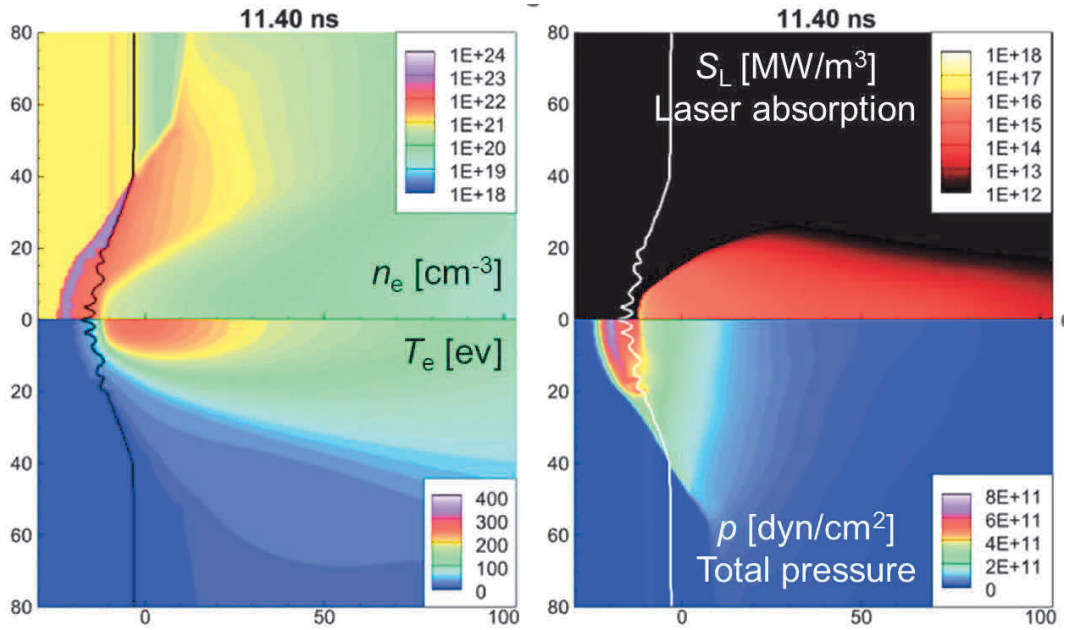

Fig. 92: Plasma dynamics near the peak time (11.4 ns), when a 1-μm Au target was irradiated by the laser power of 1×10^{13} W/cm^2. The four plots show electron density n_e, electron temperature T_e, laser absorption, and totoal pressure, respectively. The black and white lines refer to the glass-Au boundary.

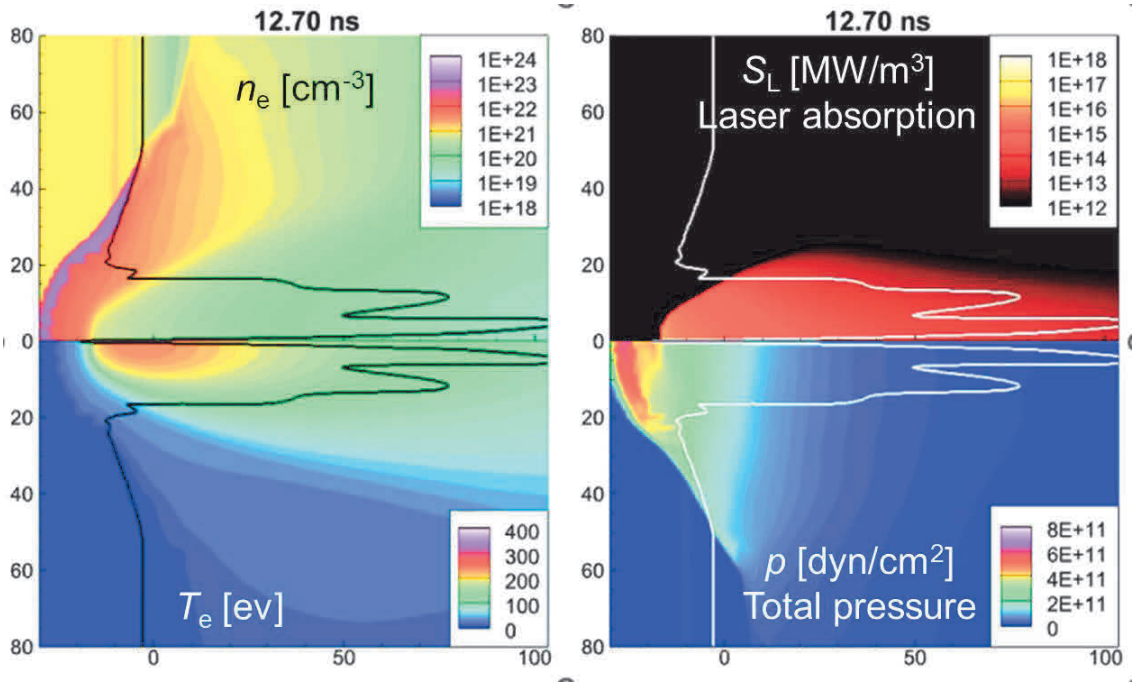

Fig. 93: The plasma dynamics 1.3 ns after the peak time.

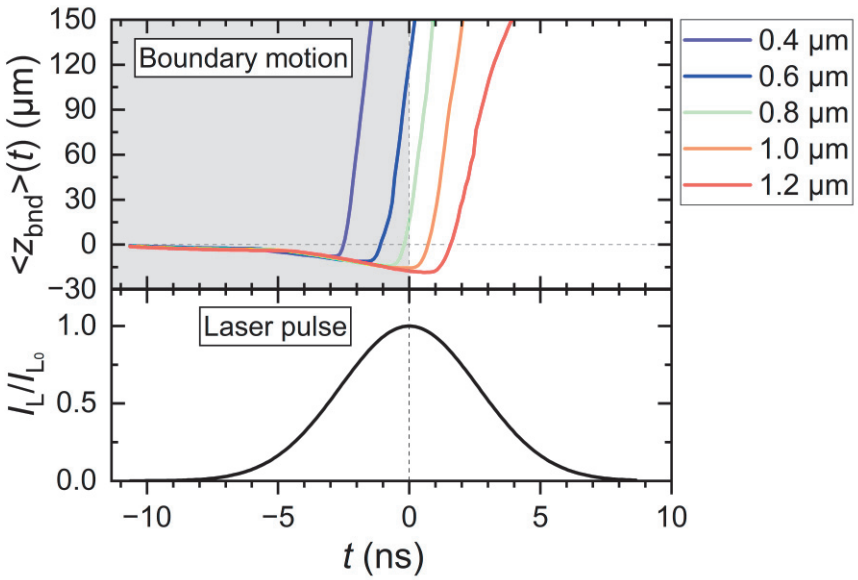

Fig. 94: Upper panel shows average temporal evolution of Au–glass boundary during laser irradiation. The laser irradiated the Au targets as shown by the red arrow. $Z_{bnd} = 0$ represents the initial z-position of the boundary as shown by the horizontal grey dashed line. The lower panel shows the laser irradiation time evolution.

3.4 Optimal focus condition for WW x-ray source

The alteration in focal distance not only affected the irradiation power but also determined the plasma plume generated from the irradiation region based on the spot size. To examine WW x-ray emission under various laser focus conditions, precise positioning of the lens is necessary. In this section, the optimal focus condition was investigated by changing the distance between the target and the focus lens. The theoretical variation for the focused laser spot was compared to the experimental one, as a very good laser beam quality was even difficult to achieve. The Star-2D was also utilized to evaluate the experimental results.

3.4.1 Lens scanning

The focused laser spot sizes for different lens positions were measured for both 240 mJ and 650 mJ laser energies using a 50-μm-thick Au foil as a target. The target position was defined such that x = 0 mm with the Au front surface precisely placed at the focal point of the focus lens. The spot size at the focal point was 15 μm. Note that the target was fixed as a reference point during the entire measurement and the lens was moved back and forth with respect to the reference point with the positive direction corresponding to a position with the target behind the focal point. Fig. 95 shows the focused laser spot images and pinhole images of the Au plasma (1.0-μm- and 0.5-μm-thick Ti filters) observed for various target positions. The laser spot images were measured by a CMOS camera by moving the sensor surface perpendicular to the *x*-axis. Within the Rayleigh length Z_R = 664 μm, almost all the laser spots had the same FWHM of 15 μm, and the soft x-ray emission areas were larger than the focused laser spot. As the spot shape started to blur as the target position was further changed, the laser spot and emission area became asymmetrical, resulting in a scattered x-ray distribution. The variation in the focused laser spot can be attributed to the laser beam profile quality. Therefore, the spot size could no longer be calculated correctly. The laser spot shape remains similar when the target position moved to the positive direction, although the intensity gradually decreases. The energy distribution tends to be stable after the beam is focused onto the focal point and irradiated the Au target behind. Compared with x-ray emission for $x < 0$ mm, plasmas for $x > 0$ mm are likely to radiate more centralized WW emission, because of the more uniform Gaussian-distributed laser energy.

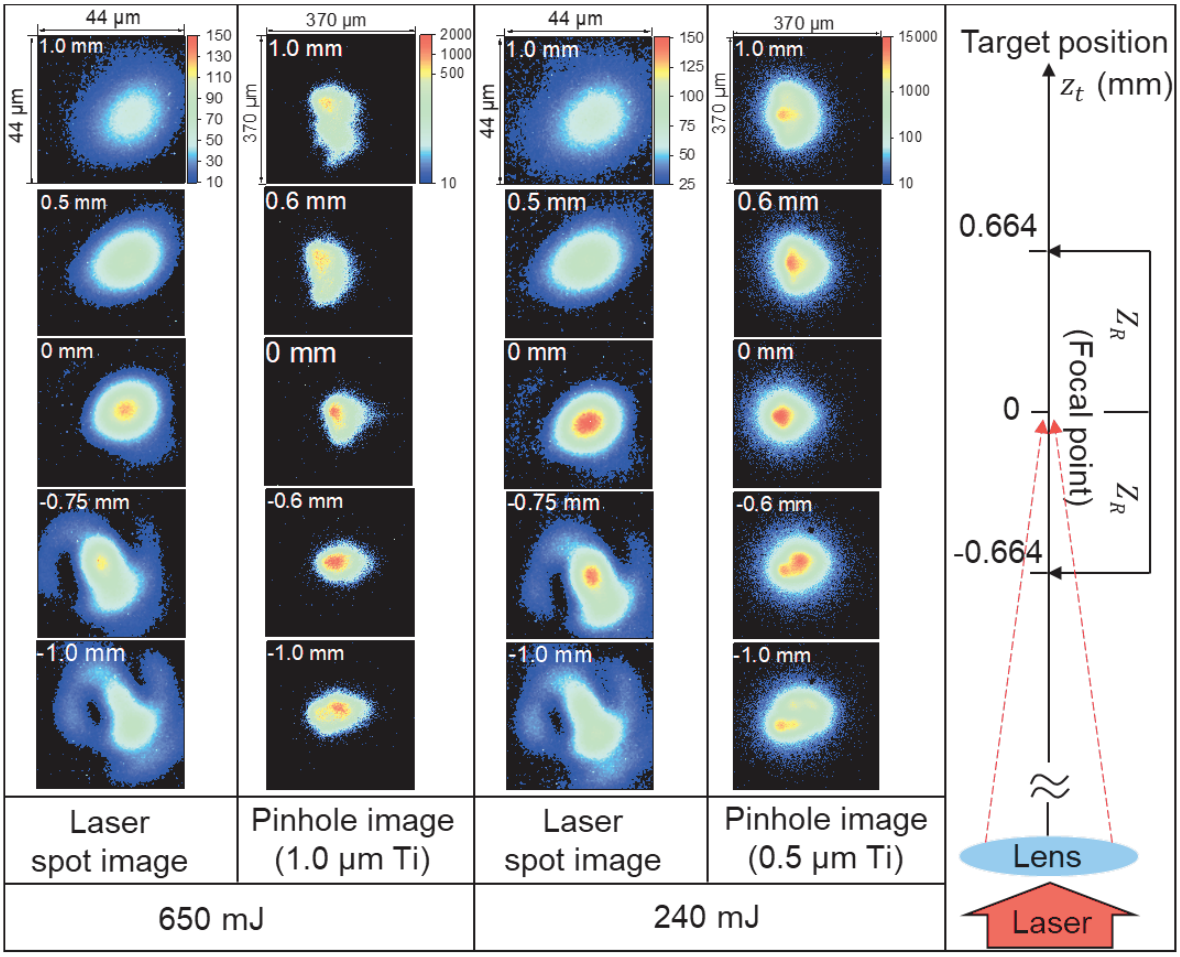

Fig. 95: Variations in laser spot images and pinhole images under different focus conditions. The target position was adjusted by moving the lens, and increasing the focus distance corresponds to the positive direction. The x axis shows the focus condition for different target positions. In the right panel, the Rayleigh length Z_R and the focal point are denoted.

3.4.2 Dependence of Au spectra on target position

WW emissions from plasma for various target positions were measured by the GIS, as shown in Fig. 96 and Fig. 97 for 650 mJ and 240 mJ laser energies, respectively. An enhancement of the WW region is observed around $x = -1.0$ mm and 1.0 mm for 650 mJ laser energy and $x = -0.8$ mm and 0.6 mm for 240 mJ. Note that the GIS was not calibrated in terms of the toroidal mirror, grating and CCD sensitivities. The peaks in the WW region are plotted as scatter-lines. The spectral peaks shift to shorter wavelength as the target approaches $x = 0$ mm, showing that Au ions with higher ionic charge are generated and dominate in the hot dense plasma.

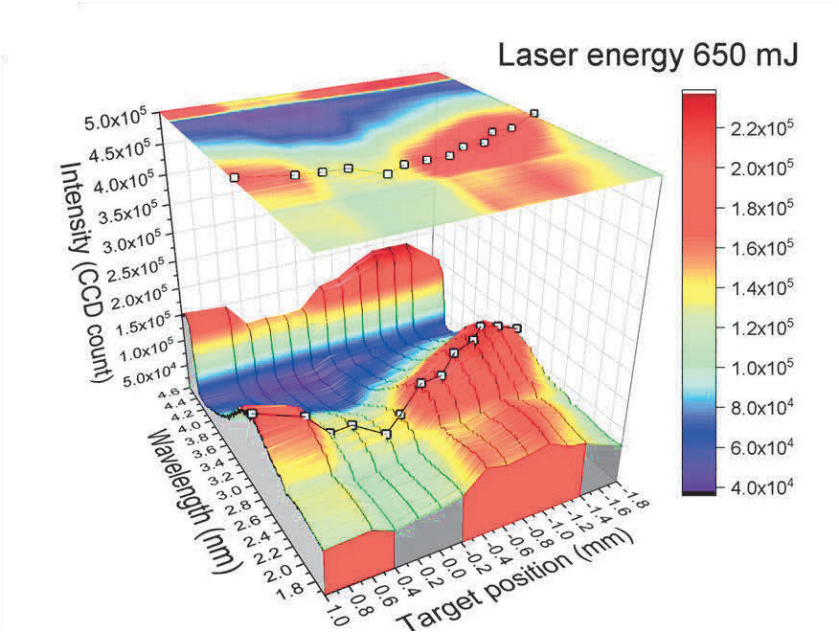

Fig. 96: GIS spectra as function of target position for Au plasma produced by 650 mJ laser irradiation. 2D contour plot is shown above the 3D plot. The scatter line represents the peak WW wavelength of the corresponding 4*f*-5*g* transitions.

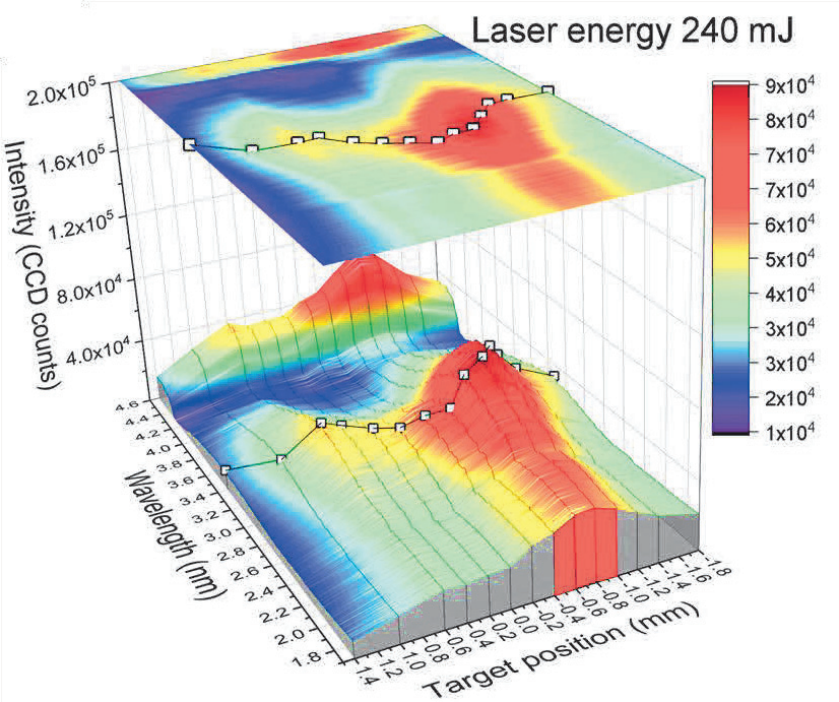

Fig. 97: GIS spectra as function of target position for Au plasma produced by 240 mJ laser irradiation. 2D contour plot is shown above the 3D plot. The scatter line represents the peak WW wavelength of the corresponding 4*f*-5*g* transitions.

The X-ray yield trend can be explained as follows. The density scale length is strongly dependent on the spot size of plasma generated by nanosecond laser pulses. When the laser spot is moved away from the focal point, the density scale length becomes larger, providing a larger plasma plume. As the area for laser–plasma interaction increases, coupling between the plasma temperature and plasma plume volume produces a larger area favorable for WW emission at a slightly lower temperature [112,113]. Consequently, two WW emission peaks were observed at the two sides of the focal point position, with slightly increased peak wavelength. Beyond the peak position, the insufficient laser intensity leads to a drop in both spectral intensity and peak wavelength, as shown in Fig. 96 and Fig. 97.Therefore, the optimal focus conditions providing a suitable laser irradiation intensity and Au plasma size for WW emission are x = −1.0 mm (spot size: 25 μm FWHM, intensity: 1.39×10^{13} W/cm^2) and x = −0.8 mm (spot size: 19 μm, intensity: 8.89×10^{12} W/cm^2) in the current experimental condition.

3.4.3 Simulation results

To further investigate the dependence of emission characteristics on laser focusing conditions, the Star-2D code was utilized to simulate the temporal evolution of the plasma parameters for different irradiation spot sizes. The laser intensity and spot size on the target were varied for the fixed laser energy of E_L = 650 mJ and pulse duration of τ_L = 6.2 ns. Table 1 shows the parameter settings for STAR-2D. The simulations were carried out for three spot sizes ϕ_L (FWHM) and intensities $I_{\mathrm{L,peak}}$: (ϕ_L, $I_{\mathrm{L,peak}}$) = (15 μm, 3.9×10^{13} W/cm^2), (33.5 μm, 0.77×10^{13} W/cm^2) and (47.4 μm, 0.39×10^{13} W/cm^2), corresponding to target positions of x = 0 mm (focus position), −1.3 mm, and −2.0 mm, respectively. Fig. 98 shows the spatial profile of electron temperature (T_e) and electron density (n_e) at the laser peak intensity. The electron temperature reaches over 300 eV corresponding to the region where Au XXI – XXXI ions are generated. When the target is located at the focus position (x = 0 mm, ϕ_L = 15 μm $I_{\mathrm{L,peak}}$ = 3.9×10^{13} W/cm^2), the plasma temperature exceeds 500 eV, which is far beyond the optimal electron temperature for WW emission (~400 eV). The width of the heated plasma is narrow due to the small spot size. Consequently, the peak wavelength of emitted soft x-ray becomes shorter, and the emission region is small. Contrary to this, when the target is located far away from the focus position (x = -2.0 mm, ϕ_L = 47.4 μm, $I_{\mathrm{L,peak}}$ = 0.39×10^{13} W/cm^2), the laser intensity is too low to produce plasma having the suitable temperature for WW emission, even though the plasma heated by the laser is much wider than that for the small spot size. In the present laser condition (E_L = 650 mJ and ϕ_L = 6.2 ns), the optimal laser irradiation condition forming suitable temperature T_e and heated plasma volume for WW emission is ϕ_L = 33.5 μm, corresponding to a target position of x = −1.3 mm. These results show that the WW emission trends from the simulation are in a good agreement with the experimental results.

Table 1: Parameter settings for Star-2D simulation

Spot size ϕ_L [μm]	15	33.5	47.4
Peak intensity $I_{L,peak}$ [10^{13} W/cm^2]	3.9	0.77	0.39
Target position [mm]	0	-1.3	-2.0

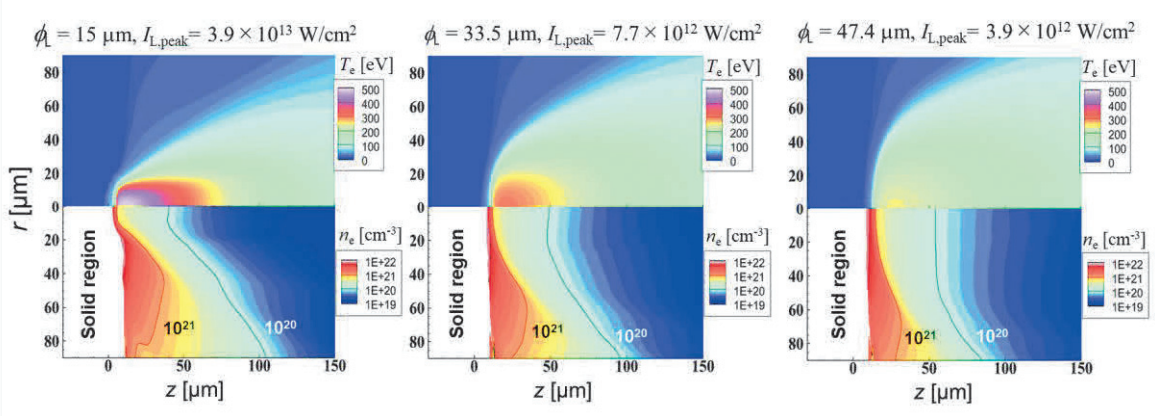

Fig. 98: Plasma profile at peak of laser irradiation intensity (t = 11.4 ns).

4. SUMMARY

Developing practical WW x-ray sources based on LPP requires a deep understanding of the plasma generation process and the radiation properties. Both emission spectroscopy and numerical simulations are crucial to characterize the plasma production and emission behavior in WW x-ray wavelengths.

In this work, a fundamental measurement for the laser-produced Au plasma using the GIS and pinhole camera was conducted. Combined with a FAC numerical calculation, the essential transitions for the Au UTA emission in the WW wavelength region has been confirmed to be 4*d*-4*f* and 4*f*-5*g* transitions in the Au^{20+}-Au^{30+} ions. A push broom scanning using the GIS with a spatial resolution of 50 μm was tested to be feasible.

The main objective of this work, the optimal Au target thickness for WW x-ray emission, was measured to be 1.3 μm and 0.6 μm for the laser power of 3.86×10^{13} W/cm^2 and 1.43×10^{13} W/cm^2, respectively. These minimum thicknesses are mainly attributed to the Au layer of being blown away by the laser shock wave.

A favorable focus condition for the laser-produced Au plasma to emit WW x-rays was also found, when setting the Au target surface 1.0 mm and 0.8 mm before the focal point of the focus lens for laser power of 3.86×10^{13} W/cm^2 and 1.43×10^{13} W/cm^2, respectively. The optimal coupling for the electron temperature and the plasma volume was considered to be the reason for this optimal focus condition.

The Star-2D code played an important role in data analysis, providing the theoretical explanations for the observed emission behaviors.

5. ACKNOWLEDGMENT

When I initially decided to pursue the Ph.D. course, I was filled with uncertainty and apprehension about the unknown research journey. However, during my Ph.D. studies, I encountered numerous mentors who profoundly impacted my life. They not only provided academic guidance but also inspired me with their unwavering dedication to research. Therefore, I extend my sincere gratitude and deep respect to the mentors in my research studies, whose influence will stay with me throughout my life.

First and foremost, I would like to express my deepest appreciation to my supervisor, Prof. Shinichi Namba, for his invaluable guidance, support, and encouragement throughout the entire journey of my research. His dedication and insightful feedback have been instrumental in shaping the direction of this thesis.

I am deeply thankful to the members of my thesis committee, Prof. Takuma Endo, Prof. Tomoyuki Jozaki, and Prof. Shuhei Inoue, for their constructive comments and thoughtful suggestions, which greatly enhanced the quality of my work.

I would like to express my sincere gratitude to Prof. Maki Kishimoto, Prof. Takeshi Higashiguchi, Dr. Atsushi Sunahara, Prof. Fumitaka Nishiyama, and Asst. Prof. Kotaro Yamasaki, for their collaboration and shared expertise, which significantly enriched the scope of my research.

My sincere thanks also go to my research fellows, Dr. Christian John, Mr. Kenta Murakami, Tomohiro Kumeda, Mr. Hikari Ohiro, Mr. Kairi Mizushima, and other members in the plasma science lab. It is their kind help and support that have made my study and life in the Hiroshima university a wonderful time.

6. REFERENCES

1. The Center for X-Ray Optics X-Ray Attenuation Length Available online: https://henke.lbl.gov/optical_constants/atten2.html (accessed on 4 December 2023).
2. Elliott, A.D. Confocal Microscopy: Principles and Modern Practices. *Curr Protoc Cytom* **2020**, *92*, doi:10.1002/cpcy.68.
3. Wang, S.; Larina, I. V 8 - High-Resolution Imaging Techniques in Tissue Engineering. In *Monitoring and Evaluation of Biomaterials and their Performance In Vivo*; Narayan, R.J., Ed.; Woodhead Publishing, 2017; pp. 151–180 ISBN 978-0-08-100603-0.
4. Zarraoa, L.; González, M.U.; Paulo, Á.S. Imaging Low-Dimensional Nanostructures by Very Low Voltage Scanning Electron Microscopy: Ultra-Shallow Topography and Depth-Tunable Material Contrast. *Sci Rep* **2019**, *9*, 16263, doi:10.1038/s41598-019-52690-9.
5. Eaton, P.; West, P. *Atomic Force Microscopy*; Oxford university press, 2010;
6. Bushberg, J.T.; Seibert, J.A.; Leidholdt, E.M.; Boone, J.M. *The Essential Physics of Medical Imaging(3rd Ed.)*; Lippincott Williams and Wilkins.;
7. Otón, J.; Pereiro, E.; Conesa, J.J.; Chichón, F.J.; Luque, D.; Rodríguez, J.M.; Pérez-Berná, A.J.; Sorzano, C.O.S.; Klukowska, J.; Herman, G.T.; et al. XTEND: Extending the Depth of Field in Cryo Soft X-Ray Tomography. *Sci Rep* **2017**, *7*, 45808, doi:10.1038/srep45808.
8. Tsai, E.H.R.; Usov, I.; Diaz, A.; Menzel, A.; Guizar-Sicairos, M. X-Ray Ptychography with Extended Depth of Field. *Opt. Express* **2016**, *24*, 29089–29108, doi:10.1364/OE.24.029089.
9. Röntgen, W.C. *Eine Neue Art von Strahlen*; Würzburg : Verlag der Stahel'schen k. Hof- u. Universitäts -Buch- u. Kunsthandlung, 1895., 1895;
10. Malsch, F. Erzeugung Stark Vergrößerter Röntgen-Schattenbilder. *Naturwissenschaften* **1939**, *27*, 854–855, doi:10.1007/BF01489432.
11. Spiller, E.; Feder, R.; Topalian, J.; Eastman, D.; Gudat, W.; Sayre, D. X-Ray Microscopy of Biological Objects with Carbon Kα and with Synchrotron Radiation. *Science (1979)* **1976**, *191*, 1172–1174, doi:10.1126/science.1257741.
12. Kishimoto, M.; Kado, M.; Ishino, M.; Tamotsu, S.; Yasuda, K.; Shinohara, K. Development of Single Shot Soft X-Ray Contact Microscopy System for Nano-Scale Dynamics Measurement of Living Biological Specimen.; 2012; pp. 43–47.
13. Shinohara, K.; Ito, A. Radiation Damage in Soft X-ray Microscopy of Live Mammalian Cells. *J Microsc* **1991**, *161*, 463–472, doi:10.1111/j.1365-2818.1991.tb03104.x.
14. Cheng, P.C.; Feder, R.; Shinozaki, D.M.; Tan, K.H.; Eason, R.W.; Michette, A.; Rosser, R.J. Soft X-Ray Contact Microscopy. *Nucl Instrum Methods Phys Res A* **1986**, *246*, 668–674, doi:10.1016/0168-9002(86)90171-3.
15. Wang, Y.; Jacobsen A Numerical Study of Resolution and Contrast in Soft X-ray Contact Microscopy. *J Microsc* **1998**, *191*, 159–169, doi:10.1046/j.1365-2818.1998.00353.x.
16. Smith, A.P.; Urquhart, S.G.; Winesett, D.A.; Mitchell, G.; Ade, H. Use of near Edge X-

Ray Absorption Fine Structure Spectromicroscopy to Characterize Multicomponent Polymeric Systems. *Appl Spectrosc* **2001**, *55*, 1676–1681, doi:10.1366/0003702011954008.
17. Niemann, B.; Rudolph, D.; Schmahl, G. X-Ray Microscopy with Synchrotron Radiation. *Appl. Opt.* **1976**, *15*, 1883–1884, doi:10.1364/AO.15.001883.
18. Uchida, M.; McDermott, G.; Wetzler, M.; Le Gros, M.A.; Myllys, M.; Knoechel, C.; Barron, A.E.; Larabell, C.A. Soft X-Ray Tomography of Phenotypic Switching and the Cellular Response to Antifungal Peptoids in Candida Albicans. *Proceedings of the National Academy of Sciences* **2009**, *106*, 19375–19380, doi:10.1073/pnas.0906145106.
19. Carlson, D.B.; Gelb, J.; Palshin, V.; Evans, J.E. Laboratory-Based Cryogenic Soft x-Ray Tomography with Correlative Cryo-Light and Electron Microscopy. *Microscopy and Microanalysis* **2013**, *19*, 22–29, doi:10.1017/S1431927612013827.
20. Legall, H.; Blobel, G.; Stiel, H.; Sandner, W.; Seim, C.; Takman, P.; Martz, D.H.; Selin, M.; Vogt, U.; Hertz, H.M.; et al. Compact X-Ray Microscope for the Water Window Based on a High Brightness Laser Plasma Source. *Opt Express* **2012**, *20*, 18362, doi:10.1364/OE.20.018362.
21. Fu, Q. RADIATION TRANSFER IN THE ATMOSPHERE | Cloud-Radiative Processes. In *Encyclopedia of Atmospheric Sciences*; Elsevier, 2015; pp. 13–15.
22. Baez, A. V Fresnel Zone Plate for Optical Image Formation Using Extreme Ultraviolet and Soft X Radiation. *J. Opt. Soc. Am.* **1961**, *51*, 405–412, doi:10.1364/JOSA.51.000405.
23. Lider, V. V. Zone Plates for X-Ray Focusing (Review). *Journal of Surface Investigation: X-ray, Synchrotron and Neutron Techniques* **2017**, *11*, 1113–1127, doi:10.1134/S1027451017060155.
24. Osakabe, T. Principles And Applications Of Multilayer Mirror Optics For X-Ray Diffraction Measurements —CBO Series For SmartLab. *Rigaku Journal* **2017**, *33*.
25. Kopylets, I.; Devizenko, O.; Zubarev, E.; Kondratenko, V.; Artyukov, I.; Vinogradov, A.; Penkov, O. Short-Period Multilayer X-Ray Mirrors for “Water” and “Carbon Windows” Wavelengths. *J Nanosci Nanotechnol* **2019**, *19*, 518–531, doi:10.1166/jnn.2019.16471.
26. Huang, Q.; Yi, Q.; Cao, Z.; Qi, R.; Loch, R.A.; Jonnard, P.; Wu, M.; Giglia, A.; Li, W.; Louis, E.; et al. High Reflectance Nanoscale V/Sc Multilayer for Soft X-Ray Water Window Region. *Sci Rep* **2017**, *7*, 12929, doi:10.1038/s41598-017-13222-5.
27. Luo, K.; Niu, S.; Shah, D.; Lonkar, A.; Liu, Y.; Ravichandran, J. Prediction of Perovskite and Other Ternary Oxide Multilayers as Mirrors for Soft X-Rays. *Mater Res Bull* **2018**, *98*, 206–212, doi:10.1016/j.materresbull.2017.10.018.
28. Hatano, T.; Ejima, T.; Ono, Y.; Dinh, T.; Tamura, T.; Hara, H.; Higashiguchi, T. Fabrication of Cr / Sc / Mo Multilayer Illuminator for Water Window Soft X-Ray Microscopes with Bi Plasma Sources. **2019**, *36*, 2018–2019.
29. Eriksson, F.; Johansson, G.A.; Hertz, H.M.; Gullikson, E.M.; Kreissig, U.; Birch, J. 14.5% near-Normal Incidence Reflectance of Cr/Sc x-Ray Multilayer Mirrors for the Water Window. *Opt Lett* **2003**, *28*, 2494, doi:10.1364/ol.28.002494.
30. Salashchenko, N.N.; Shamov, E.A. Short-Period X-Ray Multilayers Based on Cr/Sc. *Opt Commun* **1997**, *134*, 7–10, doi:10.1016/S0030-4018(96)00551-2.
31. Ishino, M.; Yoda, O.; Koike, M. Development of Multilayer Mirrors for Use in the

Wavelength Region of 4 Nm 2005, 13.
32. Bilderback, D.H.; Elleaume, P.; Weckert, E. Review of Third and next Generation Synchrotron Light Sources. *Journal of Physics B: Atomic, Molecular and Optical Physics* **2005**, *38*, S773–S797, doi:10.1088/0953-4075/38/9/022.
33. Gong, Z.; Mackenroth, F.; Yan, X.Q.; Arefiev, A. V. Radiation Reaction as an Energy Enhancement Mechanism for Laser-Irradiated Electrons in a Strong Plasma Magnetic Field. *Sci Rep* **2019**, *9*, 17181, doi:10.1038/s41598-019-53644-x.
34. Shabalin, Anatoly Coherent X-Ray Diffraction Studies of Mesoscopic Materials. PhD thesis, Universitat Hamburg, 2016.
35. Cereser, A. Nanofocused X-Ray Analysis of Semiconductor Nanowires, 2011.
36. Jacobsen, C.; Kirz, J. X-Ray Microscopy with Synchrotron Radiation. *Nat Struct Biol* **1998**, *5*, 650–653, doi:10.1038/1341.
37. Ackermann, W.; Asova, G.; Ayvazyan, V.; Azima, A.; Baboi, N.; Bähr, J.; Balandin, V.; Beutner, B.; Brandt, A.; Bolzmann, A.; et al. Operation of a Free-Electron Laser from the Extreme Ultraviolet to the Water Window. *Nat Photonics* **2007**, *1*, 336–342, doi:10.1038/nphoton.2007.76.
38. Kördel, M.; Dehlinger, A.; Seim, C.; Vogt, U.; Fogelqvist, E.; A. Sellberg, J.; Stiel, H.; M. Hertz, H. Laboratory Water-Window x-Ray Microscopy. *Optical Society of America* **2020**, *7*, 658–674.
39. Pereiro, E.; Nicolás, J.; Ferrer, S.; Howells, M.R. A Soft X-Ray Beamline for Transmission X-Ray Microscopy at ALBA. *J Synchrotron Radiat* **2009**, *16*, 505–512, doi:10.1107/S0909049509019396.
40. Wagenaars, E. Plasma Breakdown of Low-Pressure Gas Discharges. Phd Thesis 1 (Research TU/e / Graduation TU/e), Technische Universiteit Eindhoven, 2006.
41. Bennett, W.H. Magnetically Self-Focussing Streams. *Physical Review* **1934**, *45*, 890–897, doi:10.1103/PhysRev.45.890.
42. Vrba, P.; Zakharov, S.V.; Jancarek, A.; Vrbova, M.; Nevrkla, M.; Kolar, P. Pinching Capillary Discharge as a Water Window Radiation Source. *J Electron Spectros Relat Phenomena* **2011**, *184*, 335–337, doi:10.1016/j.elspec.2010.12.013.
43. Parkman, T.; Nevrkla, M.; Jančárek, A.; Turňová, J.; Pánek, D.; Vrbová, M. Table-Top Water-Window Microscope Using a Capillary Discharge Plasma Source with Spatial Resolution 75 Nm. *Applied Sciences* **2020**, *10*, 6373, doi:10.3390/app10186373.
44. Ayele, M.G.; Wachulak, P.W.; Czwartos, J.; Adjei, D.; Bartnik, A.; Wegrzynski, Ł.; Szczurek, M.; Pina, L.; Fiedorowicz, H. Development and Characterization of a Laser-Plasma Soft X-Ray Source for Contact Microscopy. *Nucl Instrum Methods Phys Res B* **2017**, *411*, 35–43, doi:10.1016/j.nimb.2017.03.082.
45. Suckewer, S.; Morozov, A.; Goltsov, A.; Sokolov, A. V; Scully, M.O. Development of a Compact X-Ray Laser in the 'Water Window' at 4.0 Nm. *Laser Phys Lett* **2021**, *18*, 115001, doi:10.1088/1612-202X/ac26cb.
46. Sayre, D., Kirz, J, Feder, R., Kim, D.M., Spiller, E. Transmission Microscopy of Unmodified Biological Materials: Comparative Radiation Dosages with Electrons and Ultrasoft X-Ray Photons 1997, 337–349.
47. Ito, A.; Inoue, T.; Kado, M.; Ohigashi, T.; Tone, S.; Shinohara, K. Biomedical Application of Soft X-Ray Microscopy with Special Reference to Spectromicroscopy. *Acta Phys Pol A* **2016**, *129*, 260–263, doi:10.12693/APhysPolA.129.260.

48. Lawrence Berkeley National Laboratory Machine Information Available online: https://als.lbl.gov/machine-information/ (accessed on 7 December 2023).
49. Martz, D.H.; Selin, M.; von Hofsten, O.; Fogelqvist, E.; Holmberg, A.; Vogt, U.; Legall, H.; Blobel, G.; Seim, C.; Stiel, H.; et al. High Average Brightness Water Window Source for Short-Exposure Cryomicroscopy. *Opt Lett* **2012**, *37*, 4425, doi:10.1364/ol.37.004425.
50. Kondo, H.; Tomie, T. Optimization of a Laser-Plasma x-Ray Source for Contact x-Ray Microscopy. *J Appl Phys* **1994**, *75*, 3798–3805, doi:10.1063/1.356055.
51. Kishimoto, M.; Kado, M.; Ishino, M.; Tamotsu, S.; Yasuda, K.; Shinohara, K. Development of Single Shot Soft X-Ray Contact Microscopy System for Nano-Scale Dynamics Measurement of Living Biological Specimen. *AIP Conf Proc* **2012**, *1465*, 43–47, doi:10.1063/1.4737537.
52. Trail, J.A.; Byer, R.L. *Compact Scanning Soft-x-Ray Microscope Using a Laser-Produced Plasma Source and Normal-Incidence Multilayer Mirrors*; 1989; Vol. 14;.
53. Ogata, T.; Iimura, K.; Aoki, S.; Yoshidomi, Y.; Mitomi, O.; Shinada, K. Development of a Grazing Incidence Soft X-Ray Microscope with a Laser-Produced Plasma Source. *J Electron Spectros Relat Phenomena* **1996**, *80*, 357–360, doi:10.1016/0368-2048(96)02991-X.
54. Afanasiev, Yu. V.; Chichkov, B.N.; Demchenko, N.N.; Isakov, V.A.; Zavestovskaya, I.N. Ablation of Metals by Ultrashort Laser Pulses: Theoretical Modeling and Computer Simulations. *Journal of Russian Laser Research* **1999**, *20*, 89–115, doi:10.1007/BF02508686.
55. Afanasiev, Yu. V.; Chichkov, B.N.; Demchenko, N.N.; Isakov, V.A.; Zavestovskaya, I.N. Ablation of Metals by Ultrashort Laser Pulses: Theoretical Modeling and Computer Simulations. *Journal of Russian Laser Research* **1999**, *20*, 89–115, doi:10.1007/BF02508686.
56. Nolte, S.; Momma, C.; Jacobs, H.; Tü, A.; Chichkov, B.N.; Wellegehausen, B.; Welling, H. *Ablation of Metals by Ultrashort Laser Pulses*; 1997;
57. 藤田雅之 レーザー加工の物理(3)光パルス幅と加工. *Japanese journal of optics : publication of the Optical Society of Japan* **2007**, *36*, 459–465.
58. Attwood, D. *Soft X-Rays and Extreme Ultraviolet Radiation*; Cambridge University Press, 1999; ISBN 9780521652148.
59. Wachulak, P.W.; Bartnik, A.; Fiedorowicz, H.; Rudawski, P.; Jarocki, R.; Kostecki, J.; Szczurek, M. “Water Window” Compact, Table-Top Laser Plasma Soft X-Ray Sources Based on a Gas Puff Target. *Nucl Instrum Methods Phys Res B* **2010**, *268*, 1692–1700, doi:10.1016/j.nimb.2010.02.002.
60. Kologrivov, A.A.; Rupasov, A.A.; Bolkhovitinov, E.A.; Stuchebrukhov, I.A.; Abrosimov, S.A.; Shelkovenko, T.A. Spectral Studies of Soft X-Ray Radiation of Laser-Produced Plasma of Various Target Materials in a Wide Spectral Range. *Phys Rev E* **2022**, *106*, 045205, doi:10.1103/PhysRevE.106.045205.
61. Davis, J.S.; Drake, R.P.; Fraenkel, M.; Frank, Y.; Keiter, P.A.; Klein, S.R.; Raicher, E.; Shvarts, D.; Trantham, M.R. Soft X-Ray Emission from Laser-Irradiated Gold Foils. *Phys Plasmas* **2018**, *25*, doi:10.1063/1.5036934.
62. MacGowan, B.J.; Maxon, S.; Hagelstein, P.L.; Keane, C.J.; London, R.A.; Matthews, D.L.; Rosen, M.D.; Scofield, J.H.; Whelan, D.A. Demonstration of Soft X-Ray

Amplification in Nickel-like Ions. *Phys Rev Lett* **1987**, *59*, 2157–2160, doi:10.1103/PhysRevLett.59.2157.
63. Stein, G.J.; Keathley, P.D.; Krogen, P.; Liang, H.; Siqueira, J.P.; Chang, C.-L.; Lai, C.-J.; Hong, K.-H.; Laurent, G.M.; Kärtner, F.X. Water-Window Soft x-Ray High-Harmonic Generation up to the Nitrogen K-Edge Driven by a KHz, 2.1 Mm OPCPA Source. *Journal of Physics B: Atomic, Molecular and Optical Physics* **2016**, *49*, 155601, doi:10.1088/0953-4075/49/15/155601.
64. Wachulak, P.W. Recent Advancements in the "Water-Window" Microscopy with Laser-Plasma SXR Source Based on a Double Stream Gas-Puff Target. *Opto-Electronics Review* **2016**, *24*, doi:10.1515/oere-2016-0018.
65. Johansson, G.A.; Holmberg, A.; Hertz, H.M.; Berglund, M. Design and Performance of a Laser-Plasma-Based Compact Soft x-Ray Microscope. *Review of Scientific Instruments* **2002**, *73*, 1193–1197, doi:10.1063/1.1445870.
66. Dong, Y.; Zhang, L.; Yang, J.; Shang, W. Detailed Energy Distributions in Laser-Produced Plasmas of Solid Gold and Foam Gold Planar Targets. *Phys Plasmas* **2013**, *20*, doi:10.1063/1.4841315.
67. Węgrzyński, Ł.; Bartnik, A.; Wachulak, P.; Fok, T.; Fiedorowicz, H. Laser-Produced Plasma Soft x-Ray Source Based on an Aerosol Target. *Phys Plasmas* **2020**, *27*, doi:10.1063/5.0005933.
68. Tanaka, H.; Akinaga, K.; Takahashi, A.; Okada, T. Development of a Target for Laser-Produced Plasma EUV Light Source Using Sn Nano-Particles. *Applied Physics A* **2004**, *79*, 1493–1495, doi:10.1007/s00339-004-2828-2.
69. Shou, Y.; Kong, D.; Wang, P.; Mei, Z.; Cao, Z.; Pan, Z.; Li, Y.; Xu, S.; Qi, G.; Chen, S.; et al. High-Efficiency Water-Window x-Ray Generation from Nanowire Array Targets Irradiated with Femtosecond Laser Pulses. *Opt. Express* **2021**, *29*, 5427–5436, doi:10.1364/OE.417512.
70. Ohashi, H.; Higashiguchi, T.; Suzuki, Y.; Arai, G.; Otani, Y.; Yatagai, T.; Li, B.; Dunne, P.; O'Sullivan, G.; Jiang, W.; et al. Quasi-Moseley's Law for Strong Narrow Bandwidth Soft x-Ray Sources Containing Higher Charge-State Ions. *Appl Phys Lett* **2014**, *104*, doi:10.1063/1.4883475.
71. Higashiguchi, T.; Otsuka, T.; Yugami, N.; Jiang, W.; Endo, A.; Li, B.; Dunne, P.; O'Sullivan, G. Feasibility Study of Broadband Efficient "Water Window" Source. *Appl Phys Lett* **2012**, *100*, doi:10.1063/1.3673912.
72. Kado, M.; Kishimoto, M.; Shinohara, K.; Ejima, T. Increase of the Emission of Laser-Produced Plasmas under N2 Gas Atmosphere in the 2.9-6 Nm Region. *Appl Phys Lett* **2017**, *111*, doi:10.1063/1.4996890.
73. John, C.; Kishimoto, M.; Johzaki, T.; Higashiguchi, T.; Kakunaka, N.; Matsumoto, Y.; Hasegawa, N.; Nishikino, M.; Ejima, T.; Sunahara, A.; et al. Enhancement of Water-Window Soft x-Ray Emission from Laser-Produced Au Plasma under Low-Pressure Nitrogen Atmosphere. *Opt Lett* **2019**, *44*, 1439, doi:10.1364/ol.44.001439.
74. Cryan, J.P.; Glownia, J.M.; Andreasson, J.; Belkacem, A.; Berrah, N.; Blaga, C.I.; Bostedt, C.; Bozek, J.; Cherepkov, N.A.; DiMauro, L.F.; et al. Molecular Frame Auger Electron Energy Spectrum from N2. *Journal of Physics B: Atomic, Molecular and Optical Physics* **2012**, *45*, 055601, doi:10.1088/0953-4075/45/5/055601.
75. Koç, A.; Hauf, C.; Woerner, M.; von Grafenstein, L.; Ueberschaer, D.; Bock, M.;

Griebner, U.; Elsaesser, T. High-Flux Table-Top Hard X-Ray Source Driven by Femtosecond Mid-Infrared Pulses at a 1 KHz Repetition Rate. In Proceedings of the 2021 Conference on Lasers and Electro-Optics (CLEO); 2021; pp. 1–2.
76. Kishimoto, M.; Kado, M.; Ishino, M.; Tamotsu, S.; Yasuda, K.; Shinohara, K. Development of Single Shot Soft X-Ray Contact Microscopy System for Nano-Scale Dynamics Measurement of Living Biological Specimen.; 2012; pp. 43–47.
77. Le Pape, S.; Divol, L.; Macphee, A.; McNaney, J.; Hohenberger, M.; Froula, D.; Glebov, V.; Landen, O.L.; Stoeckl, C.; Dewald, E.; et al. Optimization of High Energy x Ray Production through Laser Plasma Interaction. *High Energy Density Phys* **2019**, *31*, 13–18, doi:10.1016/j.hedp.2019.01.002.
78. Ishino, M.; Kado, M.; Nishikino, M.; Shinohara, K.; Tamotsu, S.; Yasuda, K.; Hasegawa, N.; Kishimoto, M.; Ohba, T.; Kawachi, T. Observations of the Intense Soft X-Ray Emissions from Ultrathin Au Films Irradiated with High Contrast Laser Pulses.; Heisterkamp, A., Neev, J., Nolte, S., Trebino, R.P., Eds.; February 11 2010; p. 75891B.
79. Hara, H.; Kawasaki, H.; Tamura, T.; Hatano, T.; Ejima, T.; Jiang, W.; Ohashi, H.; Namba, S.; Sunahara, A.; Sasaki, A.; et al. Emission of Water-Window Soft x-Rays under Optically Thin Conditions Using Low-Density Foam Targets. *Opt Lett* **2018**, *43*, 3750, doi:10.1364/ol.43.003750.
80. Fujioka, S.; Nishimura, H.; Nishihara, K.; Sasaki, A.; Sunahara, A.; Okuno, T.; Ueda, N.; Ando, T.; Tao, Y.; Shimada, Y.; et al. Opacity Effect on Extreme Ultraviolet Radiation from Laser-Produced Tin Plasmas. **2005**, *235004*, 1–4, doi:10.1103/PhysRevLett.95.235004.
81. Hou, J.J.; Zhang, L.; Zhao, Y.; Yan, X.; Ma, W.; Dong, L.; Yin, W.; Xiao, L.; Jia, S. Laser-Induced Plasma Characterization through Self-Absorption Quantification. *J Quant Spectrosc Radiat Transf* **2018**, *213*, 143–148, doi:10.1016/j.jqsrt.2018.04.009.
82. Sherbini, A.M. El; El Sherbini, Th.M.; Hegazy, H.; Cristoforetti, G.; Legnaioli, S.; Palleschi, V.; Pardini, L.; Salvetti, A.; Tognoni, E. Evaluation of Self-Absorption Coefficients of Aluminum Emission Lines in Laser-Induced Breakdown Spectroscopy Measurements. **2005**, *60*, 1573–1579, doi:10.1016/j.sab.2005.10.011.
83. Aragón, C.; Bengoechea, J.; Aguilera, J.A. Influence of the Optical Depth on Spectral Line Emission from Laser-Induced Plasmas. *Spectrochim Acta Part B At Spectrosc* **2001**, *56*, 619–628, doi:10.1016/S0584-8547(01)00172-0.
84. Kondo, H.; Tomie, T. Optimization of a Laser-Plasma x-Ray Source for Contact x-Ray Microscopy. *J Appl Phys* **1994**, *75*, 3798–3805, doi:10.1063/1.356055.
85. ROHM Semiconductor *Impedance Characteristics of Bypass Capacitor*; 2020;
86. Kramida, A.; Ralchenko, Yu.; Reader, J.; NIST ASD Team NIST Atomic Spectra Database (Version 5.10) Available online: https://physics.nist.gov/asd (accessed on 27 November 2023).
87. Li, B.; Higashiguchi, T.; Otsuka, T.; Yugami, N.; Dunne, P.; Kilbane, D.; Sokell, E.; O'Sullivan, G. Analysis of Laser Produced Plasmas of Gold in the 1-7 Nm Region. *Journal of Physics B: Atomic, Molecular and Optical Physics* **2014**, *47*, 1–7, doi:10.1088/0953-4075/47/7/075001.
88. Gu, M.F. The Flexible Atomic Code. *Can J Phys* **2008**, *86*, 675–689, doi:10.1139/P07-197.
89. Andor (Oxford instrument) *IKon-M CCD PERFORMANCE Sheet*; 2010;

90. Hamamatsu *Characteristics and Use of Charge Amplifier SOLID STATE DIVISION*;
91. Ranger, N.T. The AAPM/RSNA Physics Tutorial for Residents. *RadioGraphics* **1999**, *19*, 481–502, doi:10.1148/radiographics.19.2.g99mr30481.
92. Pan, Y.; Tomita, K.; Sunahara, A.; Sasaki, A.; Nishihara, K. Joint Measurement of Electron Density, Temperature, and Emission Spectrum of Nd:YAG Laser-Produced Tin Plasma. *Appl Phys Lett* **2023**, *123*, doi:10.1063/5.0174185.
93. Rowland, H.A. LXI. Preliminary Notice of the Results Accomplished in the Manufacture and Theory of Gratings for Optical Purposes . *The London, Edinburgh, and Dublin Philosophical Magazine and Journal of Science* **1882**, *13*, 469–474, doi:10.1080/14786448208627217.
94. Beutler, H.G. *The Theory of the Concave Grating*; 1945; Vol. 35;.
95. Palmer, C. *DIFFRACTION GRATING HANDBOOK Eighth Edition*; 2020;
96. Nakano, N.; Kuroda, H.; Kita, T.; Harada, T. Development of a Flat-Field Grazing-Incidence XUV Spectrometer and Its Application in Picosecond XUV Spectroscopy. *Appl. Opt.* **1984**, *23*, 2386–2392, doi:10.1364/AO.23.002386.
97. He, Z.; Shu, R.; Wang, J. Research on Method of Geometry and Spectral Calibration of Pushbroom Dispersive Hyperspectral Imager. In Proceedings of the Multispectral, Hyperspectral, and Ultraspectral Remote Sensing Technology, Techniques and Applications IV; SPIE, November 9 2012; Vol. 8527, p. 85270R.
98. Köhler, C.H. Airborne Imaging Spectrometer HySpex. *Journal of large-scale research facilities JLSRF* **2016**, *2*, doi:10.17815/jlsrf-2-151.
99. Barucci, M.A.; Reess, J.M.; Bernardi, P.; Doressoundiram, A.; Fornasier, S.; Le Du, M.; Iwata, T.; Nakagawa, H.; Nakamura, T.; André, Y.; et al. MIRS: An Imaging Spectrometer for the MMX Mission. *Earth, Planets and Space* **2021**, *73*, doi:10.1186/s40623-021-01423-2.
100. Shugaev, M. V.; He, M.; Levy, Y.; Mazzi, A.; Miotello, A.; Bulgakova, N.M.; Zhigilei, L. V. Laser-Induced Thermal Processes: Heat Transfer, Generation of Stresses, Melting and Solidification, Vaporization, and Phase Explosion. In *Sugioka, K. (eds) Handbook of Laser Micro- and Nano-Engineering*; Springer, 2020 ISBN 9783030636470.
101. Daido, H.; Sasaki, A. Material Property and Simulation Methods Applicable to Laser Produced Plasmas in the New Density and Temperature Region. *J. Plasma Fusion Res.* **2013**, *89*, 403–407.
102. Rethfeld, B.; Ivanov, D.S.; Garcia, M.E.; Anisimov, S.I. Modelling Ultrafast Laser Ablation. *J Phys D Appl Phys* **2017**, *50*, doi:10.1088/1361-6463/50/19/193001.
103. John, C. Spectroscopic Study on Enhancement of Water-Window X-Ray Radiation Emitted from Laser-Produced Gold Plasmas, Hiroshima University, 2020.
104. Sunahara, A. Initial Process of Laser-Plasma Interaction in the Extreme Ultra-Violet Light Source and the Inertial Confinement Fusion Plasmas. *J. Plasma Fusion Res.* **2013**, *89*, 416–422.
105. Eliezer, S. The Interaction of High-Power Lasers With Plasmas. *Plasma Phys Control Fusion* **2003**, *45*, 181–181, doi:10.1088/0741-3335/45/2/701.
106. Anisimov, S.I.; Kapeliovich, B.L.; Perelman, T.L. Electron Emission from Metal Surfaces Exposed to Ultrashort Laser Pulses. *Journal of Experimental and Theoretical Physics* **1974**, *39*, 375–377.
107. 山本　学; 村山　精一 プラズマの分光計測; 学会出版センター;

108. Lyon, S.P.; Johnson, J.D. SESAME: The Los Alamos National Laboratory Equation of State Database Contents 1992.
109. Saltzmann, D. Atomic Physics in Hot Plasmas 1998.
110. 砂原 淳 輻射流体シミュレーションによる極端紫外光源プラズ マの挙動解析. 応用物理 **2014**, *83*.
111. SUNAHARA, A.; NISHIHARA, K.; SASAKI, A. Optimization of Extreme Ultraviolet Emission from Laser-Produced Tin Plasmas Based on Radiation Hydrodynamics Simulations. *Plasma and Fusion Research* **2008**, *3*, 043–043, doi:10.1585/pfr.3.043.
112. Kodama, R.; Mochizuki, T.; Tanaka, K.A.; Yamanaka, C. Enhancement of KeV X-Ray Emission in Laser- Produced Plasmas by a Weak Prepulse Laser. *Appl Phys Lett* **1987**, *50*, 720–722.
113. Gray, R.J.; Wilson, R.; King, M.; Williamson, S.D.R.; Dance, R.J.; Armstrong, C.; Brabetz, C.; Wagner, F.; Zielbauer, B.; Bagnoud, V.; et al. Enhanced Laser-Energy Coupling to Dense Plasmas Driven by Recirculating Electron Currents. *New J Phys* **2018**, *20*, doi:10.1088/1367-2630/aab089.